University of Strathclyde
Department of Chemical and Process Engineering

CHARACTERISATION OF MICROPOROUS CARBONS BY POSITRON ANNIHILATION LIFETIME SPECTROSCOPY

by

Jhon Jairo Fernandez Hincapie

THE UNIVERSITY OF STRATHCLYDE IN GLASGOW

A thesis presented in fulfilment of the requirements for the degree of

Doctor of Philosophy
2005

ACKNOWLEDGEMENTS

The author wishes to express his sincere gratitude to Professor Peter J. Hall for his guidance and "patience".

The author would like to thank the Colombian Institute for the Science and Technology Development, COLCIENCIAS, and the Universidad de Antioquia (Medellin-Colombia) for financial support.

The author would also likes to thank the Energy Resources and Environmental Chemistry Group (Universidad de Antioquia, Colombia), and the Chemistry Department (Universidad de Alicante, Spain) for my research stays in theirs laboratories.

Special thanks go out to Dr. Fanor Mondragón for his advice and encouragement.

Warm thanks go out to Mrs Elizabeth Hall for her friendship and support.

To my son:

Juan Camilo

ABSTRACT

Gasification of coal and other organic materials using oxidative gases such as oxygen, carbon dioxide or steam produces porous carbon materials. The uncertainty in porosity information can be inadequate for a number of potentially applications of microporous carbons.

Positron annihilation lifetime spectroscopy (PALS) senses the electronic properties of condensed matter. A PALS experiment implies the measurement of the lifetime, which is the inverse of the annihilation rate. In the present work PALS has been applied to characterise the porosity of gasified carbon materials.

In the case of active carbon fibers (ACFs) the characterization by gas adsorption showed that these materials are essentially microporous with narrow pore size distribution. The PALS analysis showed two lifetime components. There is a predominant lifetime component (> 84%) which ranges from 376 to 393 ps and increases its value with the burn-off. The annihilation mechanism apparently depends on the activation agent. Saran based active carbons (ACs) were prepared by pyrolysis and activation using carbon dioxide, air and steam. Gas adsorption and small angle scattering (SAS) showed that these carbons are essentially microporous materials with wide pore size distribution. PALS showed only one lifetime component. This lifetime component (> 99%) ranges from 382 to 401 ps. The lifetime value increases with the burn-off for the CO_2 gasification process. Coal chars from Argonne Premium Coals were gasified using air, carbon dioxide and steam. The gas adsorption and SAS characterization of these activated chars indicated that they are a mixture of micro and mesoporous with a broad pore size distribution. For these samples PALS showed only one lifetime component this ranges from 352 to 367 ps.

A good correlation between gas adsorption, SAS and PALS analyses permits to associate the main lifetime with the mean micropore size to ACF and AC materials.

CONTENTS

LIST OF TABLES

LIST OF FIGURES

1. CHARACTERISTICS AND ORIGIN OF POROUS CARBONS

1.1 INTRODUCTION

Carbon compounds are extensive and complex structures as a result of the formation of σ- and π- bonds between carbon atoms and with others elements, like hydrogen, nitrogen, oxygen, sulphur, etc. Carbon materials are mainly formed of graphitic sub-units linked together with varying order. They range from well ordered structure like diamond and graphite to less-ordered structure of carbons derived from organic precursors by pyrolysis, also named carbonisation [(1)]. The aim of the carbonisation is to increase the carbon content.

There exists a wide variety of commercial carbons including cokes, active carbons, carbon blacks, graphites, carbon fibres and composites. In this section some important carbon forms will be defined which will be used through this work.

Graphitic carbons are allotropic forms of the element carbon highly crystalline without any consideration of structural order or defects [(2)].

Pitches are carbonaceous materials derived from organic precursors, like coal or petroleum, by low temperature distillation [(3)].

Cokes are carbons produced by carbonisation of organic materials which have passed through a liquid or liquid-crystalline state during this process [(2)].

Coal chars are carbon materials from the pyrolysis of some coals which have not passed through a liquid stage [(4)].

Coal is essentially a carbonaceous material and all coals are rocks formed from the altered remains of what was originally debris vegetation. The composition of coals encountered is related to the original vegetal material and the burial history in terms of temperature and pressure [5]. Elemental analysis of coal shows a carbon content between 55 to 92 % which is associated with the coalification process. Also, hydrogen, oxygen, nitrogen and sulphur are presented in small quantities in the organic phase, mineral matter is distributed through the organic phase and it is composed mainly by aluminosilicates, carbonates and sulphides [6,7]. The world total resources of coals are currently estimated at about 11.78×10^{12} tonnes [8]. Despite that the main use of coal is as fossil fuel, the production of strong and porous cokes and active carbons by carbonisation from coal have an important industrial use [9,10].

Chars are some carbonaceous materials obtained from wood or other vegetable materials by carbonisation which have not passed through a fluid stage [4].

Active carbons are highly porous carbons, usually chars from wood, coal, lignite, coconut shell and peat, which have been subjected either to reaction with gases during or after carbonisation or to chemical treatment to increase porosity [4].

Carbon fibres are PolyAcryloNitrile- and pitch- based filaments carbons in a non-graphitic stage [11].

Carbon blacks are colloidal carbons in form of sphere or their fused aggregates usually produced by chemical vapour deposition of carbon from volatile hydrocarbons on carbon or ceramic substrates [3].

Activated carbons have a large internal surface of 400-1600 m^2g^{-1} and a large pore volume of more than 0.3 cm^3g^{-1}; these properties are created

predominantly by the micropore system. These characteristics are important for adsorption and desorption processes. Active carbons generally have hydrophobic surface properties which permits to these materials adsorb preferably organic substances and other non-polar compounds from the gaseous and liquid phase.

Microporous carbons used as adsorbents have a high demand. For example it is calculated that the production of activated carbon is the order of 350000 tons per year [12]. The raw materials used to produce microporous carbon adsorbents are of low value, have a high carbon content, and are low in inorganics. The raw carbonaceous materials that are used by the industry are wood, coal, lignite, coconut shell, and peat. It is reported that 130000 tons/year of activated carbon are producing from wood and 100000 tons/year from coal [13]. The current tendency is toward an increase in coal use, because of worldwide politics to control deforestation. Another alternative is to use wastes of vegetable origin, like fruit stones, nutshells, and sawdust. As a result of the microporous structure, activated carbons have a wide use in adsorption, which range from domestic to industrial applications.

In vapour phase, common applications are: Solvent recovery of organic solvents to optimise process economics and control vapour emissions. Production of industrial respirators to adsorb organic vapours. Heating, ventilation and air conditioning purification. Removal of heavy metals, dioxins and other contaminants in domestic, chemical and clinical waste disposal. Purification of carbon dioxide from fermentation processes. Minor uses are the manufacture of fridge deoderisers and filter tips in cigarettes [13].

In liquid phase, common applications are: Removal of dissolved organic contaminants, control of taste and odour problems in potable water treatment for domestic use or production of soft drinks and beer. Gold recovery from tailings dissolved in sodium cyanide. Reduction of total

organic halogens (TOX), bioloical oxygen demand (BOD) and chemical oxygen demand (COD) from industrial waste water. Purification and decolorisation of sugar. Removal of residual ozone and control of chloramine levels in swimming pools [13].

Microporous carbons are also used as catalysts and catalysts supports for certain reactions of oxidation, decomposition, halogenation and dehalogenation. For these reactions carbons are impregnated, for example with iodine [14], silver, aluminium, manganese, zinc, iron, lithium, and calcium [15].

There exists other carbon compounds of great scientific interest like fullerenes and nanotubes concerning to the architecture of sp^2 bonded carbon and the creation of closed shell structures out of planar graphite sheets. They might find applications in the electronic industry due to their unique electrical and mechanical properties [16]. In addition nanotubes have an other special feature which is the smooth, straight, and one-dimensional channel in their centres. The size distribution of the tube cavity of typical nanotubes is quite narrow with a mean diameter value close to 1.4 nm which ranges between 1.2 to 6 nm [17]. This brings the possibility of using nanotubes as nanosize container systems. In particular some attempts are made to store hydrogen and natural gas into nanotubes [17-19]. Today, the industrial use of fullerenes and nanotubes is restricted because their production is still very expensive.

As was explained above, the microporosity predominant in carbons which controlled the majority of their applications needs to be characterised on the basis of techniques that certainly yield for pore properties, such as pore size and pore size distribution. This work studies the capabilities of a powerful technique like Positron Annihilation Lifetime Spectroscopy to deal with this matter.

1.2 CHARACTERISTICS AND ORIGIN OF POROUS CARBONS

1.2.1 Carbonisation

Chars or carbons are produced from a large number of organic precursors, e.g. coal, wood, cellulose, nut-shells, pitches derived from organic precursors (normally, coal-tar and petroleum pitch and polymers (e.g. poly(acrylonitrile) or PAN, poly(vinyldenechloride-acrylate) copolymers so-called Saran)) by relative low temperature processes[13]. These raw materials may additionally contain heteroatoms and inorganic constituents. High temperature pyrolysis of these precursors ends in the removal of the volatile matter, resulting in a solid residue, whose carbon content is higher than that of the parental material and whose structure depends on the organic precursor and the heat treatment. The final material is porous as a result of the volatile matter released process together with the complex packing within and between the carbonised particles.

1.2.1.1 Influence of precursor material and thermal treatment on char properties

It is accepted that the final structure of a char/carbon material depends on the structure of the organic precursor and any thermal treatment [20-22]. Carbons produced from carbonisation are in general a mixture of well-ordered material (like graphite where there is a high degree of anisotropy), and less-ordered material. It has been reported that the progressive increase in temperature during the carbonisation results in a highly graphitic structure [20]. The shape, size and distribution of porosity are associated with the structure of carbons and graphites. The Figure 1.1 illustrates the evolution of the carbonaceous structures during typical heating.

When the precursor material does no pass through a fluid phase during carbonisation the resultant structure retains much of the original and

complex macromolecular structure and is called non-graphitizable or isotropic carbon. These materials have a random stacking cross-linking structure that has space between the lamellae or groups of lamellae results a well developed micropore system and generally have high surface areas. Typical examples of precursors to produce isotropic carbons are: natural materials (wood, nut and nut-shells), synthetic resins (phenolic resin, polyfurfuryl alcohol, polyvinylidene chloride), most forms of biomass and, some non-fusing coals (low rank coals, brown coals and non-caking coals).

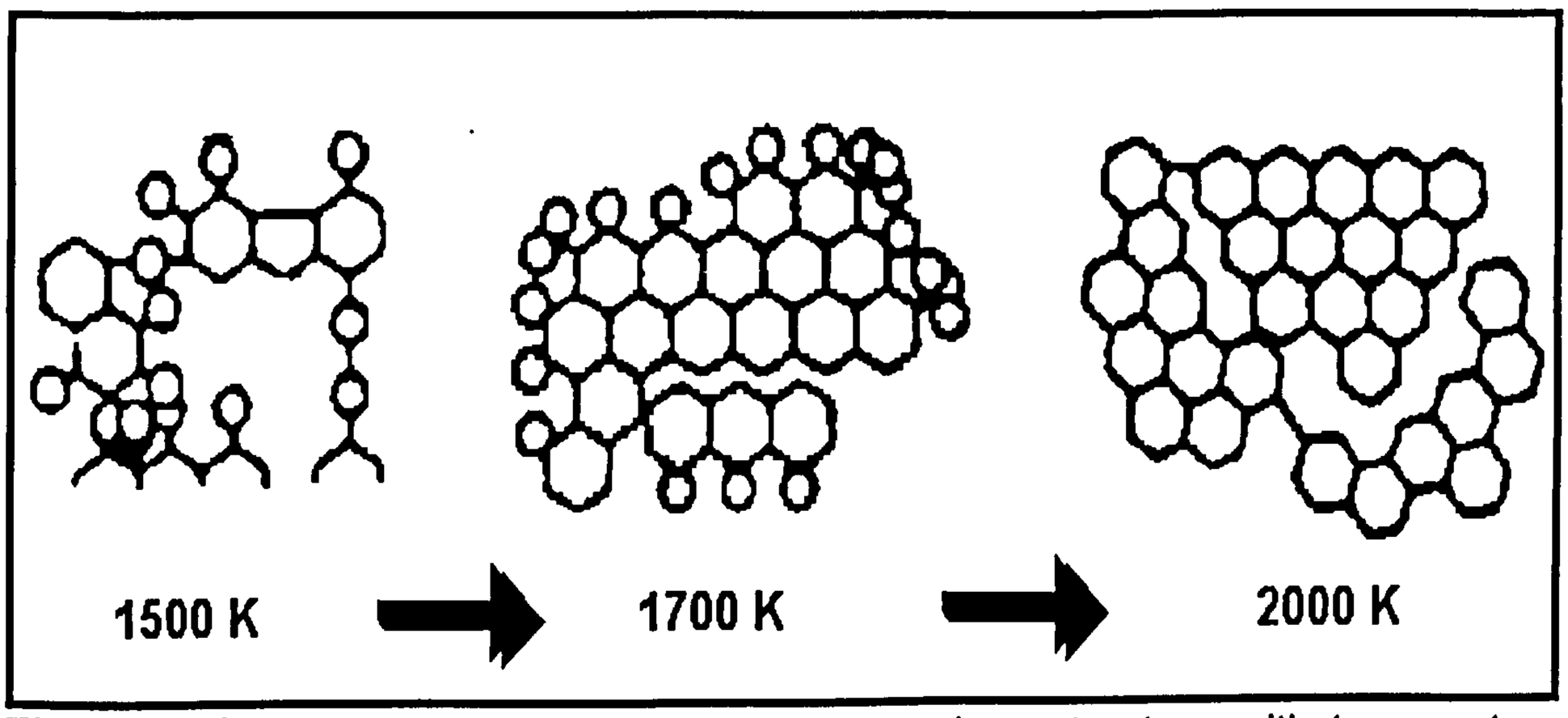

Figure 1.1: Diagram showing changes in carbon structure with temperature during a carbonisation process (adapted from reference 1)

On the other hand, when the precursor material passes through a fluid phase during carbonisation a graphitizable or anisotropic carbon is produced with a high degree of parallel stacking of lamellae. Therefore the main characteristic of these materials are low surface area and low microporosity. Precursors for this type of materials are petroleum or coal pitch, some polymers (PVC), and fusing coals [23,24].

When carbons were prepared from coals the rank of coal influences the pyrolysis process and char porosity [25-27]. The analysis of pore size distribution showed that chars from higher rank coals do not develop microporosity whereas chars from low rank coals exhibit significant levels of microporosity. Carbons from cellulose precursors have an essentially

bimodal, macropore and micropore, size distribution after the heat treatment in the range 1173-1873 K [28].

There are several works that report increases of the internal surface area, measured by gas adsorption, with heat treatment temperature between 773 to 1273 K [29-34]. Coals chars, ranging from lignites to anthracites, show a maximum in surface area between 873 and 1223 K [29-30], while graphite only develops an increase of internal surface area above 1373 K (< 4 m^2g^{-1}) [31]. These results were explained by a mechanism of the particle in its plastic state, specially when high heating rates were used [32-33]. Although, analytical evidence was found only for development of macropores, some authors assumed similar mechanism to explain the production of meso- and micropores [34].

1.2.1.2 Development of porosity by physical activation in carbons

As was discussed above, the carbons from materials such as wood, nutshells and some coals are porous solids. However, if these solids are modified by physical activation, i.e. gasification with an oxidising gas (CO_2, oxygen and steam) at temperatures from 973 to 1373 K, they enhance the microporous system, and therefore, the surface area. The extent of the porosity development and its characteristics depends on temperature, concentration of the reactant gas and original carbon structure. In general, rates of gasification can be influenced by the development of porosity. The adsorptive properties of active carbons are mainly dependent on the characteristics of the micropore system because they typically contain 90-95% of the total surface area of a typical active carbon. The presence of mesopores in this kind of materials plays a role in transport for the adsorptive to the micropores [35].

The investigation of the development of porosity during carbon gasification had been the objective of a number of research studies, with varying

results. The role of the micropore surface area could be an important factor in low temperature gasification reactivities as a result of microporous diffusion. This was shown in a comparative study of a high-surface area, but non-macroporous sucrose char that exhibited a low gasification rate in CO_2 between 673 and 873 K due to slow microporous diffusion while a highly macroporous Spherocarb carbon had complete reactant accessibility in the same reaction [36,37].

A consensus indicates that the evolution of microporosity is inhibited with increasing gasification temperature in favour of the enhancement of mesopores and macropores [38-40]. This behaviour had been found in chars derived from brown coals gasified in CO_2 at temperatures ranging from 1123 to 1373 K, the porous structure was analysed by CO_2 adsorption [38]. A similar result was reported for an hvb coal char and a pich coke gasified in steam at 1273 K. It was seen for both char and coke that with decreasing reaction rate the CO_2-BET surface area was increased [38]. When the same coal char sample was gasified in air at 673 and 773 K, the maximum value of internal surface area was higher for the reaction at 673 K than the reaction at 773 K [39]. A study of a non-porous graphite during early stages of gasification showed significant amounts of either mesopore and micropore development at low levels of gasification (< 3.4 wt%) [40].

To establish the effect of the gasifying gas on pore development, the same coal char and pitch coke were gasified to 40 wt% of burn-off, in carbon dioxide, steam and hydrogen [34]. Steam produced the highest surface area (measured by CO_2 at 298 K) then the carbon dioxide and hydrogen respectively. Comparison of a brown coal gasified in oxygen at 623 K with steam at 1113 K resulted in a greater development of microporosity for oxygen than steam [41]. The same result was found after comparing gasification in carbon dioxide (at 1098 K) and air (at 673 K) of active carbons produced from olive and almond stones [42,43]. In this case an

initial increase of microporosity was followed by a drastic decrease at high degrees of burn-off.

It is general found that steam produces more highly mesoporous carbons than corresponding carbons prepared by carbon dioxide gasification [35]. Ungasified chars from low range coals have a narrow and fine microporosity and some show closed porosity, then char are converted into a broad and wide pore system, as gasification proceeds [44]. In the same way a coalchar (oxicoke) showed that steam produces a less microporous structure than carbon dioxide gasification. However the reverse effect was found for a coke and a pitch coke gasified in the same conditions. It was explained by a sintering effect during heat treatment causing by their anisotropic structure [45].

A linear correlation between surface area (measured with CO_2) and relative reactivity was found for the gasification of a coal char in steam-hydrogen mixtures [46]. From this, Bhatia and Perlmutter developed an empirical model to predict the reaction on the basis of surface development. This model assumed that the porosity depends on the burn-off. A good fit of this model with reactivity calculated in the reaction with steam at 1073 K was obtained [47]. In spite of this that model did not take account that the development of porosity and the result surface area dependent on the reaction conditions. Other models that have tried to correlate porosity and reactivity, involve the concept of active sites using the active surface area (ASA) parameter which accounts for the amount of oxygen chemisorbed at 573 K during 24 hours [48-51]. This concept was applied to the gasification of a carbon black with oxygen until 35 % of burn-off [48]. The correlation with the reactivity was better than one using N_2-BET surface areas. The main limitations of this model are that some carbons, specially from coal, do not reach the oxygen uptake equilibrium during the chemisorption measurement, and that gasification is influenced

by chemisorption temperature, oxygen concentration and catalytic components [52].

A good correlation have been claimed between reactivity and active surface area (ASA) for coal chars under steam [53] and carbon dioxide [54] gasification. It found in the latter that below 50% burn-off the ASA values were directly proportional to the total micropore area (measured by CO_2 adsorption) and that after this burn-off the three coal chars studied showed the same ASA value.

In summary, carbon reactivity is strongly influenced by gasifying agents, temperature, pressure, catalysis of inorganic species and carbon structure. The global chemical kinetics of heterogeneous carbon reactions are determined by the total surface area, the number of reactive sites per unit of surface area, and the concentration of the gasifying agent [55-58].

The influence of the carbon structure in gasification is important because this is a selective process which occurs at particular sites while other sites remain unaffected. The physical structure defines the active sites for reaction, e.g. dislocations or defects, mainly, in the basal plane and crystalline edges [59-61] (Figure 1.2). Several studies shown that most reaction occurs at the edge rather than basal sites [56,62,63]. Modelling of gasification reaction, which applied the theory of perturbation of molecular orbitals proposed by Huckel in zig-zag and arm-chair polyaromatic molecules, concluded that the zig-zag structure is more reactive than the arm-chair structure (Figure 1.2). When heteroatoms are presented in carbon structures, they are assumed as pyran or chromene forms [64] which permit an attack in edge carbons by the gasifying molecule [48-65].

Carbon pore structure defines the total accessible surface area, and controls diffusion rates and thus the local concentration of gaseous reactants. The interaction of carbons with gases is a heterogeneous

reaction governed mainly by a complex coupling of transport phenomena and chemical kinetics. The overall process can be described by the following events:

-Mass transfer of gasifying agent (and product gases) to the boundary layer surrounding the solid particle.

-Diffusion of gas through the porous structure of the particle.

-Adsorption of reactant gas on the surface.

-Reaction of gases with solid surfaces within the particle (e.g. chemisorptions, chemical rearrangements and formation of adsorbed products on the surface). This step itself involves side reactions of desorption of previous formed surface complex.

When one of these process governs the overall process kinetics, slowest, it is named the rate determining step (RDS) [23].

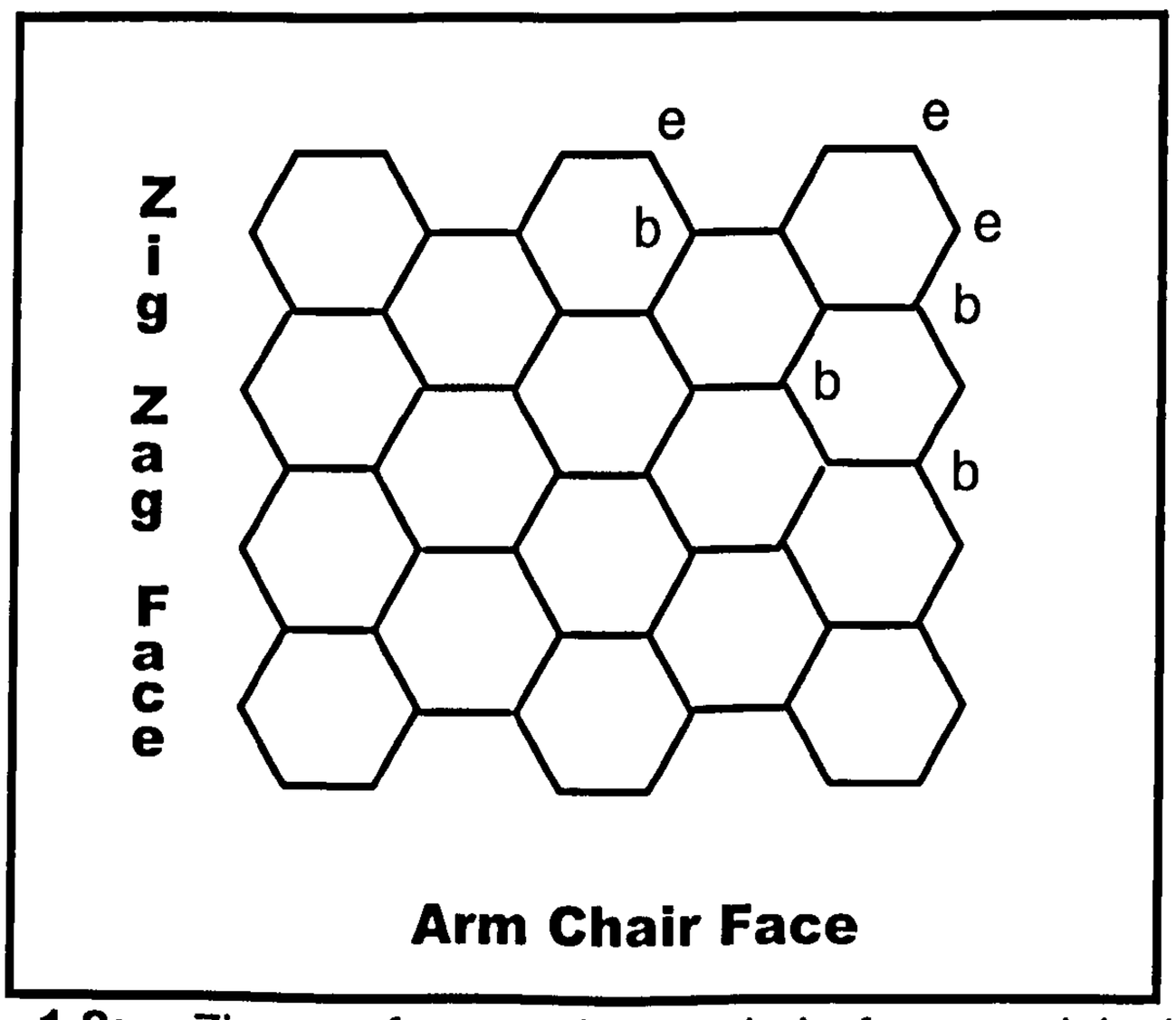

Figure 1.2: Zig-zag face and arm-chair face models in a carbon structure showing basal (B) and edge (E) carbon atoms (adapted from reference 62)

Transport of gasifying agent to the carbon surface (diffusion control) is the RDS for the gasification of a non-porous carbon at high temperatures (>

1000 K). At lower temperatures, the RDS becomes governed by chemical control [23].

A more complex situation is the case of a porous carbon; as a result of restrictions on the diffusion of gases into of pores. The RDS could be controlled by chemical process over the accessible external surface or by diffusion in the accessible internal surface porosity, especially in micropores. An intermediate state may exist in a restricted temperature range. In this region, the rate is partially controlled by diffusion in the pores. It is necessary to have low temperatures and small particle sizes to achieve chemical control of gasification to determine information about the activation energy of the reaction. Gasification at high temperature is controlled only by diffusion of the gas to the external carbon surface, and the concentration of the gas is reduced from its bulk value.

Some inorganic species can promote direct catalytic activity of the surface and create further dislocations during carbon gasification [35,66]. The amount of catalyst is usually not as important as its distribution. Metals, metal oxides and salts are catalytic species for the gasification reactions, the most effective are iron, calcium and magnesium forms [67-69].

Oxygen, carbon dioxide, steam, oxides of nitrogen and hydrogen are the most important gasification agents [56,57,70]. The basic reactions are described by the following chemical equations:

$$C^* + O_2 \rightarrow CO_2$$

$$C^* + 1/2\ O_2 \rightarrow CO$$

$$C^* + H_2O \rightarrow CO + H_2$$

$$C^* + CO_2 \rightarrow 2\ CO$$

$$C^* + 2H_2 \rightarrow CH_4$$

$$C^* + NO \rightarrow CO + 1/2\ N_2$$

$$C^* + 2NO_2 \rightarrow CO_2 + N_2$$
$$C^* + N_2O \rightarrow CO + N_2 \quad (71\text{-}74)$$

Where, C* are the carbons atoms at the surface undergoing reaction. However only oxygen, carbon dioxide and steam gasification carbons will be briefly considered here.

1.2.1.2.1 The oxygen-carbon reaction

This reaction is very sensitive to energy and mass transfer process. The reaction is exothermic and the activation energy ranges from 230 to 270 $kJmol^{-1}$ [75]. The primary products of this reaction are carbon monoxide and carbon dioxide. The CO/CO_2 ratio increases at high temperatures and low pressures. Any catalytic activity favours CO_2 production at lower temperature [60]. This reaction is described by the following chemical equation:

$$C + O_2 \longrightarrow CO_2 \quad \Delta H = -393.5\ kJmol^{-1} \quad (35)$$

A chemisorption mechanism had been proposed based on two main steps: The first step includes; chemisorption and desorption of the products. First, the adsorption of the O_2 take place, then it reacts to form an activated complex and finally a surface intermediate is formed. The second step is desorption of gaseous products; i.e. CO, CO_2, mainly by breakdown of the surface oxide complex [75-80].

Controlled gasification with oxygen proceeds at low pressures and temperatures between 600-800K [48,81]. At high oxygen pressures and moderate temperatures the carbon can ignite and combustion starts.

1.2.1.2.2 The carbon dioxide-carbon reaction

This reaction is also called "Boudouard reaction". It is an endothermic reaction described by following chemical equation:

$$C + CO_2 \longleftrightarrow 2CO \qquad \Delta H = +159.0\ kJmol^{-1}\ ^{(35)}$$

This reaction proceeds very slowly at temperatures below 1000 K and its activation energy ranges from 335 to 375 $kJmol^{-1}$ [75]. At the moment there is no agreement on an exact mechanism for this reaction but there is coincide to attribute the rate retardation to inhibition by CO [61,82-84].

It has been concluded that cyclic esters are primary responsible for the surface acidity found after carbon dioxide gasification of carbons [85,86]. A lactone type surface complex had been attributed as a possible intermediate structure responsible of the formation of these acid esters [61]. It is known that the presence or addition of metals, alkali or alkaline-earth metals has a markedly catalytic effect on the C-CO_2 [87-89].

1.2.1.2.3 The steam carbon reaction

This important reaction is used in industrial processes to produce hydrogen and carbon monoxide (coal gasification, regeneration of coked catalysis, water-gas manufacture). This is an endothermic reaction between carbon and steam accompanied by the "water-gas shift reaction" [61,90] and its activation energy ranges from 270 to 310 $kJmol^{-1}$ [75].

$$C + H_2O \longleftrightarrow CO + H_2 \qquad \Delta H = +118.5\ kJmol^{-1}\ ^{(35)}$$

The secondary water-gas shift reaction is:

$$CO + H_2O \longleftrightarrow CO_2 + H_2 \qquad \Delta H = -42.3\ kJmol^{-1}\ ^{(35)}$$

The first reaction produces CO and H_2. However, these gas products can react further. Thus, the carbon monoxide molecule formed by the above reaction can remove an oxygen atom from occupied sites to form carbon dioxide which can be reduced by an active site to carbon monoxide.

In a similar way to C-CO_2 gasification, C-H_2O reaction is promoted by metals, alkali and alkaline-earth metals, especially calcium forms [90-94]. A study on low-rank coal chars gasification in steam concluded that the reactivity is controlled by the amount of surface active sites exchangeable with Ca and Na [94].

1.3 SUMMARY

This chapter has described the results of several research works concerning the generation of porosity in carbonaceous materials, in particular in activated carbons. In summary, the development of porosity in carbons is a complex process which depends of several factors. Not only the precursor structure is important, but also temperature and heating rate influence the production of porosity in pyrolysis and carbonisation. The physical activation of the char; usually with oxygen, carbon dioxide and steam, is the important step to optimise the amount of microporosity and also to determine the pore size and its distribution. Although, pore development of activated carbon depends on temperature and concentration of reactant gas the effect at catalytic inorganic species must not be ignored.

Normally, the generation of porosity is not uniform lending a non-homogeneous pore system. Usually microporosity is created together with meso- and macroporosity. The characterisation the porosity of the carbon produced as well as during the activation must be performed carefully in order to control and determine the adsorption properties of the material.

There remain several problems in the characterisation of microporosity. Traditionally, gas adsorption techniques are used but the interpretation of results is limited by the experimental conditions used as well as of the adsorptive gas size and its interaction with the porous solid. Also, adsorptive probes can not access closed porosity or ultra-microporosity.

The uses of other techniques to avoid these limitations have been increasing with variable success. For example in small-angle scattering of X-ray (SAXS) or neutrons (SANS) the intensity of the scattered beam and the way in which the intensity varies with the scattering angle are determined by the structure of the porous sample. Pore sizes and surface roughness can be deduced from the scattering data. The use of small-angle scattering is restricted to use a two-phase model, where one phase is the solid and the other is the pore system. The presence of mineral species in the carbon can be increase the scattering intensity data.

This research explores the possibilities of positron annihilation lifetime spectroscopy to probe microporosity in different kinds of carbons. This technique is not destructive and probes the electronic density distribution of the material. When positrons are injected into matter, they thermalise in the order of tens of pico-seconds, and then annihilate by interactions with electrons. The lifetime depends on the electronic density of the material. The next chapter describes the theoretical basis of positron annihilation and application of the common techniques, such as gas adsorption and small-angle scattering, and positron annihilation spectroscopy to study porous carbons.

2. CHARACTERISATION OF POROSITY IN CARBONS

2.1 SCOPE AND DEFINITIONS

In general terms, the characterisation of porosity in porous systems plays two important roles, depending on the purpose for which such information is required. One of them is to have information of physical characteristics such as density, total porosity (and its distribution in into open and close porosity), surface area (and its classification into accessible and inaccessible), pore size, pore size distribution, pore shape and pore connectivity. The second one is to consider the role of the pore structure on effective use of the porous material. Here, it is related with the adsorptive properties, molecular sieving behaviour, the reversibility of the adsorption and desorption, permeability and fluid flow, wetting and dewetting, mechanical strength and resistance to freezing, being the most important.

However, it is not possible to separate the practical consequences of the use of a porous system from its determined physical characteristics. In fact, real systems exhibit a relationship between them, although this could be complex to establish.

The difficult quantitative interaction of the experimental data in terms of its structure to produce a structural model require the study using more than one experimental technique and it is necessary to settled a clear procedure of characterisation, including a specific selection the best techniques to use according to the porous system under study.

At the present, it is possible to use a wide number of techniques to characterise porous solids. The common methods available are shortly described hereafter [95-98].

-***Stereology:*** This technique obtains information by direct observations of a solid to produce realistic pore structure parameters. It is limited to get information of external or macroporous regions by image-analysis such as *optical or electron microscopy*. The resolution of the imaging determines the range of pore sizes accessible by this method.

-***Pycnometry:*** The measure of fluid displacement is used to estimate the apparent density of solid. The volume measured by fluid displacement depends if the liquid probe used as fluid wets or no the solid. The pore volume obtained may be expected to increase as the size of the probe molecule decreases.

-***Adsorption from the gas phase:*** This technique is widely used to characterise a variety of porous solids. In particular, gravimetric or volumetric measure of physisorption (physical adsorption) is used to determine the surface area and pore size distribution of mesoporous materials by adsorption of nitrogen at 77 K [(99)]. It is recommended to employ a range of gas probe molecules to obtain an assessment of the pore system.

-***Methods depending on interfacial curvature:*** In a liquid/gas or liquid/liquid interface formed within a pore wall of the solid the curvature of a meniscus is related both to the size of pore and to either a hydrostatic pressure or vapour pressure. Under this base several methods have been proposed; *the capillary condensation method* described by the so-called BJH (from the measurement of nitrogen vapour pressure over the pores); *the intrusion methods*, which use a non-wetting liquid probe like mercury porosimetry; and *the suction method* and *the maximum bubble pressure method*, which use a wetting liquid probe. These methods are model-dependent and are limited by the mechanical strength of the porous materials.

-Fluid flow method: This a simple and quick method based on the measure of permeability of a porous plug or membrane to a fluid (gas or liquid) flow. The main limitations of the method are that the interpretation of the data involves a number of simplifying assumptions, and that in the case of powders the final packing causing interparticle voids which affects the connectivity.

-Calorimetric methods: The calorimetric methods describe by different assessment the surface area, microporosity and mesoporosity of a porous material. The main calorimetric techniques are; *immersion calorimetry, gas adsorption calorimetry, liquid adsorption calorimetry*, and *thermoporometry*. The immersion calorimetry is based on the measure of the enthalpy change occurring on immersing a dry or pre-covered sample into a liquid; it provides information of the overall surface area and the existence of micropores. The gas adsorption calorimetry is based in the comparison of the energy enhance of adsorption in argon and nitrogen; it is used to detect the existence of micropores smaller than 1 nm. The liquid adsorption calorimetry provides an empirical assessment of the surface area with limited accuracy using a liquid flow microcalorimeter; it is used when the sample is not being available to be dried. Thermoporometry is based in the measure of the depression of the melting point of a condensed adsorbate due to the presence of pores using a differential scanning calorimeter (DSC); it gives information on mesoporosity in the range of 1.5 to 150 nm.

-Radiation scattering: In this non-destructive method the scattered intensity from an incident beam of either electromagnetic radiation (light, *SALS* or X-rays, *SAXS*) or neutrons (*SANS*) on the sample is measured as a function of the scattering angle (2θ) to the incident direction. The scattering intensity variations occur according to the presence of pores in a solid material. Information about surface area and porosity can be extracted using this method in the range from 1 to 1000 nm. The SAXS measurement can be affected by the presence of heavy atoms like metals.

-Others methods: There are other less common methods using to characterise porosity with variety successful. *Size exclusion chromatography* (SEC) is used to calculate pore size distribution of porous materials. *Solid nuclear magnetic resonance* studies the chemical shift of a probe molecule that accesses an internal void. *Ultrasonic method* is used to get information about porosity from variation of the ultrasonic velocity and attenuation of the propagation of ultrasound in porous system. *X-ray* and *neutron diffraction* were used to study the porous cavities on the framework of porous materials with a well defined crystallinity structure such as graphite.

-Pore: It can be defined as an empty space in solid material as a result of discontinuity in the array of the atoms and molecules. In highly porous materials they may form a connected passage to the external surface of solid. This is called open porosity. Closed pores occur when the pore is not connected to the external surface. The total volume of pore is the open pore volume plus closed pore volume [100]. Pores shape can vary from slit-shaped cracks to spherical bubbles [97,100]. Different kinds of pores are illustrated in Figure 2.1.

-Pore size: This is the distance between two opposite walls of the pore.

The International Union of Pure and Applied Chemistry, IUPAC, [99] in order to set a standard procedure, has proposed a classification for porosity based upon size, as follows:

micropores < 2 nm

2 nm < mesopores < 50 nm

50 nm < macropores.

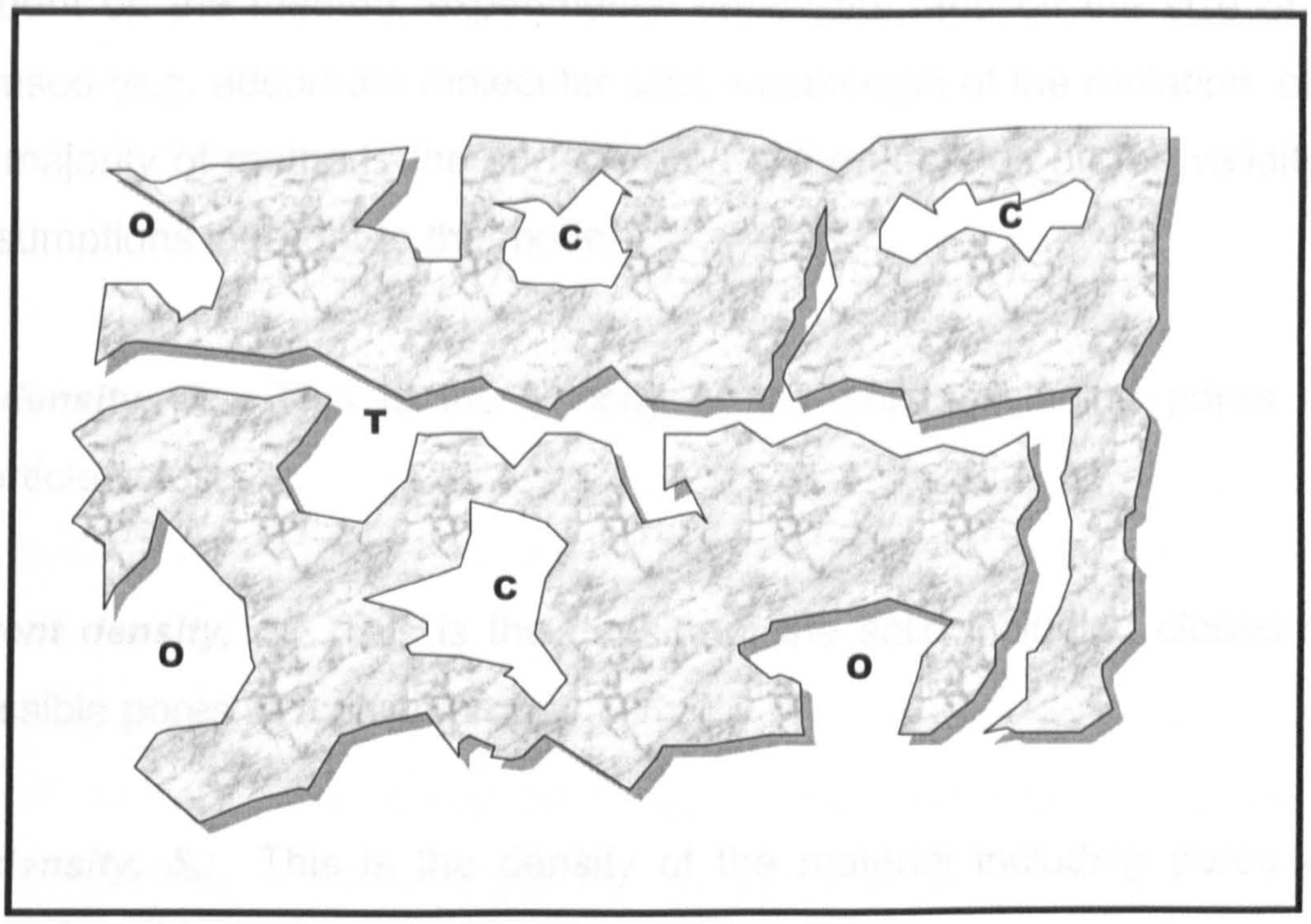

Figure 2.1: Model of possible pore types found in an irregular porous material. **O** : open ; **C** : closed ; **T** : transport passage.

-Pore size distribution, PSD: It is represented by the derivatives of area (A_p) or volume (V_p) as a function of radius (r_p) of the porous system [97].

$$PSD \equiv \frac{dA_P}{dr_P} \; or \; \equiv \frac{dV_P}{dr_P} \qquad \textbf{(2.1)}$$

-Porosity, ε : This term is defined as ratio of the total pore volume V_p to the apparent volume V of the sample. The value of V_p and V depends of the method used for its determination, size of the molecular probe either in fluid displacement or adsorption methods or of the yardstick in stereology method [97].

$$\varepsilon = {V_P}/{V} \qquad \textbf{(2.2)}$$

-Specific surface area, a, a_p or S: This parameter is the accessible or detectable area of solid surface per unit of mass of material. Its value is

dependent on the method, experimental conditions, and on the size of the probe used (e.g. adsorbate molecular size, wavelength of the radiation, etc.). In the majority of methods the surface area value depends on the validity of the assumptions inherent to the model.

-True density, δ_t: This is the density of the solid excluding pores and interparticle voids.

-Apparent density, δ_a: This is the density of the solid including closed and inaccessible pores to a given probe.

-Bulk density, δ_b: This is the density of the material including pores and interparticle voids.

In the last chapter it was stated that wide variety of carbons basically have a structure modelled as a three-dimensional network resulting of the bonds between the imperfect sections of graphitic lamellae which presents low density of packing, and cause spaces or voids between the lamellaes constituting the porosity with widely different sizes and shapes of these spaces trapped between the lamellar constituent molecules of the network. This model, the most accepted, supports not only the mechanisms of formation of microporous carbons but also the molecular sieve properties found in some carbons. Consequently, the carbon structure is closely related to the microporous system. This means that the porosities form part of both the adsorption system and the transportation system.

Many experimental and modelling works to acquire knowledge of pore structure, surface area and pore size distribution of carbons have been undertaken. The inherent or developed porosity of chars must be characterised because the shape or size of the pores affects their physical and chemical properties for example; density, surface area, strength, or reactivity. Also, these properties determine the future industrial use of these

materials. However the different techniques individually give incomplete information and there is a need to correlate this information with the variations of reactivity in important process of coals and coal chars, e.g.: combustion, carbonisation, gasification and, liquefaction [35,57,75,101,102].

For technical purposes it is important to know the porous structure of the carbon parental material just after pyrolysis and how it changes in reactive atmospheres. During activation of the char closed pores may become open; micropores of different sizes and shapes are known to be sources of structure heterogeneities of activated carbons [103]. An important commercial group of carbons are active carbons. They are used as activated adsorbents, filters, catalyst supports, molecular sieves and in numerous others applications. Their industrial use is determined basically by the characterisation of its porous structure and the surface area [104-106]. In new applications of carbon materials such as in low pressure methane storage, the most important characteristics in these carbons are high levels of microporosity (~ between 0.76 to 5 nm) and low levels of meso- and macroporosity, which will be carefully measured [107-111].

According to the aims of this research, the techniques; gas adsorption, small angle scattering (SAS) and spectroscopy of annihilation of positrons (PAS) will be described in the next sections. A brief account on their application on carbon materials is included.

2.2 GAS ADSORPTION ANALYSIS

Detailed information about of the porosity in solid materials with surface irregularities and internal pore system can be probed by gas adsorption. This process occurs when a solid surface (*adsorbent*) is exposed to a gas or vapour (*adsorptive*) below the critical temperature of gas. In this condition the concentration of the gas/vapour at the solid surface (i.e. within a molecular or atomic distance) is greater than in the gas/vapour phase. Then

an excess of molecules exit at the interface and the gas/vapour molecules can be condensed on the surface of the adsorbent, now the gas/vapour is named *adsorbate*.

The adsorption process depends upon the absolute temperature (T), the pressure (*P*), and the interaction potential (*E*) in the vapour-solid interface. Usually, the temperature is kept constant; therefore the amount of gas adsorbed (*W*) is function of only two factors, *P* and *E* [112].

$$W = f(P, E) \qquad (2.3)$$

As a result, a plot of *W* versus *P* at constant temperature is called the *adsorption isotherm*. The adsorption process is characterised by a decrease in entropy (ΔS) and free energy (ΔG) of the system under investigation. Then, from Gibbs function,

$$\Delta G = \Delta H - T\Delta S \qquad (2.4)$$

It follows that enthalpy (ΔH) in this process is a negative quantity. Therefore the adsorption is an exothermic process which increases with decreasing temperature.

A strong interaction between the solid and the gas is named *chemical adsorption or chemisorption*. It is characterised by the irreversible bonding of the gas with the surface at temperatures above of the critical temperature of the adsorptive which releases high heats. When the interaction is associated to low heats of adsorption and the quantity of gas adsorbed can be fully desorbed (reversible process) is termed *physical adsorption or physisorption*. In this case no structural changes occur at the surface of the solid, because there are no chemical bonds formed. In contrast to chemisorption (monolayer coverage), physical adsorption can produce more than one layer of adsorptive and increases with increasing pressure and decreasing

temperature [112,113]. The forces responsible for the adsorption are van der Walls or London dispersion forces. Using chemisorption it is possible to obtain the number of centres of reaction of a material, while using the physical adsorption of a gas on the solid the surface area is obtained.

Normally, the physical adsorption rate is high, but when the adsorbent is essentially a microporous system the adsorption rate may be restricted by the molecular diffusion rate [103]. The information related to porosity in solids is contained within the adsorption isotherm. However, this information is not absolutely able, on the contrary, it is necessary an interpretation of adsorption behaviour in order to produce a model of the pore structure. Hereafter, this review describes the most relevant theories or experimental assessments on the adsorption process.

2.2.1 The Langmuir Theory

Langmuir [113], using the kinetic theory of gases, described the adsorption of a monolayer of gas on the surface of a solid, thus,

$$N = \frac{P\,N_A}{(2\pi\ RTM)^{1/2}} \qquad (2.5)$$

Where: *N*; is the number of molecules joint each cm^2 of surface per second.
P; is the adsorbate pressure
N_A; is Avogadro's number
M; is the adsorbate molecular weight
R; is the gas constant
T; is the absolute temperature

The number of molecules adhering to each cm^2 of surface is,

$$N_{ads} = KP\,\theta_o\,A_1 \qquad (2.6)$$

Where: K; is equal to $N/(2\pi R T M)^{1/2}$

θ_o; is the fraction of the surface unoccupied
A_1; is the condensation coefficient and represents the probability of a molecule being adsorbed upon collision with the surface

Similarity, the rate of desorption of the molecules each cm^2 of surface is,

$$N_{des} = N_m P \theta_1 \gamma_1 e^{-E/RT} \qquad (2.7)$$

Where: θ_1; is the fraction of the surface occupied by the adsorbed molecules
N_m; is the adsorbate amount needed to cover the surface layer of the adsorbent
E; is the energy of desorption
γ_1; is the vibrational frequency of the adsorbate normal to the surface when adsorbed

At equilibrium, the rates of adsorption and desorption are equal, and $\theta_o = 1-\theta_1$; yields,

$$\theta_1 = \frac{K P A_1}{N_m \gamma_1 e^{-E/RT} + K P A_1} \qquad (2.8)$$

It is defined; $\kappa = \frac{K A_1}{N_m \gamma_1 e^{-E/RT}}$ (2.9)

Then; $\theta_1 = \frac{\kappa P}{1+\kappa P}$ (2.10)

For one layer of coverage,

$$\theta_1 = \frac{N}{N_m} = \frac{W}{W_m} \qquad (2.11)$$

Where: *W*; is the weight of gas adsorbed.
Wm; is the weight of gas adsorbed in the monolayer

Finally, the Langmuir equation can be obtained,

$$\frac{W}{W_m} = \frac{\kappa P}{1+\kappa P} \quad or \quad \frac{P}{W} = \frac{1}{PW_m} + \frac{P}{W_m} \qquad (2.12)$$

A plot of *P/W* versus *P* will give a straight line with slope 1/ *Wm* and an intercept 1/ *KWm* , where *k* and *Wm* are calculated. The surface area (S_t) of the sample is obtained from,

$$S_t = N_m A = \frac{W_m A_1 \overline{N}}{\overline{M}} \qquad (2.13)$$

Where: *A* and *M* are the cross-sectional area and the molecular weight of the adsorbate

This equation describes only one isotherm with the assumption that the adsorption is limited to one monolayer. In other words, the adsorption energy, *E,* is assumed constant, which implies a surface with a uniform energy.

2.2.2 The Brunauer, Emmett and Teller (B.E.T) Approach

The interaction between a solid surface (adsorptive) and adsorbed gas (adsorbate) will be changed when a gas monolayer is completed, the amount of change depends of the binding energy distribution to the solid surface but this is normally assumed to be heterogeneous.

The first quantitative theory, Langmuir, considered monolayer adsorption but, this was replaced by BET method (Brunauer-Emmett and Teller) which takes account of multilayer adsorption [112]. The isotherm plot present the relationship between the relative pressure (*P/Po*, where *Po* is the saturated vapour pressure of adsorbate at the temperature of operation), and the

amount of gas adsorbed. The shape of these plots usually, fall into one or other of the five patterns modelled by BET theory [99,110,112].

The BET isotherm may be expressed as,

$$\frac{P/Po}{Vads[1-(P/Po)]} = \frac{1}{VmC} + \frac{C-1}{VmC} P/Po \qquad (2.14)$$

Where: *Vads* is the NTP volume of gas adsorbed at *P/Po*
Vm is the monolayer coverage volume
C is a constant

Experimentally, the data for the isotherm can be obtained from either the static or dynamic system, using volumetric or gravimetric measurement of gas amounts. Nitrogen is the most widely used adsorbate. The plot of *P/Po* against *(P/Po) / {Vads[1-(P/Po)]}*, should yield a straight line. From this plot the monolayer volume is deduced, *Vm* = [1/slope + intercept on the ordinate)]. In order to calculate the slope and intercept, it is recommended to use P/Po limits between 0.05 and 0.25. Surface area may be calculated from *Vm*; the nitrogen cross sectional area is usually taken as 0.16 nm^2.

2.2.3 The Kelvin equation

The shape of gas adsorption isotherms is affected by the presence of pores. The basis of the methods to calculate the pore size distribution is the Kelvin equation, [112,113]

$$\ln\frac{P}{Po} = -\frac{2V\gamma}{rRT} Cos\varphi \qquad (2.15)$$

Where, *V* is the molar volume of liquid adsorbate filling the pores
r, is the porous radius
φ, is the angle of contact between liquid and pore walls It is usually assumed that the liquid wets the pore walls, then $cos\varphi = 1$

This equation was developed to account for the variation of vapour pressure over surfaces of varying curvature and when applied to the filling of pores might not be expected to give high accuracy. The slope of a plot of *Vads* against *r* gives the pore size distribution; *Vads* is the volume of all pores filled of radius up to a radius *r*. Each value of r in the Kelvin equation has an associated value of *P/Po*.

There is an increase in the thickness of the adsorbed layer on the walls of pores of radius greater than *r* as *P/Po* increases but the Kelvin equation does not take into account this complex factor. The use of so-called t-plot method has been proposed to solve with this [112]. This method assumed that pores are either slit-shaped or cylindrical with a distance apart of sides *d* and with a Kelvin radius r_k, related by

$$d = r_k + 2t \qquad (2.16)$$

Where, *t* is the multilayer thickness

Using the assumption on pore shape, *d* can be calculated and r_k is obtained from the Kelvin equation.

While t-plot is valuable tool in the characterisation of mesoporosity, it is not used to investigate microporosity.

2.2.4 The Dubinin Approach

It was found experimentally that micropores tend to fill with adsorbate at low relative pressures ($P/P_o < 0.3$). This phenomenon is associated to enhanced adsorption energy (dispersion forces), resulting from the proximity of the pore walls, as compared to the corresponding values for large and mesoporous or non-porous adsorbents with a similar chemical nature. [114,115] Dubinin and co-workers in order to explain these results extended the Polanyi potential

theory of adsorption [116] to produce the theory of volume filling of micropores, named as TVFM [117,118].

The Polanyi theory of adsorption is based on the function of the adsorption potential, ε, given by

$$\varepsilon = RT\ln\left(P_o/P\right) \qquad (2.17)$$

Where, P being the equilibrium and P_o the saturation vapor pressures of the adsorbate at a given temperature T
R being the molar gas constant

It was reported that the curve of ε versus $a^*\upsilon$, (where a is the adsorption and υ the molar volume of the adsorbate) is temperature-invariant for a given adsorbate-adsorbet system. That is

$$\varepsilon = f(\omega) \qquad (2.18)$$

Where ω is the volume of the adsorption film, and justify the adsorption by temperature-independent dispersion interaction for microporous solids.

Dubinin et-al, refused to interpret of the value of ε, as the adsorption potential, because that is mean that in the adsorbent pores there is an equipotential surface on which the adsorbate pressure is equal to P_o. Then, they assumed that the function ε was a differential change of free energy (ΔG) during the reversible isothermal transfer of a mole of the adsorbate from a bulk liquid to an indefinitely large amount of adsorbent, i.e.,

$$P = \left(\partial \Delta G / \partial T\right)_{av} \qquad (2.19)$$

This equation represents the theory of physical adsorption of vapours and gases in microporous solids (expressed by Dubinin as TVFM), which excludes the concept of the surface coverage and formation of successive adsorption layers proposed by B.E.T (see section 2.2.2). After these considerations, the principal thermodynamic function is defined as "differential maximal molar work of adsorption", or *A*. It is equal with a minus sign to ΔG.

$$A = -\Delta G = RT \ln\left(P_o / P\right) \qquad (2.20)$$

Now, according to the equation 2.17 it is obtained,

$$\left(\frac{\partial A}{\partial T}\right)_{av} = 0 \qquad (2.21)$$

$$\left(\frac{A}{A_o}\right)_{av} = \beta \qquad (2.22)$$

The equation 2.19 expresses the temperature-invariant of the characteristics curve of adsorption, $A = f(w)$. And, the equation 2.20 shows that at equal filled volume of the adsorption space *w*, the ratio of *A* of a given vapour to the differential molar work of adsorption A_o of the vapour chosen as standard is a constant value, named β or affinity coefficient of the characteristic curve.

Here, it is possible deduced the so-called Dubinin-Radushkevich (D-R) equation:

$$\frac{w}{w_o} = \left(\exp - k\frac{A^2}{B^2}\right) = \exp\left[-B\left(T/\beta\right)^2 \log\left(P_o/P\right)\right] \qquad (2.23)$$

In this equation, *k* is a constant and w/w_o is the fraction of the total adsorption volume w_o filled at any value of *A* (or ΔG). β is the adsorbate affinity coefficient. Benzene is usually employed as standard value, $\beta_{C6H6}=1$. The

value *B* is a qualitative measurement of the relative average micropore sizes of the adsorbent.

A number of experimental evidence was shown by Dubinin and co-workers, where the Equation 2.21 adequately describes, over wide pressure range, the adsorption of adsorbates on microporous carbons, both activated and unactivated [114]. However, deviations from linearity were shown at low values of $\log^2(P/P_o)$, and was concluded that this equation fits active carbons, which at low grades of burn-off have a homogeneous micropore distribution [119-121]. Also, the same was found for polar adsorbates which have van der Walls forces dependent of the temperature [122].

In the case that the adsorbate-adsorbet system obeys the D-R equation, that is, a plot of log (w) against $\log^2(P_o/P)$ should be rectilinear, the micropore volume w_o is taken from where the line intercept, when the x=0 axis, and the constant *B* can be obtained from the slope.

The overall range of linearity of the DR plot is reduced as the microporous size distribution is widened. Then, the value of *B* that is related to the size of the micropore is only average value and it is not expressed the intrinsic micropore distribution. Therefore if the D-R equation gives non-linear plot as a result of very narrow energy distribution is proposed to replace the square term in the D-R equation by a variable exponent *n*, [118,123]

$$\frac{w}{w_o} = D\log^n\left(P/P_o\right) \qquad \textit{(2.24)}$$

This equation is so-called Dubinin-Astakhov or D-A. The term *n*, usually takes values between 1 and 3, and experimentally it was reported n=1 for non-porous or mesoporous solids solids and n>2 for a non-homogeneous distribution of pore sizes [124,125], e.g. for molecular sieves general values tend to 3 [123].

An alternative method to Equation 2.24 was proposed to overcome with the limited use of D-R plot to carbonaceous adsorbents with homogeneous micropore structures. In this approach it is suggested that for nonhomogeneous carbons the overall isotherms is best fitted by the sum of individual D-R contributions of the type, [126]

$$W = \sum W_{oj} \exp\left[- B_j \left(T/B \right)^2 \log\left(P_o/P \right) \right] \qquad (2.25)$$

Where, *Woj* and *Bj* characterised each pore group

In a general expression this sum can be replaced by the integral

$$W_{(y)} = \int_0^\infty f(B) \exp\left[- B.y \right] dB \qquad (2.26)$$

Where, *f(B)* is the distribution function of the micropore volume with respect to B, and the variable y is defined by,

$$y = \left(T/B \right)^2 \log^2\left(P_o/P \right) \qquad (2.27)$$

This procedure had been applied with variable success on pure active carbons using a normalised gaussian function as *f(B)* [127].

2.2.5 Gas Adsorption to Study Porous Carbons

The development of porosity in carbons and chars is of interest because the accessibility of reactive gases to the structure might be a controlling factor in reactivity. Gas adsorption measurements have been widely used for determining the surface area, volume of pore and pore size distributions of a variety of carbon materials, such as graphites, carbon blacks, activated carbons, chars, coal coke, pitch coke and recently synthetic high porous carbons, like fullerenes and nanotubes. Due to the fundamental applications of these materials in industrial processes it is essential that this technique provides a standard procedure for the physical quantities derived. However, as was shown in Chapter 1, the final structure of these materials depends on

various factors such as heterogeneity of the original material and different preparation treatments which lead complex surfaces to be analysed. Not all adsorbates respond to these structural variations in the same form, consequently this is the major source of disparity in results. The limitations of applicability of each selected model or adsorptive, must be considered [99,113].

In this matter, macropores are transport pores to the interior of the particles and considered as external area which do not influence the adsorption process. Then, the high interest in carbons is to describe the adsorption occurring into of meso- and micropores. High temperature used in the carbonisation process of the precursors of graphites, carbons and chars normally results, in non-porous materials. It has been reported that activation or gasification at low degrees, on these solids develops considerable amounts of micro- or mesopores [37,45,46,106,128]. Also it is found that carbonised materials may exhibit a molecular sieve effect having low N_2 surface area and high CO_2 surface area values [37].

The Figure 2.2 shows the six different types of isotherm shape that are obtained from adsorption experiments [99]. Commonly, microporous carbons give type I isotherms, typical example is the adsorption of nitrogen on microporous carbon at 77 K. Carbon essentially mesoporous generally have type IV isotherm shape which exhibit a hysteresis loop as a result of capillary condensation. Non-porous carbon produces type II isotherm, as consequence of monolayer coverage followed by multilayer adsorption at higher *P/Po* values. A mixture of meso- and microporosity can also result in a type II isotherm. The type VI isotherm shape had been reported in the adsorption of krypton at 90 K on the carbon blacks with surface area small than 4 m^2g^{-1}. This isotherm characterises highly homogeneous, non-porous surfaces in carbons such as graphites and carbon blacks.

The evaluation of mesoporosity size is usually derived on the application of the Equation 2.15 (Kelvin equation) using various mathematical procedures to get the pore size distribution, [129] which is showed in the plot $\Delta V_p / \Delta d_p$ versus d_p (where d is the parallel-sided slit, Equation 2.16). In order to apply this method, it is necessary to assume that the pores are rigid and of uniform shape, the pore size distribution is restricted to the mesopore range (20 to 50 nm), there are no pore blocking effects and that the multilayer adsorption follows true capillary considerations. In practice, this method is subject to a number of uncertainties when is applied to majority of activated carbons because of the wide distribution of pore size, including micro- and macropores. It is possible derived the total mesopore volume if type IV isotherm has a clear plateau at high P/Po (i.e. ~0.95), but only few active carbons at high burn-off give a well defined mesopore character.

The deal in porosity characterisation in carbons is the description of the microporous systems of these materials. Various adsorbates have been used for characterising the microporosity and the properties of adsorption such as; nitrogen, carbon dioxide, argon, propane, isobutane, n-butane, neopentane, isooctane or 2,2-dimethylbutane [106,103,130]. The low-pressure parts of adsorption isotherms are used to obtain micropore distributions. The BET equation is used when nitrogen is selected as the adsorptive, while Dubinin theory is preferentially, used for the analysis of carbon dioxide isotherms [37,130]. It was found that the adsorption isotherms of nitrogen, carbon dioxide, benzene and cyclohexane, on high microporous carbons, were fitted by the Dubinin-Astakhov equation [131].

Some active microporous carbons have been shown that the adsorption of N_2 increased with the rise of the adsorption temperature. This behaviour had been attributed with the activated entry of adsorbate molecules through very narrow pore entrances or constriction. Despite that CO_2 and N_2 have no very different molecular dimension, 0.30 and 0.28 nm respectively, it is found that in active carbons that the uptake of CO_2 at 273 or 298 K is much larger than

the amount adsorbed of N_2 at 77 K. In this case is obvious to attributed to CO_2 molecules sufficient kinetic energy to overcome the energy at the pore entrance but, it is known that CO_2 molecule has a high quadrupole moment and that the presence of ions or polar groups in the microporous carbon surface may be influence the adsorption performance [132-133].

It was found an empirical relationship between the characteristic energy, *Eo*, and the mean micropore width, *L*, for a series of microporous carbons using the DR equation [134-136].

$$L_p E_o = Constant \qquad (2.28)$$

In fact, it was found that the pores are widened as the level of burn-off is increased and, it was assumed that *Eo* decreased as consequence of pores were turned more accessible to adsorbate molecules. Thus, it was reported two different empirical approachs according to the characteristic energy calculated in the adsorption process,

When, $20 < Eo < 42$ (kJmole^{-1}) [134,135]: $L_{(nm)} = \frac{10.8}{(E_0 - 11.4)}$ **(2.29)**

And when, $Eo < 20$ (kJmole^{-1}) [136]: $L_{(nm)} = \frac{24}{(E_0)}$ **(2.30)**

There are various methods proposed to evaluate the micropore size distribution. One common procedure uses a selection of molecular probes of different size and shape. With this technique it is only possible to probe the pore width up to the dimension of the largest available adsorptive molecules, i.e. 0.8nm [137]. Molecular sieve carbons have been successfully characterised by this method. The use of the Equation 2.25 to get pore size distribution of microporous carbons have been criticised because the distribution function could be influenced by defects or different functional

groups on the carbonaceous surface, and such contribution is not feasible to resolve from micropore potential addition [138-140].

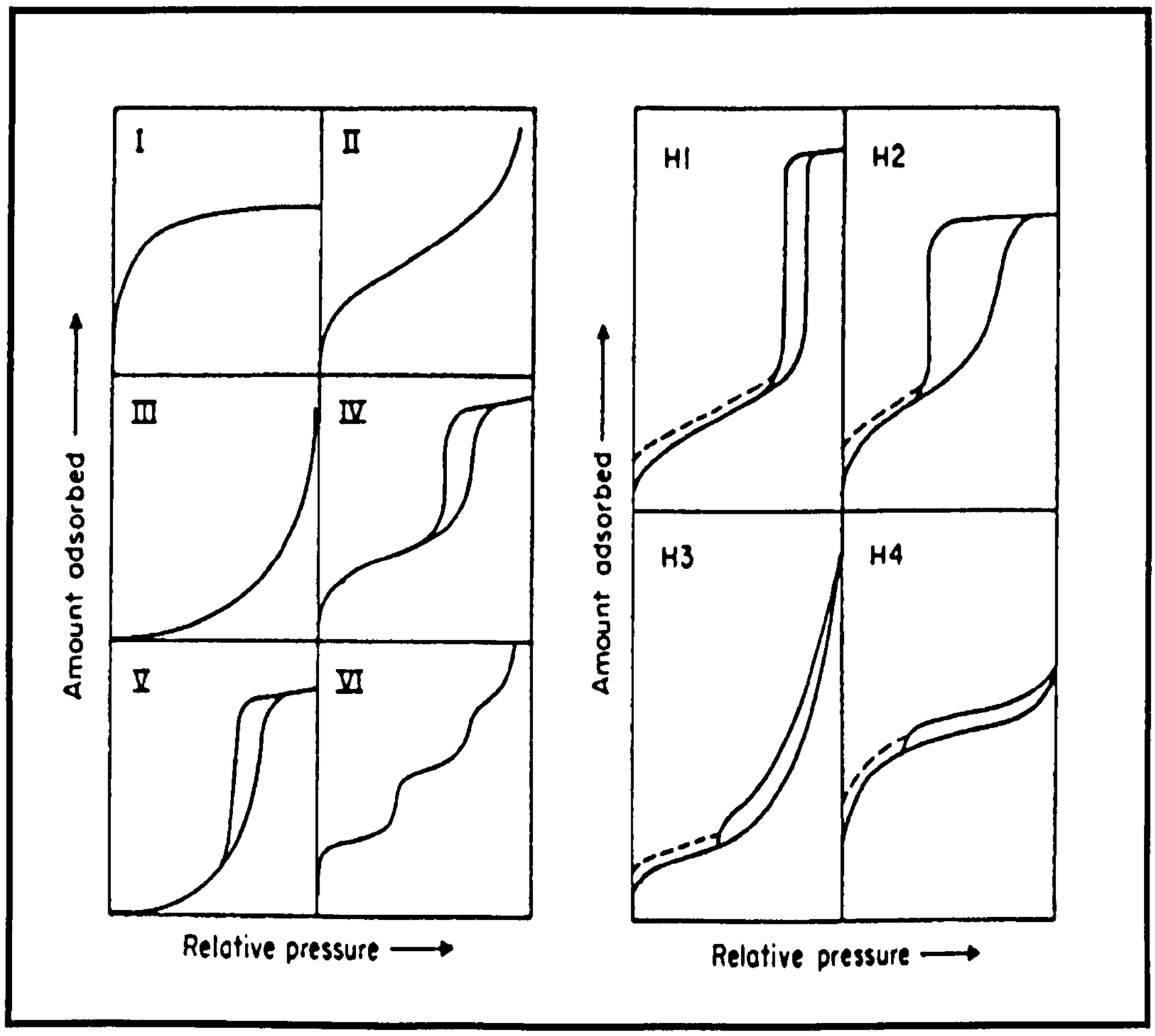

Figure 2.2 : This diagram shows the different types of gas adsorption-desorption isotherms (I to IV) and hysterisis loops (H1 to H4) [99]

2.3 SMALL ANGLE SCATTERING (SAS)

In small-angle scattering (SAS) techniques the sample is exposed either to a beam of monochromatic X-ray (SAXS) or neutrons (SANS). The typical wavelengths are ranging from 0.05 to 0.24 nm, and the scattered flux, Z, is measured in units of counts per second as function of the scattering angle $2\theta < 5°$. SAS occurs when small objects having a density which differs from the density of the surrounding medium, i.e. the intensity pattern depends on the

phase difference between coherent neutron or X-ray waves scattered at different points in a sample. Small-angle scattering experiments are non-destructive analysis and provide average information about of size range of 1 to 200 nm [141-145].

The X-ray wavelength is λ=0.229 nm for CrK_α and λ=0.154 nm for CuK_α. The incident energy of the waves, E, is of the order ~10^4 eV, which is much higher than the electron binding energies. The electrical component forces the electrons to oscillate in form of inductive dipoles, which generate spherical coherent electromagnetic waves at same frequency as the X-rays. This interaction is an exchange of energy phenomenon and it is of the type elastic photon scattering. The X-ray coherent scattering intensity is maximal at $2\theta = 0$ and decreases with increasing 2θ.

On the other hand, neutrons have no charge, the mass is slightly greater than the mass of a proton, the spin is ½ . Neutron decays into a proton and a neutrino with a half-life time of 10.7 min. Neutrons which are in equilibrium with a moderator at 300K have a mean energy of 25 MeV with a velocity mean, v=2200 ms^{-1}, a mean de Broglie frequency of 1.1 x 10^{13} s^{-1} , and mean wavelength λ=0.18 nm. Thermal neutrons have λ<0.25 nm and for cold neutrons λ>0.25 nm, it is referred to the temperature of the moderator used to slow down fission neutrons (T = 12 K for a mean value of λ=0.9 nm). The wavelengths mainly used for a nuclear reactor-based SANS ranging between 0.4 and 1.6 nm [145].

Thermal neutrons penetrate several centimetres through most materials depending on atomic number. The other hand, X-rays penetrate well through of materials with a low atomic number, but only tens of micrometers through metals. As a result of the small flux of neutrons beams the typical experiments take to be run on the instrument from hours to days, while X-ray beans is orders of magnitude stronger (~10^4) which leads to very rapid collection of data to get adequate statistics.

The scattering process is characterised by a reciprocity law, which is a relationship between particle size and scattering angle [141,146,147]. When a solid material is penetrated by x-rays their electrons resonate with the frequency of the x-rays and emit coherent secondary waves which interfere with each other and also, have the same energy (differ only by their phase; $\varphi = 2\pi/\lambda$ times the difference between the optical path and some reference point, it is function of the position of the electron). The scattered wave is coherent with respect to the incident wave if scattering occurs without energy exchange and phase shift. This event takes place when small scattering angles are considered, that is $2\theta < 5°$.

Figure 2.3 shows the calculation of the phase φ as function of the incident (*So*), and of the scattered beam (*S*); the vector r is the path to a point *P*, against origin *O*. The path difference of the point *P* against to the origin is *r(S - So)*. Then, the vector *q* is the change in the wave vector *So* due to scattering [141,146].

$$q \equiv S - S_o \tag{2.31}$$

It is deduced that the magnitude of (*S*-*So*) is,

$$|S - S_o| = 2\sin\theta \tag{2.32}$$

Consequently, the magnitud of *q* is |*q*|,

$$|q| = q = 2|S_o|\sin\theta \tag{2.33}$$

And for elastic scattering where |So| is equal to |S|,

$$|S_o| \equiv 2\pi/\lambda \tag{2.34}$$

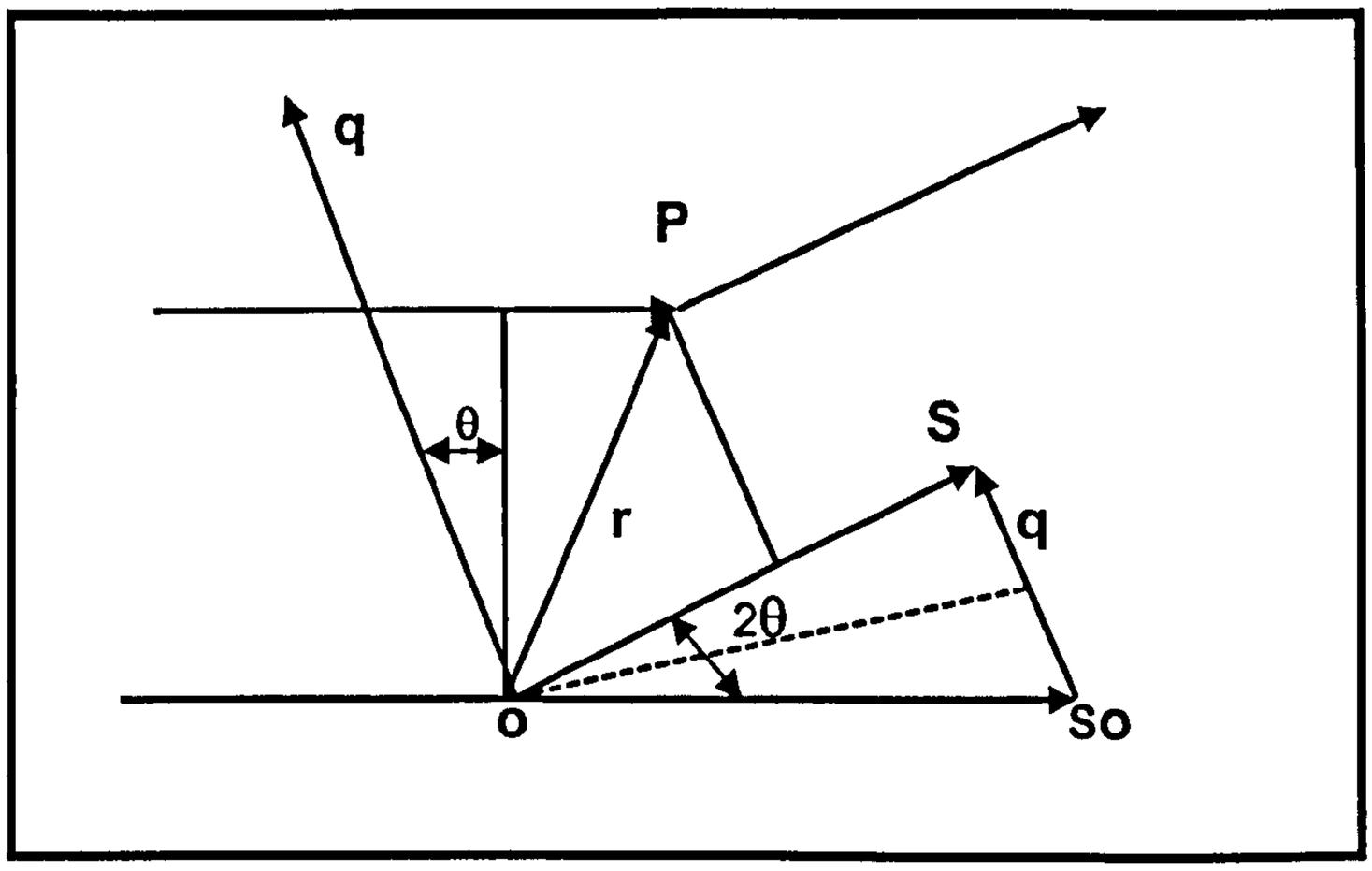

Figure 2.3: Scattering by two point centres; θ means half the scattering angle, **r** is a vector from the origin to a point **P**, against the origin **o**, **S** and **So** are the incident and scattered beans respectively

And for elastic scattering where ISoI is equal to ISI,

$$|S_o| \equiv 2\pi/\lambda \qquad (2.34)$$

From Equations 2.31, 2.33, and 2.33 is obtained that,

$$\varphi = (2\pi/\lambda) r (S - So) = -qr \qquad (2.35)$$

And, finally the mathematical expression for *q* is,

$$q = 4\pi \sin(\theta)/\lambda \qquad (2.36)$$

In the direction zero of the scattering angle, all the waves are in phase and the scattering intensity is a maximum.

The scattered wave is coherent with respect to the incident wave if scattering occurs without energy exchange and phase shift. The constant, *b*, is known as the bound atom, coherent scattering length. It is proportional to the strength of the neutron/nucleus interaction and it depends on the spin state of

the nucleus and is defined to be positive for repulsion. The ratio of the time-averaged coherently-scattered energy flux and the incident flux is named differential coherent scattering cross section, $d\sigma/d\Omega$, where σ is the effective area for a neutron/nucleus collision.

$$\sigma = \int_0^{2\pi} \int_0^{\pi} \frac{d\sigma}{d\Omega} \sin\theta d\theta d\phi \qquad (2.37)$$

And,

$$\frac{d\sigma}{d\Omega} = b^2 \qquad (2.38)$$

The coherent scattering length density, ρ_b (cm^{-2}), is the sum of the coherent scattering length, b, for all nuclei in a volume element ΔV divided by ΔV. SANS is observed only if a specimen differences exist in the coherent scattering length density.

As with neutrons, the wave properties of X-rays are used in order to describe X-ray interactions with atoms. The differential scattering cross section, $d\sigma/d\Omega$, for scattering by one electron is defined as the ratio of the photon flux scattered (s^{-1}) into a solid angle $\Delta\Omega$ and the incident flux, Io ($cm^{-2}s^{-1}$). Then, an X-ray scattering length, b_x, for one electron is defined by

$$\frac{d\sigma}{d\Omega} = b_x^2 \qquad (2.39)$$

And the X-ray scattering length of one atom is:

$$b_x = zb_x \qquad (2.40)$$

Where z is the number of electrons in the shell

Then, the X-ray scattering length of one atom is known as the atomic form factor, F, for X-ray diffraction.

In general, the average of X-ray and neutron coherent scattering length density, ρ_{bx} and ρ_b, for a material is the number of X-ray or neutron coherent scattering lengths per unit volume for atoms of type j = 1, 2, 3.

$$\rho_b = \sum_j \frac{b_j}{\Delta V} = \sum_j b_j \left(\frac{\rho_m N_A}{M} \right) \qquad (2.41)$$

Where, ρ_m is the theoretical mass density
M is the molecular mass
N_a is 6.022×10^{23} mol^{-1}

It is conventional in materials to evaluate a macroscopic cross section, $d\Sigma /d\Omega$, defined as the cross section per unit volume of material. If the sample contains a sum of N atoms i, with atomic cross section $d\sigma /d\Omega$, and considering the Equation 2.41it is deduced that,

$$\frac{d\Sigma}{d\Omega} = \sum_1^N \left(N_A \rho_m / M \right) d\sigma / d\Omega_i \qquad (2.42)$$

So, summation can be replaced by integration over the volume V

$$\frac{d\Sigma}{d\Omega} = (1/V) \left| \int_V \rho_{(r)} \exp(iqr) dr \right|^2 \qquad (2.43)$$

Where, $\rho_{(r)}$ is the spatial density distribution at the position r

The second term is a function defined in a 3-dimensional space which is so-called form factor, $|F(q)|^2$. [144-146] $F(q)$ describes the shape of the scattered object in terms of their Fourier transform. Form factor has the value unity at $q=0$, and falls off with increasing q value width depending on the inverse of the scattering object size.

The macroscopic scattering cross section is obtained by Fourier inversion of the distance distribution function of the electrons or nuclei, $\rho_{(r)}$, as

$$\frac{d\Sigma}{d\Omega} = \int_0^{\infty} \rho_{(r)} \frac{\sin qr}{qr} dr \qquad (2.44)$$

To simplify notation, hereafter the expression for the macroscopic scattering cross section, $d\Sigma/d\Omega$, will be written as $I(q)$.

For a Two-phase system consisting of a dispersion medium and dispersed particles or pores with constant composition (dissolution) only the difference of the density of the phase1 or dispersed medium, ρ_1, minus the density of phase 2 or matrix, ρ_2, (i.e., $\Delta\rho$) can be proportional to the scattered amplitude and its square to the intensity. This density difference is named contrast, $C_{i,j}$. This approach is called *"two-phase model"* [142,146,148].

If all the particles in the material are identical, and spaced far enough apart that interference between them is negligible, is possible define N_p regions each of volume v_p, then the Equation 2.43 becomes

$$I(q) = C_{1,2}^2 (1/V) N_p V_p^2 \left|F(q)\right|^2 \qquad (2.45)$$

It means that scattering cross section is proportional to the contrast, $C^2_{i,j}$, the particle volume fraction $(N_p v_p/V)$, particle volume , and the function form factor.

When interference between particles is considered the $I(q)$ is proportional to an interference term named the structure factor, $S(q)$.

$$I(q) = C_{1,2}^2 (1/V) N_p V_p^2 \left|F(q)\right|^2 S(q) \qquad (2.46)$$

S(q) affects the q-dependence of the scattering intensity for smaller values of *q*, and the affected *q* values depend of the concentration of the system. That is, there is minimum effect by the examination of dilute systems.

In the most simple case, the single form factor, *F(q)*, is represented by a sphere of radius *Ro* and volume v, with uniform density. In this case the result has been given by, [146]

$$F(q)=(\Delta\rho)v^2\left[3\frac{\sin qR_o - qR_o\cos qR_o}{(qR_o)^3}\right]^2 \qquad (2.47)$$

The scattering intensity for a specimen volume *V* is,

$$I(q)=\frac{1}{V}(\Delta\rho)^2 v^2 9\left[\frac{\sin qR_o - qR_o\cos qR_o}{(qR_o)^3}\right]^2 \qquad (2.48)$$

The solution of the expansion of sin(x) and cos(x) functions for q=0 leads *I(q)* =1, then

$$I(q=0)=\frac{N_\rho}{V}(\Delta\rho)^2 v^2 \qquad (2.49)$$

Therefore the volume of the sphere can be obtained from scattering intensity data if the contrast term and volume fraction are known. According to the Equation 2.45, this fact can be generalised to any particle, unconditional of size or shape of the particle.

It is possible to obtain some parameters from the interpretation of the experimental data which describe the pore structure of the sample. Two methods of approximation are possible: *i)* To plot the data in such a way that linearity is obtained and the slope and intercept can be interpreted; *ii)* To fit a

calculated *I(q)* to the experimental one. But certain assumptions must be made about the structure of the sample, before each model can be applied.

2.3.1 The Guinier Approximation

From Equation 2.47 for the form factor in SAS considering spherical object structure the expansion of the sine and cosine functions to the fifth order in qR and considering $qR << 1$ gives [142,144,146]

$$F(q) = \exp\left(-q^2 R_g^2 / 3\right) \qquad (2.50)$$

And,

$$I(q) = (\Delta\rho)^2 v^2 \exp\left(-q^2 R_g^2 / 3\right) \qquad (2.51)$$

This is so-called Guinier law, where Rg is the radius of gyration of the scattered object. It is defined by analogy with mechanic as the radius of inertia or the root-mean square of the distances of all electrons or nuclei from their centre of gravity ($Rg = \sqrt{r^2}$). A plot of *ln(I)* versus q^2, *Rg* proportional to the square root of the slope of the tangent at small q (in the limited $q \rightarrow 0$). For example a sphere of radius *R*, the radius of gyration is

$$R_g = \left(\sqrt{3/5}\right) R \qquad (2.52)$$

For not anisometric particles, like ellipsoids or parallelepipeds, Rg can be obtained by

$$R_g^2 = V^{-1} \int_V r^2 d^3 r \qquad (2.53)$$

With r being the distance from the centre of gravity and V is the volume

According to the *Guinier law*, the behaviour of scattering at very small *q* is an intuitive way to distinguish between particle shapes. When there is large separation between the particles it is not possible to apply the Guinier interpretation of the small q-behaviour.

2.3.2 The Porod's Law

The *Porod's law* is followed when at largest *q* values the scattering intensity falling rapidly as q^{-4} [140,143,146,149]. Porod model assumed two phases of uniform electron or nuclei density and did not to consider shape, size or connectivity of the dispersed phase. So, the intensity will obey the expression,

$$I(q)=(\Delta\rho)^2\frac{2\pi}{q^4}\frac{S}{V} \qquad \textbf{(2.54)}$$

Where *S* is the total interfacial surface area with the scattering volume

A plot of $q^4I(q)$ versus *q* is called *Porod plot* and shows a straight horizontal line for large *q*. Porod behaviour is obtained only when the limited $qr >> 1$, *r* is the radius of the structure resulting in the scattering.

From Equation 2.53 is possible write

$$\int I(q)q^2dq=2\pi^2v_1v_2(\Delta\rho)^2 \qquad \textbf{(2.55)}$$

Where v_1 and v_2 are the volume fractions of the two phases

This integral is known as *Porod Invariant*, *Q*, because is independent of the shape of the scattering object [144,147,149]. One important use of the *Q* is for the measurement of the evolution of the void fraction of porous materials. But, the use of this equation to found the interfacial surface area of condensed materials is limited only to an isotropic scattering obtained from

sample. Normally in real systems deviations from q^{-4} behaviour are found. This means that the scattering intensity for a real system may show a Porod region but, the Porod's law cannot be a truly asymptotic law for a real system [147].

2.3.3 Fractal Concept to Interpret SAS

It have been found that some disordered or porous systems, including polymers, aggregates of particles, gels, zeolites and carbon materials exhibit fractal property or self-similarity [147,149-152]. This behaviour describes to a geometric characteristic of a structure with a correlation function which is proportional to the original function, independently of the magnification factor (ξ) used in the analysis, that is,

$$I_{(q)} \propto I_{(\xi q)} \qquad (2.56)$$

For any magnification factor, ξ
I (q) is a intensity probe function in terms of *q*

One quantity is proportional to a power of the other quantity, when *q* is large enough to satisfy that $\xi q >> 1$. In x-ray or neutron scattering, ξ is a length that characterises the size of the object producing the scattering.

$$I_{(q)} = I_o q^{-\alpha} \qquad (2.57)$$

Where *Io* and α are constant.

A fractal rough surface with Hausdorff dimension *Ds* and a fractal volume with dimension *Dv* are related to α by [144,147]

$$\alpha = \begin{cases} 6-Ds & surface\ fractal,\ with\ 3\langle \alpha \langle 4 \\ Dv & volume\ fractal,\ with\ \alpha \langle 3 \end{cases}$$

Previous works [147,153-155] have been reported fractal behaviour on porous materials from X-ray and neutron small-angle scattering using the next model [147,156]

$$I(q) = Io\ \Gamma(5-D_s)\ sin\left[\pi\left(D_s-1\right)/2\right]\ q^{-(6-D_s)} \qquad \textbf{(2.58)}$$

Where $\Gamma(5\text{-}D_s)$ is a gamma function

A double-logarithmic plot of $I(q)$ versus q that shows a linear graph at low q is evidence of a fractally rough surface. The surface fractal dimension Ds is determined by,

$$S = -\left(6-D_s\right) \qquad \textbf{(2.59)}$$

Where S is the plot slope

Fractal behaviour of the scattering at low q has been associated to meso- and macroporosity in a porous material [147]. In contrast, an ordinary surface which follows the Porod's law is described by a slope, $\alpha = 4$ which leads $Ds = 2$.

2.3.4 Scattering from Polydisperse Systems

A specimen that produces scattering data from a broad range of scattering objects is not possible to analyse according to the methods described above, for example the Guinier approach will be failed to yield a straight line in a wide q range. Then, a polydisperse system can be analysed assuming that the total scattering is a sum of the scattering from subsystems weighted according to the size distribution of the system. This kind of methods are based in three main steps; *i*) presumption of a structural form factor for the scattered objet, *ii*) calculation of scattering intensity distribution function and, *iii*) fitting of the experimental data to extract structural parameters, radius size.

In this approximation the variation of scattering intensity with the vector q is written as, [144,145,157-160]

$$I(q) = \int P(q,R)\, No\, f(R) dR \qquad \textbf{(2.60)}$$

Where, *P(q, R)* is the intra-particle structure factor
f(R) is the normalised size distribution function
R is the size of the scattering objects
No is the number of objects scattered

A scattering object of size *R*, *P(q, R)* is described by

$$P(q,R) = (\Delta\rho)^2\, G(q,R)\, (V_p(R))^2 \qquad \textbf{(2.61)}$$

Where *G(q, R)* is the scattering kernel
Vp(R) is the volume of the particle

If the average intra-particle structure form factor is normalised, that is $\langle \tilde{P}(0) \rangle = 1$, then it can be described as

$$\langle \tilde{P}(q) \rangle = \frac{\int G(q,R) V_p^2 f(R) dR}{\int V_p^2 f(R) dR} \qquad \textbf{(2.62)}$$

Where, $\langle V_p^2 \rangle$ is the second moment of the particle volume

And consequently, it is deduced that,

$$I(q) = (\Delta\rho)^2\, No \langle V_p^2 \rangle \langle \tilde{P}(q) \rangle = A \langle \tilde{P}(q) \rangle \qquad \textbf{(2.63)}$$

In this equation, *A* represents the prefactor about the concentration of scattering particles and will be treated as a fitting parameter in the model.

There are several distribution functions that is possible to use in modelling polydisperse solution of particles. One of them is the two parameter, $\bar{R}$ and z, unimodal *Schultz distribution* for spherical particles [160]. This was originally applied to obtain of polymer molecular weight distribution. The fraction of particles having an averaged particle radius $\bar{R}$, and z is a parameter that measures the width of the size distribution which is given by

$$f(R) = \left[R^z / \Gamma(z+1)\right]\left[(z+1)/\bar{R}\right]^{z+1} \exp\left[-(z+1)R/\bar{R}\right] \quad \textbf{(2.64)}$$

Where, Γ is the gamma function

In particular, the normalised intra-particle scattering factor, $\langle \tilde{P}(q) \rangle$ for spheres with a Schultz size distribution reads

$$\begin{aligned}\langle \tilde{P}(q) \rangle = 8\pi\alpha^{(z+1)} \Big\{ & \alpha^{-(z+1)} - (4+\alpha^2)^{-(z+1)/2} \cos(\xi_1) \\ & + (z+1)(z+2)\left[\alpha^{-(z+3)} + (4+\alpha^2)^{-(z+3)/2} \cos(\xi_3)\right] \\ & - 2(z+1)(4+\alpha^2)^{-(z+2)/2} \sin(\xi_2) \Big\}\end{aligned} \quad \textbf{(2.65)}$$

Where $\alpha \equiv z+1/q\bar{R}$ *and* $\xi_i \equiv (z+1)\tan^{-1}(2/\alpha)$

The polydisperse sphere approximation does not fit data at high *q* and it should be considered as a low-*q* range model, resulting in a good fit for scattering from microporosity.

2.3.5 Small-angle Scattering to Study Porous Carbons

Small-angle X-ray scattering and neutron scattering are powerful and well established techniques for the investigation of no regular or amorphous structures, like coal, carbons and chars [161]. A large number of models have

been proposed for the interpretation of data and subsequent modelling of the porous structures. In order to obtain clarity in describing the unknown structure of porous-carbon materials is necessary that the model by itself is used for both interpreting the scattering data and simulating mechanical or chemical transformations including adsorption, oxidation, combustion, gasification and pyrolysis of the porous material.

An analysis of the surface area as a function of conversion for gasification in CO_2 of a microporous carbon (Carbosieve-S) was carried out by small-angle X-ray scattering in the range for vector q between 0.03$Å^{-1}$ and 0.5 $Å^{-1}$ [157]. In this was reported that the intensity changed for the range q^{-4} to q^{-3} and it was associated to very large changes in the sizes of these pores with the conversion. Also it was found that a decrease in the average micropore size at initial stage of reaction followed by growth of the micropores with the conversion. An unexpected agreement between the size of pores determined by nitrogen adsorption and SAXS of a series of active fruit pit-based carbons prepared by combination of activation (by steam, at 1173 K) and by heat treatment (at 1523 K, 2 h under nitrogen) was found [162]. It was suggested that the diameter of micropores formed during the activation and the heat treatment have nearly the same size as the crystallites; the scattering data of some carbons satisfying Guinier and Porod approximations. In this case is possible to obtain the radius of gyration, *Rg*, and specific surface area.

An agreement was found in other work [163] between SAXS and carbon dioxide adsorption analysis for pine wood-based charcoals prepared at temperatures from 873 to 2873 K. In this case only below 1273 K was found an increase of CO_2 gas adsorption in contrast with a significant decrease of the internal surface area determined by SAXS. In the other range examined, (at high temperatures), both techniques showed similar trends, it was compared the filled volume with surface area from SAXS. The micropore size associated to the mean Rg increased from 0.4 to 3 nm with HTT ranging

from 1073 to 2873 K. Some prepared active carbons by oxidation were analysed using SAXS, [164] scattering intensity showed and slightly linear portion and a pronounced shoulder at high q values. The quasi linear region was attributed to polydisperse mesopores and the shoulder was ascribed to the high concentration of narrow microporosity. This shoulder increased with burn-off and the Rg from Guinier plot was estimated in approximately 1 nm. SAXS from CO_2 oxidised sucrose-based carbons were fitted by Guinier plots in a wide range of q [165]. The Rg was used to characterise the average pore size of the micropore region, the main characteristic of these materials. The Rg remained constant at 0.6 nm in the range of burn-off between 3.5 to 35 wt%.

The comparison of SAXS curves for three different active carbons showed a shoulder at higher q values [166]. Two carbons from anthracite charcoal and coconut charcoal exhibited multiple scattering at high q as well a commercial Carbosieve carbon but the intensity scattering for this sample followed a linear region in the Guinier plot with Rg=0.7 nm.

A SAXS study was carried out of active carbon fibers (ACFs) prepared from cellulose and polyacrynitrile (PAN) after filled with water the microporosity. The Rg increased and this was associated to the swelling of the micropores in the ACFs. The Rg was 2 and 2.7 nm for original cellulose- and PAN-based ACFc respectively and, this increase to 3 nm after water filling [167,168].

Some oxidised Carbosieves with a weight loss until 30 wt% after treatment showed a pronounced increase in the scattering intensity probably by microporosity development but the Rg was essentially constant at 0.4 nm [157]. Polyvinyldene chloride (PVC) based chars were oxided to weight losses of 28% and 80%, these samples showed a well defined high microporous system tested by argon adsorption at 77 K but, the mean width pore size from SAXS showed a no significant increase [169].

A lignite coal sample was modelled as a surface fractal SAXS, [147] it was found that this sample was a surface fractal with D=2.5, and described by a power law over a range of intensity of at least 10^7. Later, other work used the proposed Equation 2.58 to estimate the surface fractal (dimension D) on experimental SAXS data obtained in a set of porous carbon-based samples [152]. This work found a value of D=2.54 for the same sample reported in reference 147. D values for three activated carbons were 2.05, 2.08 and 2.21. It was shown also, that D values decrease as the rank of coal increase; between 2.25 for Durian high rank coal to 2.86 for Morwell brown coal. In the same study was found that D values decrease slightly with the degree of oxidation (at 100°C with oxygen) on Durian coal sample.

Much SAXS and SANS work has been reported regarding the development of microporosity in amorphous carbon structures obtained by pyrolysis of polymeric precursors at high temperatures [162,163,170-172]. In generally, it is found that as the heat treatment temperature is raised, pores grow in size and also, there is development of graphitic crystallinity in the matrix. The production of highly microporous materials is accompanied by significant amount of closed porosity.

An important part of the porosity in carbons or coal chars is inaccessible to gas molecules at room temperature and below, then adsorption methods cannot be applied to account the total porosity in these porous materials. A method based on contrast matching small-angle scattering (CM-SAS) has been developed to detect closed porosity in polymer resins [171,172]. This method also has been used successful applied on coals and coal chars [111,159,173]. It has shown that small-angle scattering from dry samples comes from three sources, open porosity, closed porosity and inter-particle scattering. This can be made through CM-SANS technique where hydrogenated and deuterated solvents are used selectively to produce a cancellation of the contrast factor ($\Delta\rho \cong 0$). Thus, SAS allows the possibility of studying the closed porosity separately, because both the solid phase and

void-filled volume which are contrast matched and then the remained scattering intensity is attributed coming from closed porous. CM-SANS in carbons is carried out with deutered hydrocarbons and deutered water, whereas halogenated hydrocarbons are necessary for CM-SAXS experiments.

2.4 POSITRON ANNIHILATION SPECTROSCOPY (PAS)

Positron physics is concerned with the interaction of low energy positrons with matter [174-177]. The existence of a positive-electron was predicted by P.A.M Dirac theory in 1930 and, soon after, it was detected by C.D. Anderson [176]. This is named as *positron* and symbolised, e^+.

The positron is the antiparticle of the electron, has the same mass but opposite charge. Positrons exist in small numbers and for short times. They can be generated by nuclear reactions such as radioisotope decay [177]. The most common source of positrons is sodium 22 which decays to neon 22 with the simultaneous emission of a positron and a gamma-particle (1.28 MeV). This γ -particle is known as the birth signal.

When the positron is injected into a condensed material it is annihilated by interaction with an electron present in the medium to produce two gamma-particles (0.511MeV). The time between birth signal and annihilation gamma-particles is the lifetime or τ . This overall process means, that the mass of the positron is converted to energy, according to the law of conservation of matter or $E=mc^2$ [176]. Figure 2.4 displays the positron annihilation experiment.

The annihilation rate is given by, [176]

$$\lambda = \pi r_o^2 c n_e \qquad (2.66)$$

Where r_o is the classical electron radius
c is the velocity of the light
n_e is the electron density

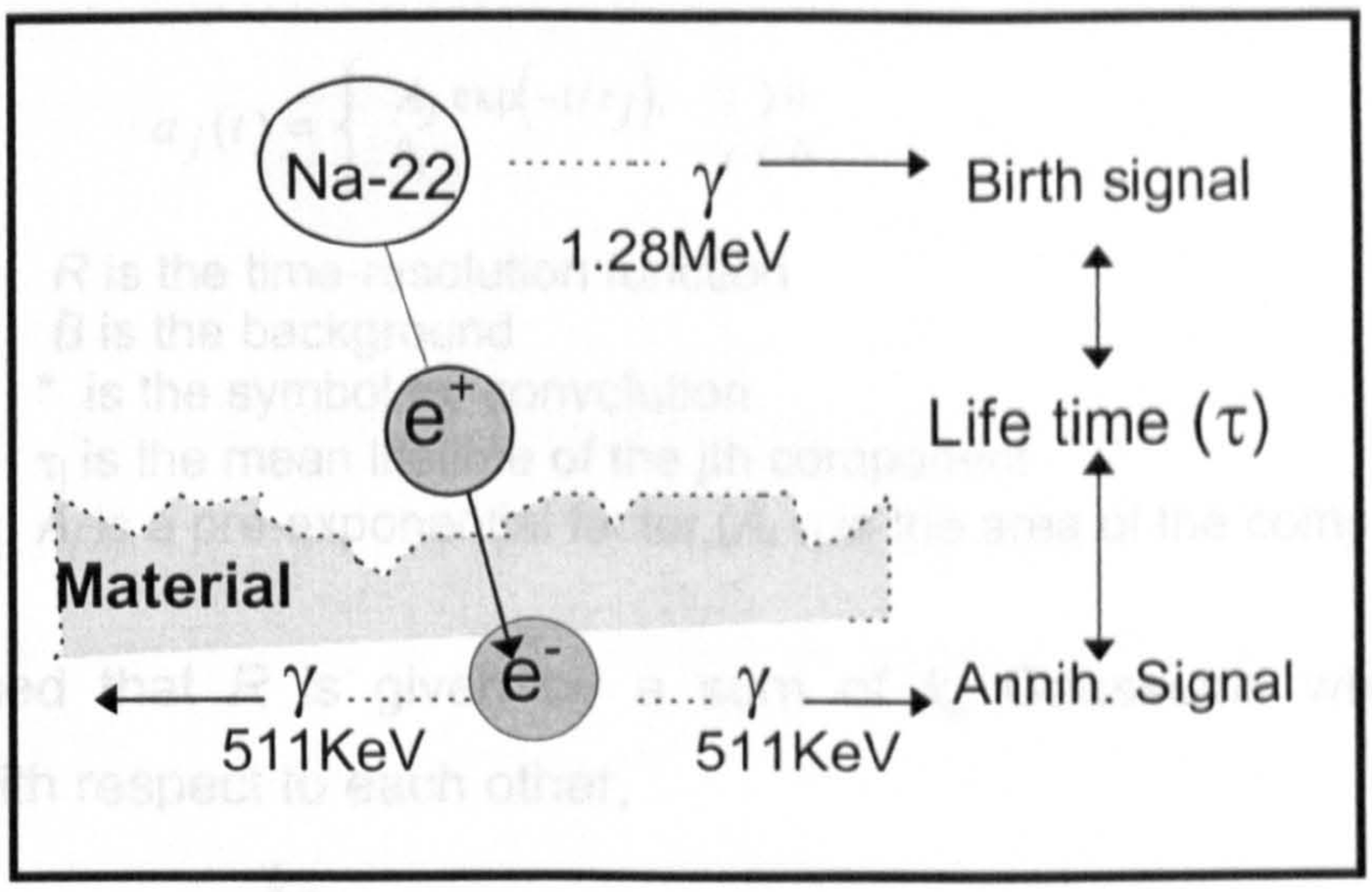

Figure 2.4 : Description of the positron formation and annihilation experiment

The inverse of λ is the lifetime (τ). Therefore, by measuring the annihilation rate the electron density of the material can be obtained. The positron annihilation spectrum is composed of all the distribution of positron lifetimes, as a result, this consists of many exponentially decaying curves, and then it needs a computer program to obtain each component of lifetime [174].

The ideal lifetime spectrum is of the form,

$$F(t) = \sum_i \lambda_i I_i \exp(-\lambda_i t) \quad and \quad \sum_i I_i = 1 \qquad \textbf{(2.67)}$$

Where λ_i and I_i are the annihilation rate and relative intensity, respectively, of the *i-th* component positrons

In these programs the model function consists of a sum of decaying exponential convoluted with the resolution function of the lifetime spectrometer plus a constant background,

$$f(t) = \sum_{j=1}^{ko} \left(a_j * R\right)(t) + B \qquad (2.68)$$

Where, *ko* is the number of lifetime components
a_j is the decay function for component *j*

$$a_j(t) = \begin{cases} A_j \exp\left(-t/\tau_j\right), & t \rangle 0 \\ 0, & t \langle 0 \end{cases}$$

R is the time-resolution function
B is the background
* is the symbol for convolution
τ_j is the mean lifetime of the jth component
A_j is a pre-exponential factor,($A_j\,\tau_j$ is the area of the component)

It is assumed that *R* is given by a sum of k_g Gaussians which can be displaced with respect to each other,

$$R(t) = \sum_{p=1}^{k_g} w_p\, G_p(t) \qquad (2.69)$$

Where, $G_p(t) = \frac{1}{\sqrt{2\pi\sigma_p}} \exp\left(-\frac{\left(t - To - \Delta t_p\right)^2}{2\sigma_p^2}\right)$ *(2.70)*

$$\sum_{p=1}^{k_g} w_p = 1 \qquad (2.71)$$

The Gaussian in the Equation 2.69 is centred on channel number *To* + Δt_p, where *To* is a reference channel number (called "time -zero") and Δt_p a displacement. The standard deviation σ_p of the Gaussian is related to its full width at half maximum ($FWHM_p$) by,

$$FWHM_p = 2(2\ln 2)^{1/2}\,\sigma_p \qquad (2.72)$$

There is evidence that a fraction of positron injected in the matter can remain trapped in surface states (τ_s) and defects (τ_d), such as vacancies or

dislocations [178]. In comparison with the lifetime of the free annihilation in the bulk (τ_b) it was found the follow sequence: $\tau_{b<}\tau_{d<}\tau_s$. In this case, from the Equation 2.66 is possible define the mean lifetime, τ_M.

$$\tau_M = \frac{\int_0^\infty t\ F(t)\ dt}{\int_0^\infty F(t)\ dt} \qquad (2.73)$$

For example, if two lifetime components are resolved by the computer fitting program (τ_1 and τ_2, with intensities I_1, I_2 respectively), the mean lifetime of the positrons annihilating in the sample is given by the transformation of Equation 2.72 in

$$\tau_M = \frac{(\tau_1 I_1 + \tau_2 I_2)}{(I_1 + I_2)} \qquad (2.74)$$

2.4.1 Positronium Formation

When a positron is injected in a molecular substance the thermalisation process will cause ionisation of an amorphous region of the medium with release of secondary electron which can form a bound positron-electron state. It was named *positronium* (*Ps*) by Ruark in 1937 and experimental evidence for the existence of the Ps system was obtained by Deutsch between 1949 and 1952 on the slowing down of positrons in nitrogen [175]. Also, positronium systems have been observed in other gases, liquids, solids, as well as in interstellar space.

In analogy to quantum mechanics of the hydrogen atom, [175] it is possible to predict two spin states for the positronium system which are called "*ortho, (o-Ps)*" and "*para, (p-Ps)*" for triplet and singlet, respectively. The *o-Ps* is originated when the spin of the positron and electron are formed a triplet

(spins are parallel), while the *p-Ps* is characteristic the singlet state (spins are anti-parallel). Typical lifetimes for positronium are 140 ns for ortho-positronium (*o-Ps*) and 0.125 ns for para-positronium (*p-Ps*). Collisions of the *o-Ps* with an electron with opposite spin of the surrounding media can be producing a process of annihilation called pick-off, or pick-off quenching [176,177].

The energy involves in the formation the positronium can be explained by three [174,175] models. The *Ore* and *Spur* models are considered inconsistent with each other.

One of them is the *Spur model* which postulates that the positronium is formed when a thermalised positron finds a secondary electron before the latter recombines with its parent molecular cation. In this step the positron has deposited its energy in discrete quantities (positron kinetic energy is assumed about 30 - 100 eV) producing ionisation of the molecules of medium, (radiation tracks or spurs are created) and simultaneously, the positron is completely thermalised. According to this model, the critical distance between the charges to form a stable bound state at which the potential energy of the e^+e^- pair equals the thermal energy kT is named r_c. This is

$$r_c = {e^+ e^-}\Big/{\varepsilon kT} \qquad (2.75)$$

Where, ε is the static dielectric permitivity of the medium
kT is the thermal energy

And, the probability of positronium formation, P, is defined by

$$P = 1 - \exp\left(-{r_c}\Big/{r_m}\right) \qquad (2.76)$$

Where, r_m is the mean thermalisation distance of the e^+ in the medium

Other model is the *Ore*, which assumes that the positronium is formed when an electron from a molecule of the medium is extracted, but only if a gap is produced during the slowing down of thermalisation of the energy of the positron and no other electronic energy transfer process is possible. The probability of formation of positronium depends on the energy of the e^+ thermalising within the energy gap, called Ore gap which is defined from E_I - 6.8 eV < E< E_I. Here, E is the kinetic energy of the e^+, E_I is the ionisation potential of the medium and 6.8 eV is the binding energy of the positronium.

A third model for positronium formation is the *free volume* model [179]. This model is based on decay of positronium which takes place in vacancies and other open spaces named *free volume*, which are spaces with low electron density. This predicts that the positronium can be only formed in a free volume which is larger than a certain critical value, but different to Spur and Ore models it cannot explain the energy at which the positron picks up an electron to form the bound state or positronium. In particular, molecular solids have a large number of imperfect sites, such as impurities, defects, voids, grain boundaries, etc. which leads to a high fraction of positronium trapped in microvoids [180]. A relationship between the *o-Ps* state and void size is obtained from the overlap of the o-Ps density in the microvoid and the electronic density in the surrounding medium [179,181]. In this sense, a semi-empirical equation was proposed which the *o-Ps* in a spherical void with radius R is trapped in the potential well with infinite barrier height and with the radious $Ro = R + \Delta R$, where ΔR is a empirical parameter describing the penetration of the *Ps* wave-function into the bulk [182,183].

$$\tau_{o-P_S} = \frac{1}{2}\left[1 - \frac{R}{R_o} + \frac{1}{2\pi} Sin\left(\frac{2\pi R}{R_o}\right)\right]^{-1} \qquad (2.77)$$

Where, τo-p is expressed in ns
R is the void radius in Å
ΔR is the empirical electron layer thickness, equal to 1.66 Å

2.4.2 Positron Annihilation Studies In Metals

In perfect metals positrons diffuse around in a delocalised state. Normally, the annihilation rate, which is proportional to the electron density at the site of the positron, is enhanced by a factor between 4 and 30 from of the unperturbed value, as a result of the masking of the positrons by electronic conduction. Reported lifetimes in metals are between 100 and 400 ps. For example, in nearly free-electron metals it varies from 170 ps in aluminium to 420 ps in cesium [174,184].

It is noticed that the deformation (vacancies, vacancy clusters or dislocations) and heating of metals produce remarkable changes in the annihilation characteristics. They are attributed to positron trapping in the deformations which are regions of less than average electron density [174,175,177,178, 181,184]. The annihilation characteristics depend on the type of defect in which the positron is localised, therefore important consequences can be deduced, i.e. the concentration of defects may be obtained of the proportion of trapped and free positrons, local properties of the defects (e.g. internal electronic structure, vacancy agglomeration), can be deduced.

2.4.3 Positron Annihilation Studies in Organic Materials

These materials have been studied in amorphous and crystalline forms by positron techniques. When positrons are injected in a molecular media a high fraction of them form positronium (20-70%, [175]). This is important, because the lifetime of ortho-positronium can be measured more precisely than the shorter lifetime of the positron. Studies on positronium can be made by using a slow positron beam which has a well defined energy. Positronium is attracted to regions of lower electronic density and it can become trapped in vacancy-type defects in molecular crystals. Thus, the formation and annihilation process of Ps in these materials depend on their chemical and physical characteristics.

The free volume is defined as vacancies or open spaces in molecular solids which serve as points for Ps formation. A relationship between the free volume and the Ps pick-off rate was found; hence, a large free volume results in a long Ps life-time [181,184]. Also, the o-Ps lifetime is affected by the packing arrangement in solids. Various phase transformations including solid-liquid, solid-solid, liquid crystal mesophases, and glass crystalline transitions have been studied by positron spectroscopy; specially attention have been on plastic phases. A plastic phase is characterised by a lower density that produces a longer o-Ps lifetime and a sharp change of the spectral signal is observed at the transition temperature [181].

2.4.4 Positron Annihilation Studies in Polymers

Polymers are molecular materials which have been under wide investigation by positron annihilation spectroscopy. At least three different life-times can be obtained from the polymer spectra ($\tau_1 \cong 0.3$ ns, $\tau_2 \cong 0.7$ ns, $\tau_3 \cong 3$ ns). The longest one is thought to be due to pick-off annihilation of *o-Ps*, the shortest is attributed to p-Ps and free positrons in the bulk. The origin of the intermediate life-time is not clearly understood. The most accepted explanation attributes it to positrons which have not formed positronium but are bound to lower density amorphous regions [174].

Lifetime measurements of different positron states are widely used to investigate the free volume size or voids and glassy state in amorphous polymers. That means; that the probability of formation of Ps is proportional to the number density of free volume holes present in the polymer [181,185-192]. Positron annihilation was used to probe various amberlite XAD resins (styrene-DVB or acrylic ester used as macroreticular adsorbents) with different pore sizes and surface areas. A correlation between the intensity of the long-lived o-Ps (~30ns) and the surface area was found [186]. Hole volume distributions were determined from the measurements of o-Ps

lifetime distributions in an epoxy polymer (DGEBA/DDH/DAB) with Tg = 62°C, at temperatures between 25 and 150°C [187]. It was established that the distributions were changed to larger radius as the temperature increased.

As was noted before, positron lifetimes in polymers show a sharp change at the glass transition temperature (Tg). An early work found that the o-Ps annihilating on polystyrene samples (with different molecular weight) depends upon the free volume, because an increase of the Tg with molecular weight was observed. However the Tgs obtained were 13°C below that measured by differential scanning calorimetry [188]. In a series of studies of temperature versus different cross-linked epoxy polymers was found that the steepest of o-Ps lifetime occurred at the glass transition temperature where the free volume underwent a maximum value. The Tg obtained by this technique is 1 to 5 degrees less than those determined by differential scanning calorimetry (DSC) [185]. Similarly, results were found in a copolymer of p-hydroxybenzoic acid, (HBA) and poly(ethylene terephthalate), (PET) where the o-Ps lifetime showed that the free volumes increases from 0.05 to 0.1 nm^3 in the temperature range between 30 and 230 °C; accordingly, the results were confirmed by DSC [184].

2.4.5 Positron Annihilation Spectroscopy to Study Porous Carbons

Not many positron investigations on carbonaceous materials have been performed in spite of the fact that positron annihilation spectroscopy should be able to provide useful information on the properties of these materials which have a wide industrial application. Essentially, the research has been limited to study of the graphites with different degrees of crystallinity.

A positron lifetime study based on the trapping model was performed to characterise the defects in different types of graphites (such as: glassy carbon, artificial graphite, pyrolytic graphite and natural graphite) [193]. It was found that the lifetime of the free positrons delocalised in the perfect graphite

lattice was 215 ps while, in a well-crystallised pyrolitic graphite and natural graphite was 400 ps; in this case, it was attributed to positrons trapped at the internal surfaces between crystallites. Other work on graphite powders, grafoils and pyrolytic graphite crystals with different surface areas performed in the range between 25 - 600°C reported correlation between the intensity of surface-trapped positrons (with a lifetime component ~ 0.45 ns) and the surface area and also, between Ps formation and surface area of the graphites [194]. A short-lived component (~0.2 ns, due to positrons in the bulk) and a long-lived component (~2 ns, of o-Ps in the voids) were found. Additionally, it was observed using angular scattering of electron-positron annihilation that the degree of fall of the intensity curve (I(θ)) at θ=0 for carbon black and glassy carbon was substantially different, probably as a result of the quality and anisotropy of the graphite single crystal [195].

More recently, a comparative positron spectral study between graphite powders and C_{60}/C_{70}-buckminsterfullerenes [196] reported three lifetime components for the graphite: 0.237ns (I_1= 75%), 0.455ns (I_2=24%) and 88 ns (I_3=1%). The longest life-time was attributed to o-Ps in the voids. Only one lifetime was found for the C_{60}/C_{70} powder at 0.393ns, it was assigned to free positron annihilation without forming Ps states.

A work that presented preliminary testing of active carbon fibres produced from polyacrylonitrile precursor by positron annihilation found only one lifetime component ranging from 373 ± 1 to 441± 1 ps [197]. Two important conclusions were extracted. For one of them, it was observed that the positron lifetime increased with the temperature of heat treatment of carbon fibres (from 1250 to 1800 °C) in comparison with a reduction of the total pore volume while the mean pore width rose. The other one, it was found that the oxidative chemical treatment of carbon fibres produced a decrease of the positron lifetime. As a result, the authors considered a positron annihilation near-surface region and trapping of positrons in a one type of defects at approximately 400 ps. It was assigned to trapping of positrons in pores.

However, a previous work found two lifetimes for PAN- and pitch-based carbon fibres [198]. Two PAN-based carbon fibres made from high and low modulus fitted in a short lifetime at 250 ps with intensity about of 25% and long lifetime about 400 ps. Surface treatment on the PAN-based carbon fibre reduced the short lifetime to about 150 ps and its intensity decreased about 13%. The long lifetime remained unaffected. This surface treatment was not described in the mentioned paper. Pitch-based carbon fibre exhibited the same two lifetimes, but the intensity was about 50%.

Positron annihilation analysis of Illinois #6 coal powder (Argonne Premium Coal Bank) and the same coal after extraction with pyridine in order to remove low molecular mass fractions showed two lifetime components. The lifetimes for original material were 0.345 ns and 0.746 ns and, for the extracted coal were 0.345 ns and 0.843. It was suggested that the extraction of low weight material increased the long lifetime slightly as result of a reduction in the electronic mobility [199]. This preliminary work showed that positron techniques could be useful to extract information of the micro-structure of coals and related materials.

2.5 SUMMARY

It is clear that all adsorbents used in gas adsorption to characterise porous carbons give different porosity information. However, general characteristics can be obtained. The gas adsorption of N_2 or CO_2 is a fast analysis that approximates for the pore system predominant but the uncertainty increases if the analysis is on high heterogeneous porous carbon or a mix of porous materials. The qualification of the isotherm forms is an essential tool and must be the first step in the characterisation of any carbon. This work found useful the quantification of the isotherm data (volume adsorbed versus P/Po) in terms of surface area from N_2 adsorption and microsurface area from CO_2

adsorption as a comparative measurement in the evaluation of the development of porosity in the activation or carbonisation of carbons.

Concerning with this matter is necessary to be consistent with the experimental conditions used. This review-work found appropriate to carry out N_2 adsorption at 77 K assuming a molecular cross-section of N_2 molecule as 0.162 nm^2 and the range of P/Po to fit the isotherm data BET approach (Equation 2.14) between 0.06 and 0.2. In the case of CO_2 adsorption it is recommended to use as molecular cross-section 0.187 nm^2, the saturation pressure of the affinity coefficient (β) as 0.461 to fit the data with DR-Equation 2.23. The calculus of pore width using Equations 2.29 and 2.30 will be carried out on essential microporous carbons with very narrow pore size distribution (isotherm type I, Figure 2.2) in order to compare with Small-angle Scattering and Positron Annihilation Lifetime Spectroscopy.

X-ray or neutron beams constitute a useful tool to probe porous carbons because they are non-destructive incident radiation which provides average information about of scattering objects in the size range of 1 to 200 nm according the variation in the density contrast factor between solid and porous phases. Therefore, total porosity is sensed for low or high volume fractions without any consideration of pore size, pore constrictions or interactions of probe with the bulk carbon structure. SAXS from coalchars is affected by the presence of mineral species, especially heavy atoms such as iron and calcium. Also, gases trapped into micropores contributed to the intensity scattering data. SANS experiment, contrasting to SAXS is free of any of these considerations in the study of porous carbons. Its limitation concerns the restricted access to neutron sources.

Analysis of SAS at high q range senses the microporous system. Homogeneous microporous carbons had been fitted by Guinier approach, where Rg calculated is a direct measure of the pore size. However the majority of porous carbons, that are heterogeneous pore systems, do not satisfy the Guinier condition, i.e., $q.R_g << 1$.

At relatively low q range, where the Porod's law can be applied, is possible obtain information of the total surface area but only if q^{-4} decay in the intensity scattering is followed. Although, not many works have reported this behaviour in carbons, the Porod Invariant as a measurement of the surface area, is usually calculated in order to follow pore development in gasification.

The closed porosity can be obtained by SANS comparison between dry and wet experiments, using C_6D_6 or C_7D_8 to fill the open porosity.

3. OBJECTIVES

The main objective of this work was to investigate the porosity of gasified carbon materials by means of positron annihilation spectroscopy, and to compare and contrast that information with that obtained by gas adsorption and small angle X-ray and neutron scattering techniques.

Specific Objectives

To carbonise Saran polymer and two Argonne Premium Coals (Pittsburgh and Illinois). To gasify the carbonised samples using air, carbon dioxide and steam in order to obtain different levels of burn-off.

To characterise the porosity of active carbons, activated coal chars, and also a pitch based active carbon fiber by conventional methods such as N_2 and CO_2 gas adsorption, as well as by small angle X-rays (SAXS) and neutron scattering (SANS) techniques.

To characterise the activated carbons, carbon fibers and coal chars by means of positron annihilation lifetime spectroscopy, (PALS).

To propose mechanisms that can help to understand the development of porosity carbons and chars from different origin and activated with different agents.

4. EXPERIMENTAL SECTION

A variety of carbon-based materials was pyrolysed and then activated with air, carbon dioxide and steam. They were characterised by gas adsorption, Small Angle Scattering, (SAS), and Positron Annihilation Lifetime Spectroscopy, (PALS). The overall production and characterisation is summarised in Figure 4.1.

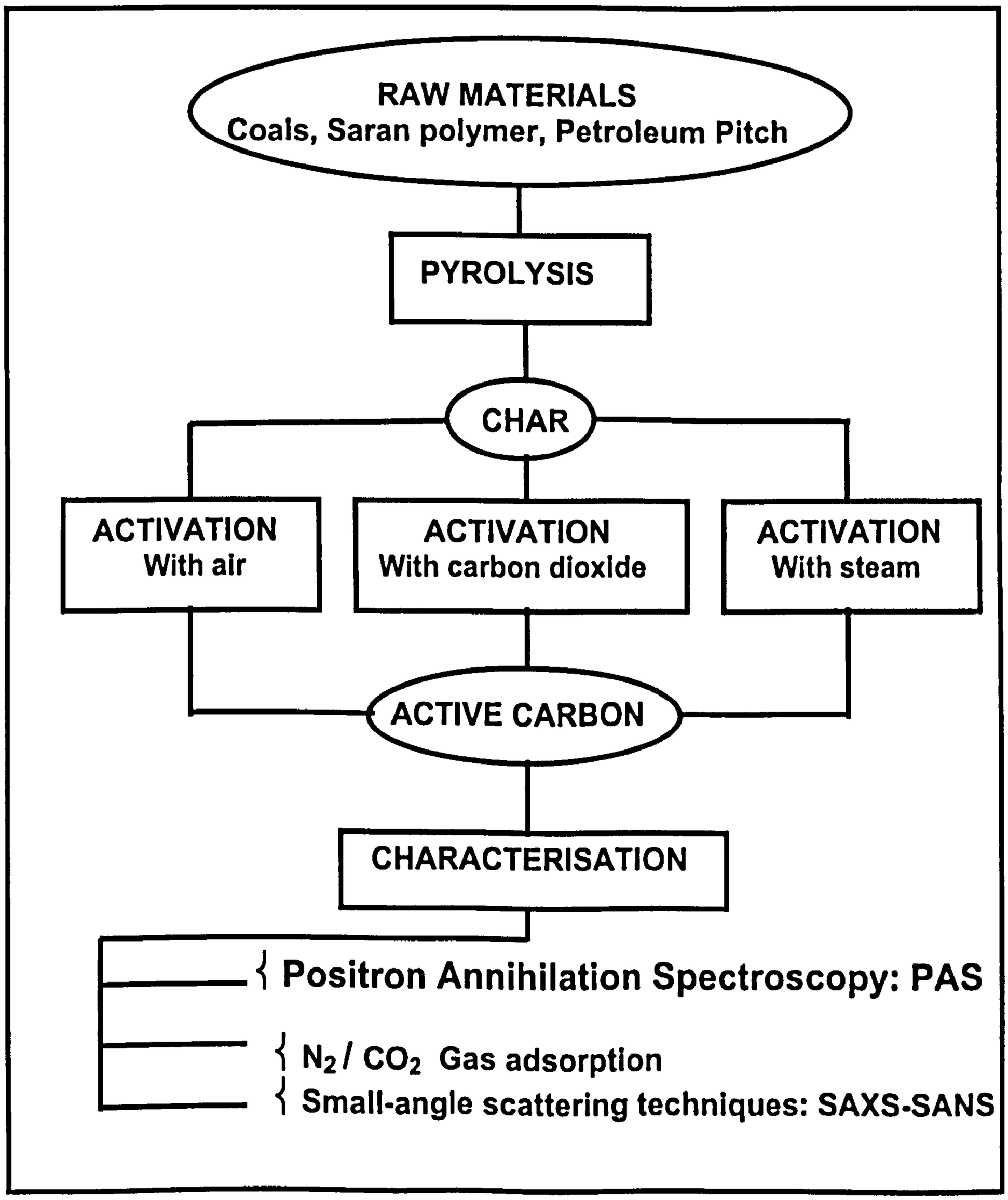

Figure 4.1: Chart showing the experimentation proposed in this work

4.1 SAMPLES

4.1.1 Saran Carbon Precursor

Saran was used as precursor to obtain a polymer-based carbon. The raw material is a granulated copolymer produced by *Aldrich* (CAS No. 25038-72-6) which corresponds to poly(vinylidenechloride-co-methyl acrylate). The chemical structure representation for the monomer is

$$(\text{-}CH_2CCl_2\text{-})_x[\text{-}CH_2CH\text{-}(CO_2CH_3)\text{-}]_y$$

This is a transparent and almost colourless thermoplastic, with extremely low permeability to gases, with an average molecular weight of 90000, the melting point is 152 °C, the density is 1.780 [200]. Poly(vinyldenechloride) $-(CH_2.CCl_2)_x-$ decomposes with the evolution of hydrogen chloride accompanied by molecular reorganisation or crosslinking to form an almost pure carbon. Decomposition has been observed to proceed at temperatures as low than 100 °C, the reaction releases one mole of hydrogen chloride per unit of monomer. [201-203] The carbon thus prepared has a low level of impurities and therefore a catalytic effect during gasification reactions has been ruled out. [204-206]

4.1.2 Carbon Fibre Precursor

General-purpose carbon fibres (CF) were prepared from a commercial isotropic petroleum pitch. The process included spinning, stabilisation and carbonisation in nitrogen at 1273 K of the pitch fibers. [207,208] These samples were provided by the Inorganic Chemistry Department of the University of Alicante, Spain. Two series of activated carbon fibers have been prepared by gasification with steam and carbon dioxide at 1160 K. The true, (ρ_{He}), and apparent, (ρ_{Hg}), densities were measured as 2.1 and

1.1 gmL^{-1}, respectively. Then, the total pore volume is 0.43 gmL^{-1} from $V_t = 1/\rho_{Hg} - 1/\rho_{He}$.

4.1.3 Coal Samples

The coals used were obtained from the Argonne Premium Coal Sample program [209]. These samples are good reference materials; they have stable chemical and physical properties. Their elemental analyses are shown in Table 4.1.

Table 4.1: Elemental analysis of coals in wt %[209]

SAMPLE	RANK	C %	H %	N %	O % *	S %	ASH %
Pittsburgh # 8	High Volatile Bituminous	75.50	4.83	1.49	6.63	2.19	9.25
Illinois # 6	Subbituminous	65.65	4.23	1.16	8.60	4.83	15.48

Notes: % dry basis, *Oxygen by difference.

Main mineral composition reported for the Argonne Premium Coals [209,210], after low temperature ashing analysis (LTA), are presented in Table 4.2. A complete high temperature analysis (HTA) [209] of major elements in the ash is presented in Table 4.3. The ash percentage values measured by LTA are higher than those measured by HTA.

Table 4.2: Main mineral composition for used coals (total mineral matter basis)

SAMPLE	Total mineral matter (LTA%)	Quartz (wt%)	Pyrite (wt%)	Calcite (wt%)	Total Clay (wt% by diff)
Pittsburgh # 8	10.9	16	22	5	57
Illinois # 6	18.1	19	30	10	41

Tables 4.2 and 4.3 shows that the main inorganic elements in Pittsburgh coal ash are aluminium, silicon and iron. While in Illinois coal ash are silicon, aluminium, iron, calcium and sulphur.

Table 4.3: Major elements in coal ash, expressed as oxides

Elements	Pittsburgh # 8 (wt%)	Illinois # 6 (wt%)
Ash	9.2	16.2
Al_2O_3	25.2	18.3
BaO	Nil/Trace	Nil/Trace
CaO	2.6	7.9
Fe_2O_3	19.5	18.0
K_2O	2.1	2.9
MgO	1.3	1.2
MnO	Nil/Trace	Nil/Trace
Na_2O	0.0	0.0
P_2O_5	0.0	0.2
SO_3	2.0	6.8
SiO_2	45.9	43.7
SrO	Nil/Trace	Nil/Trace
TiO_2	1.2	1.0

(dry ash basis)

Another important analysis is the maceral composition of the coals. Table 4.4 shows the mineral matter free percentage of liptinite, vitrinite and inertinite. These macerals could be related to the gasification reactivity.

Table 4.4: Maceral composition reported for the coals used [209]

SAMPLE	Liptinite (wt%)	Vitrinite (wt%)	Inertinite (wt%)
Pittsburgh # 8	7	85	8
Illinois # 6	5	85	10

(dry coal basis)

4.2 PREPARATION OF CARBONS

4.2.1 Carbonisation

Pyrolysis of Saran and coal samples was carried out in a horizontal tube furnace reactor controlled by a *Eurotherm* device. The sample was weighted (5-8 g) and loaded into a silica boat, and placed in the furnace. The sample was purged with a dry high purity nitrogen stream (~ 100 $mLmin^{-1}$) at least for two hours. The nitrogen gas was previously dried and

oxygen traces removed using Chrompack-7970/7971 traps. The sample was then heated to 1173 K a rate of 10 K min^{-1} and held at this temperature for one hour. The char thus obtained was cooled under a nitrogen atmosphere to room temperature, and then removed from the furnace and weighted. The carbonisation yield of sample was then calculated. The char was then ground in a porcelain mortar until the entire sample was sized to < 250 μm. A lay out of the equipment used is shown in Figure 4.2.

4.2.2 Air Activation

Carbon and coal char samples were activated in the same furnace used for pyrolysis (see Figure 4.2). Sample was weighted and loaded into silica boats, the tube reactor was purged with high purity nitrogen stream at least for two hours at room temperature. Then, the temperature was increased to 673 K at a rate of 10 K min^{-1} under a nitrogen flow. A dry air stream (100 mL min^{-1}) was then introduced and nitrogen flow was turned off. The time for the activation was between 0.25 and 5 hours, in order to obtain different values of burn-off. The air flow was then turned off and the furnace was cooled under a nitrogen atmosphere. When the run was finished the char was removed and weighted and the burn-off percentage was calculated.

4.2.3 Steam Activation

Samples were activated in a horizontal quartz tube reactor (see Figure 4.2). The sample was weighted and loaded into a quartz boat. The system was purged with high purity nitrogen for two hours at room temperature. The sample was heated under dry nitrogen up to 1173 K at a rate of 10 Kmin^{-1}. Then a wet nitrogen stream at a controlled flow rate of 100 mLmin^{-1} was introduced. The water vapour was produced in a flask heated at 353 K by an oil bath. The wet nitrogen stream was admitted to the system. Activation of the chars was carried out at different times in

order to obtain several degrees of burn-off. After this has been accomplished the water vapour was stopped and the reactor was cooled under dry nitrogen. The active carbon was removed and weighted to calculate the percentage of burn-off.

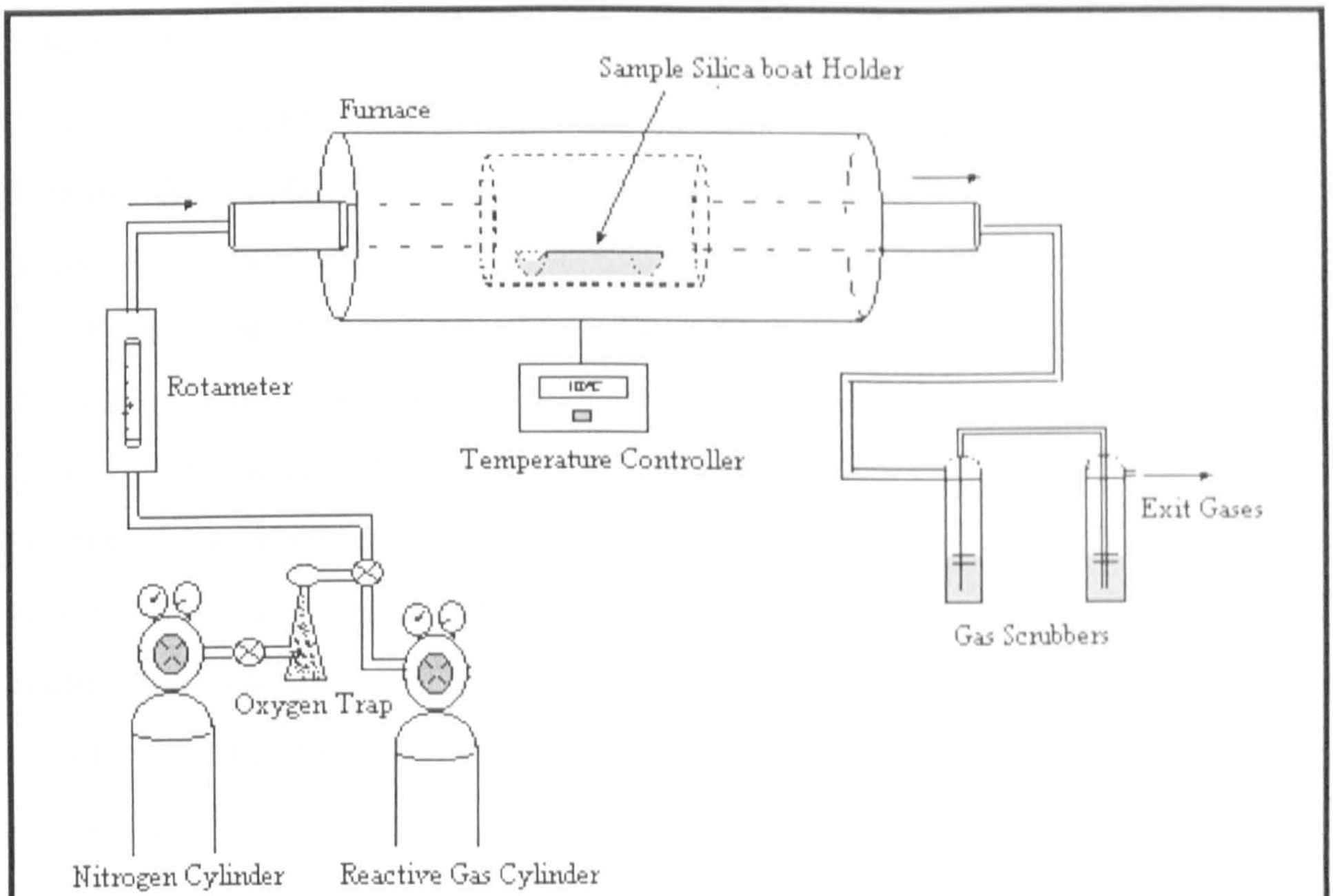

Figure 4.2: Gas supply and furnace arrangement for pyrolysis and activation of the samples

4.2.4 Carbon Dioxide Activation

Carbon and coal char were gasified with carbon dioxide in the horizontal reactor shown in Figure 4.2. Sample was loaded in silica boats in the furnace and purged during two hours with pure nitrogen at room temperature. The furnace was heated to 1073 and 1173 K, for coal chars and carbon respectively, under nitrogen stream at a rate of 10 K mL^{-1}. Once the temperature reached a steady state a flow of pure carbon dioxide at 100 mL min^{-1} was admitted to furnace. The activation time was between 0.25 and 9 hours to vary the degree of burn-off. The furnace was cooled at room temperature under nitrogen. The active carbon thus obtained was weighted to determine the burn-off level.

4.3 CHARACTERISATION OF THE ACTIVATED CARBONS AND COALS CHARS

4.3.1 Nitrogen and Carbon Dioxide Adsorption

The determinations of BET surface area and pore size distribution by nitrogen were performed in a *Micromeritics ASAP 2010* unit [211]. Carbon dioxide adsorptions were carried out in a *Quantachrome Autosorb-6* apparatus. The sample was out-gassed under high vacuum for 14 hours at 523 K, in order to remove all the physisorbed species from the surface of the adsorbent. The weight of the out-gassed sample was measured at room temperature; typical quantities used were between 0.15 and 0.3 grams. The warm and cold free volumes were measured previous to the adsorption experiment with helium. Then, the sample was-out gassed under high vacuum for 2 hours at 523 K, and then cooled down to the liquid N_2 temperature (77 K) for the N_2 adsorption or to 273 K for CO_2 adsorption.

All chars were characterized by nitrogen adsorption-desorption at the temperature of the boiling point of nitrogen (77 K). The equilibrium time was 30 seconds. The same adsorption result was obtained for longer times such as 45 and 60 seconds. The nitrogen adsorption-desorption isotherms were obtained using a large number of data points to improve resolution. A second fresh sample was analysed for each char in order to check the reproducibility.

The adsorption of carbon dioxide was performed at 273 K with the saturation pressure, P^o, of CO_2 taken as 26142 mmHg. Prior to adsorption, the samples were out gassed at 523 K for 12 hours. For all runs, the maximum CO_2 equilibrium pressures, P, was close to 780 mmHg, which means that, the highest relative pressure, P/P^o, achieved while performing the measurements was 0.030. The time to reach the equilibrium pressure was 15 seconds.

4.3.2 Small-Angle Scattering

4.3.2.1 Small-Angle X- Ray Scattering, (SAXS)

Small angle x-ray scattering measurements were carried out using a Phillips PW-101011 generator with a Kratky camera. It was run at 40 KV and 20 mA ; the radiation (CuKα) was filtered with nickel and collimated by four slits and its incident wavelength λ was 1.54 Å . The detector was positioned to cover an angular range corresponding to values between 0.1° and 3.0° with steps of 0.05° and counting times of 60 seconds per step. The char sample was prepared by packing it in 2 mm inner diameter aluminium holder with Kapton windows and an optical-path length of 2 mm. Three runs were made for each sample and the mean value was calculated. Figure 4.3 shows a schematic diagram of the SAXS apparatus.

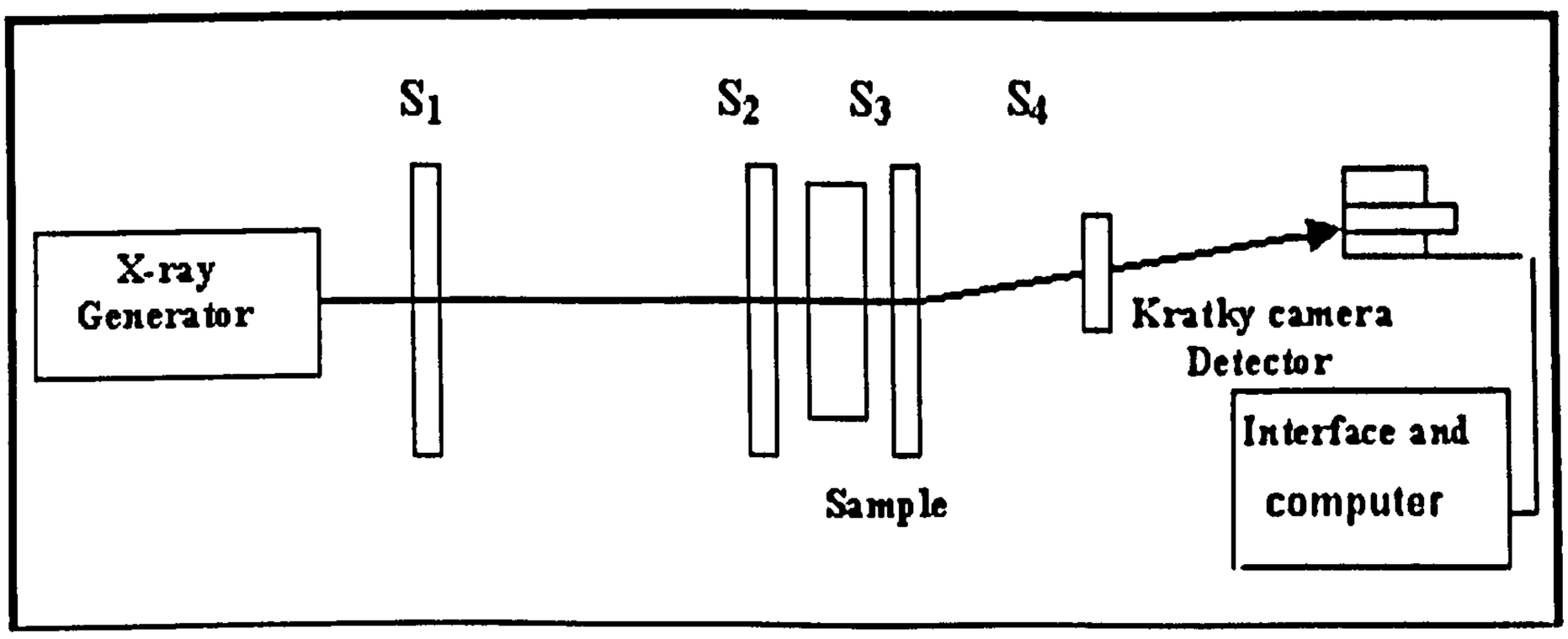

Figure 4.3: Diagram of the SAXS experiment. S_i : Slit collimators

4.3.2.2 Small-Angle Neutron Scattering, (SANS)

The SANS experiments were performed on the 12 m *DR3-Multipurpose Research Reactor at Riso National Laboratory in Denmark*. This a heavy-water moderated and -cooled reactor with a power of 10-12 MW thermal supplied by a fuel of U_3Si_2-Al, enriched at 19.8% [212]. The neutrons are monochromatized by a mechanical velocity selector with a relative wavelength resolution of $\Delta\lambda/\lambda$=0.18. The SANS spectra were collected in a total scattering vector range of 0.002 to 0.55 $Å^{-1}$. The measured spectra

were corrected according to standard procedures for background, as measured with an empty sample holder which was a 2 mm path-length low boron glass *Suprasil* cell, and for instrumental background, as measured with boronated plastic in the sample holder. The data were corrected for detector efficiency and put on absolute scale using a standard water sample [213-214]. SANS was first performed on the dry samples. The sample holder was filled with the powdered carbon or charcoal and the experiment run for 90 min.

Contrast-matching SANS (CM-SANS) was achieved by mixing the sample with high purity deuterated toluene, which has the same neutron scattering cross section as graphite [215]. Deuterated toluene was introduced into the cell and this placed in an ultrasonic bath for three periods of 30 min and left overnight, in order to promote pore filling and removal of trapped air bubbles. SANS was performed on the wet sample.

4.3.3 Positron Annihilation Lifetime Spectroscopy, (PALS)

The measurements of positron annihilation lifetimes were carried out using a conventional spectrometer [216], Figure 4.4. Measurements were obtained using a fast-slow coincident instrument by monitoring the birth signal (1.28 MeV γ-ray) from the decay of ^{22}Na source and the death signal (0.51 MeV γ-ray). These gamma photons are detected by two BaF_2 scintillators, which are joined to fast photomultiplier tubes (PMT); they were positioned at 90° to each other to avoid pile-up. Discrimination between the birth and death photons is achieved in the slow circuit and removes any ambiguity of the nature of photon arriving at the PMT tubes by two simultaneous time and energy discriminators (DFD). The time difference between the two detectors is recorded by a time amplitude converter (TAC), and this information is send via an analogue digital converter (A/DC) to a multi-channel analyser (MCA) where the signal is stored. MCA produces the distribution of life times or spectrum in terms of counts by channel.

The ^{22}Na source of about 13 μCi was prepared by evaporation of a concentrated solution of $^{22}NaCl$ onto a Kapton foil (a polyimide). Then the residue was sealed with a second Kapton foil using an epoxy resin. The source was placed between the sample of about 2.5 g. Life time data were collected in triplicate at room temperature for 6 hours, giving about 10^5 counts accumulated for each measurement which represents a reasonable time to achieve a low signal to noise ratio.

Using this technique the lifetimes of the process of annihilation of the positrons into the carbons were extracted; here each component is determined by a mean lifetime and probability for annihilation. The spectrum consisted of exponentially decaying components then it was fitted using a sum of negative exponential terms by a data-processing program, named PATFIT-88 developed by Riso National Laboratory, Denmark [216-217]. This program deconvolutes the various lifetime components by a least-squares analysis (see Section 2.4). It is necessary to extract the lifetime components to obtain the instrument time-resolution function. In this case, the resolution of the instrument was found by measuring the annihilation of a standard of benzophenone which has a single well defined lifetime occurring at 331 ps. It was represented by three Gaussian functions. Also, the spectrum was corrected by the contribution of the source and background radiation, which was calculated to be 5%. Prior to each analysis the samples were treated in a furnace at 1173 K in a stream of nitrogen for 30 minutes. The lifetimes were fitted into two, three and four components. The three and four lifetime fitting gave large standard deviations. Therefore, the two component results were the most reliable fitting.

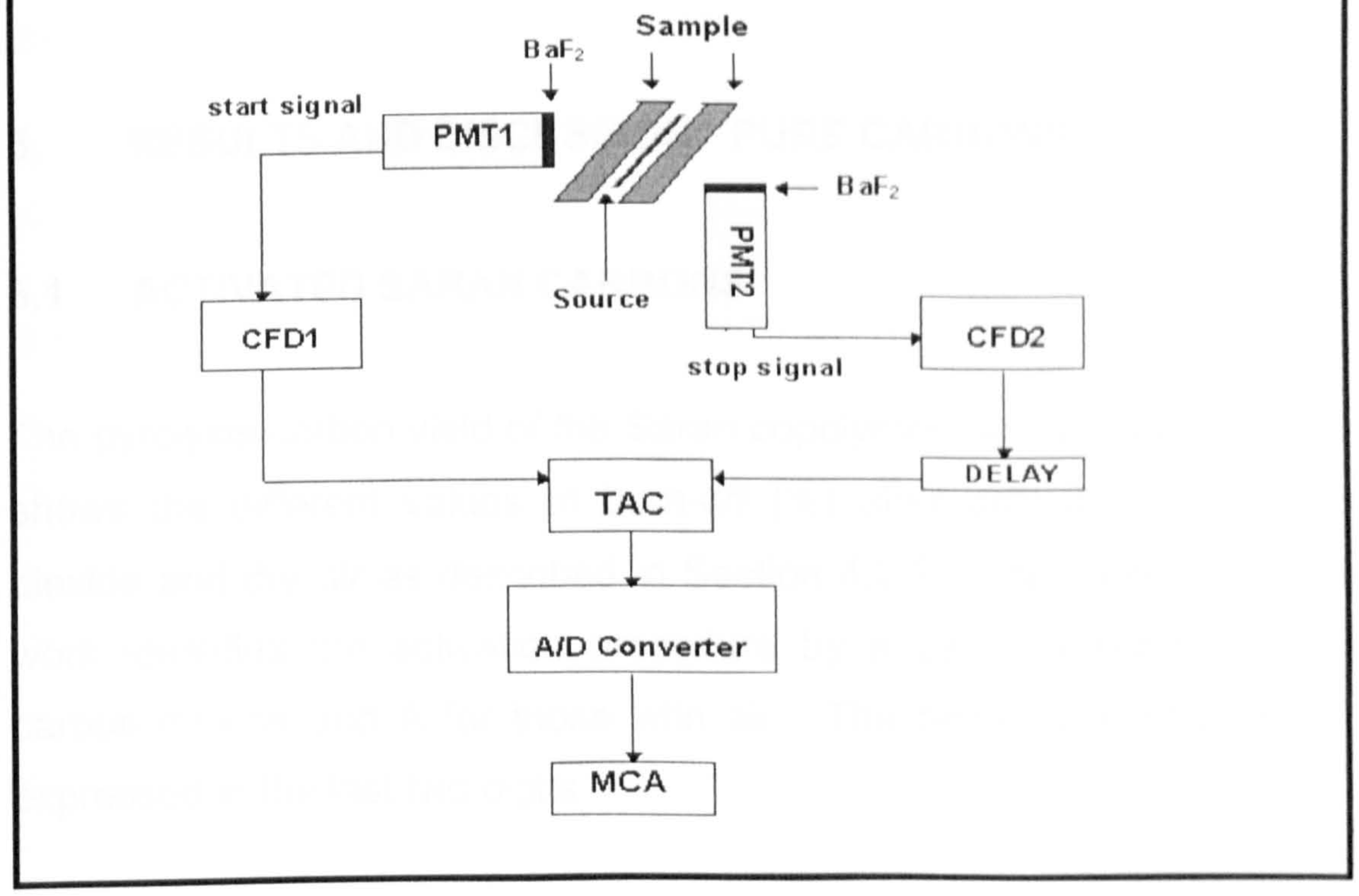

Figure 4.4: Representative block diagram of a positron annihilation lifetime spectrometer.

5. RESULTS AND DISCUSSION: PURE CARBONS

5.1 ACTIVATED SARAN CARBONS

The pyrolysis carbon yield of the Saran copolymer was 28.6%. Table 5.1 shows the different values of burn-off (%) after activation with carbon dioxide and dry air as described in Section 4.2.2. The code used in this work identifies the activation procedure by a capital letter thus, C for carbon dioxide and A for those with air. The percentage of burn-off is expressed in the last two digits.

Table 5.1: Burn-off (%) levels of the carbons from Saran activated in carbon dioxide at 1173 K and dry air at 673 K.

Activation Agent	Carbon code	Burn-off (wt%)*	Time of activation (min)	Elemental analysis (wt%)* C	H	Cl	O
Unactivated	Sar00	0.0	0	87.7	0.9	6.7	4.7
Carbon dioxide	SarC13	12.7	40	95.5	t/n	t/n	4.5
	SarC21	21.4	180	96.0	t/n	t/n	4.0
	SarC36	36.4	390	96.1	t/n	t/n	3.9
Air	SarA08	7.6	30	93.0	0.8	1.1	5.1
	SarA20	20.0	60	94.9	t/n	t/n	5.1

Notes: * dry basis, ** Oxygen by difference, t/n: trace or nil

The carbon content increases with the extent of activation. This kind of carbons has good adsorptive properties and high reactivity in gasification reactions [201-203]. Saran based-carbon is a highly disordered non-graphitic solid with a considerable micropore surface area, more than 700 m^2g^{-1}, an average micropore width of 1.05 nm. This carbon has a low level of impurities and catalytic effects during gasification reactions had been ruled

out [204-206]. Also, Saran char was found to be highly reactive to air with an active surface area (ASA) of 37 m^2g^{-1} [203-206].

5.1.1 Characterisation of Saran Carbons by Gas Adsorption

5.1.1.1 Carbon dioxide activated carbons

Activated Saran carbons were characterised using nitrogen adsorption at 77K. The adsorption and desorption were obtained using a large number of data points to obtain good resolution and long equilibrium times were used to attain equilibrium uptake. Figure 5.1 shows the 77K nitrogen adsorption-desorption isotherms of Saran carbons activated in CO_2. They are of the type I according to the IUPAC classification [99,134,218]. Their shape is typical for microporous materials having a high surface area and shows a large increase of gas adsorption at low relative pressure which is associated with micropore filling [219].

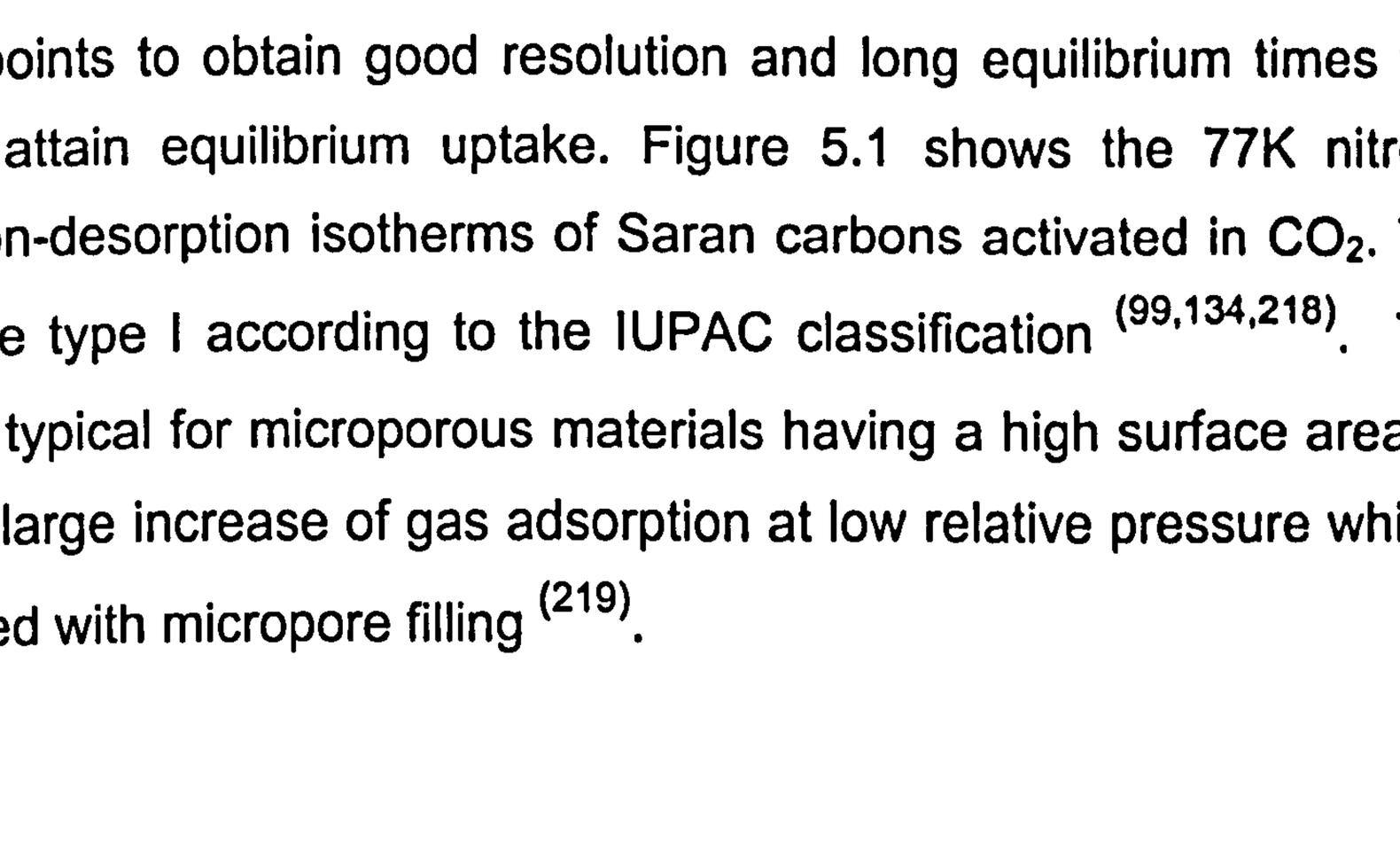

Figure 5.1: 77K nitrogen adsorption-desorption isotherms for Saran carbons activated to different values of burn-off in carbon dioxide.

The shape of the knee is very sharp for the samples with less than 21% of burn-off, then the equilibrium plateau is reached at very low value of relative pressure, *P/Po* (i.e. 0.035). For the more highly activated carbon (36% of burn-off) the knee is broader and the equilibrium pressure plateau is reached at higher value of *P/Po*, (i.e. 0.049). However, this sample is still classified as a microporous material. The plateau for all the samples is virtually horizontal up to high *P/Po*, it is mean that the isotherm is reversible and the limiting uptake can be taken as a direct measure of the micropore capacity.

Figure 5.2 shows the CO_2 at 273 K adsorption isotherm of carbon dioxide activated Saran carbons. They are characteristic of microporous materials; the pressure equilibrium plateau is reached at 0.03 P/Po, while the other samples showed a light tendency to increase at this value. Basically, the CO_2 adsorbed behaviour for all carbon dioxide activated Saran carbons is similar.

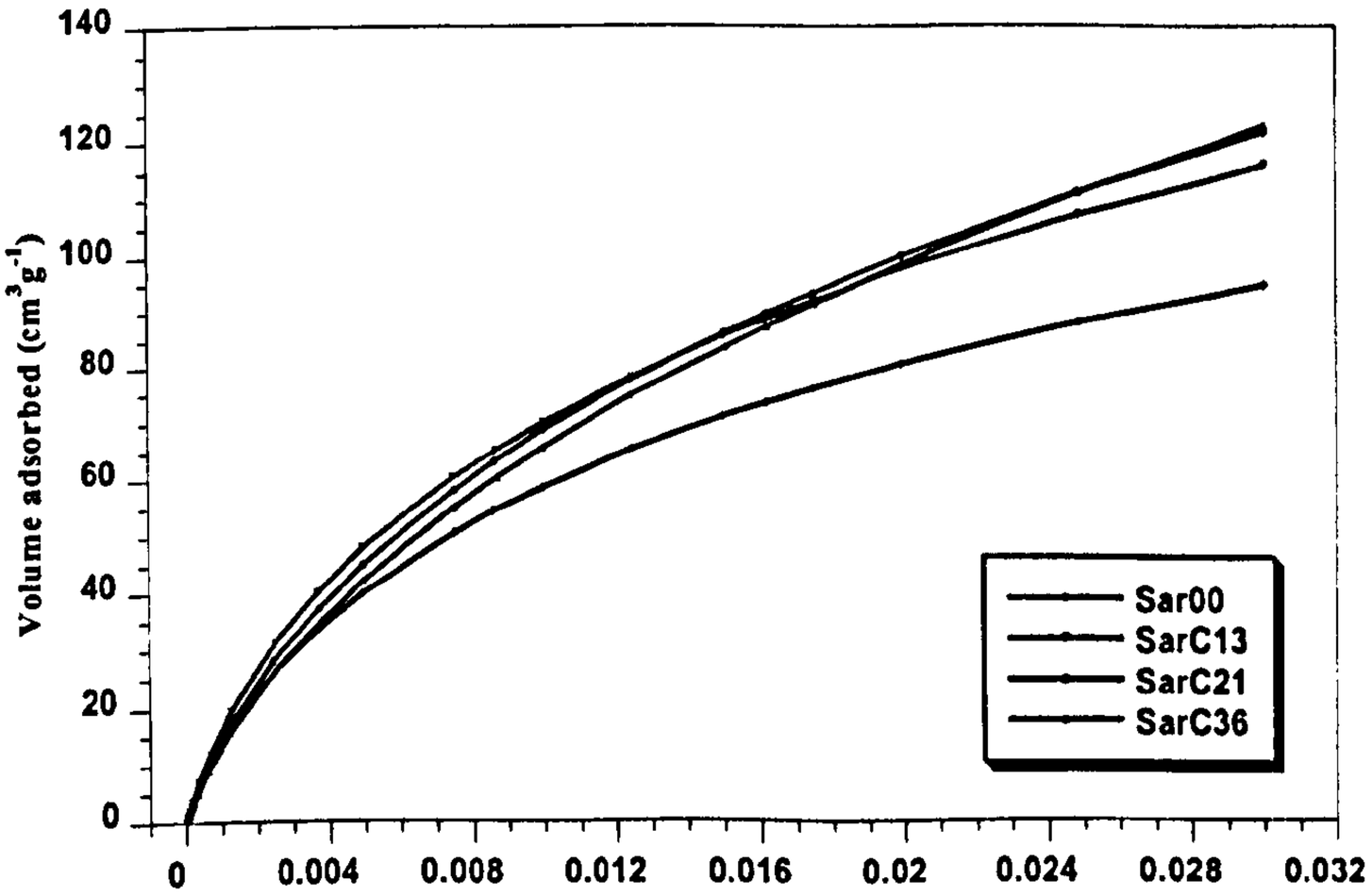

Figure 5.2: 273 K carbon dioxide adsorption isotherms for Saran carbons activated to different levels of burn-off in carbon dioxide.

Surface areas were calculated using the Brunauer-Emmett-Teller (BET) equation applied to N_2 adsorption data at 77 K [113]. Micropore surface

areas were determined from CO_2 adsorption data at 273 K using the Dubinin-Raduskeivich (DR) theory [104]. Table 5.2, shows the values of surface area values and pore volumes from the N_2 and CO_2 adsorption data.

Table 5.2: Characterisation of Saran carbons activated with carbon dioxide at 1173 K, by physical adsorption using N_2 at 77 K and CO_2 at 273 K

Carbon	V_{N2} (cm^3g^{-1})	N_2-BET Surface Area (m^2g^{-1})	V_{CO2} (cm^3g^{-1})	$E_{0\,(CO2)}$ ($kJmole^{-1}$)	L_{CO2} (nm)	CO_2-DR Micro Surface Area (m^2g^{-1})	$V_{N2} - V_{CO2}$ (cm^3g^{-1})
Sar00	0.32	681	0.33	14.1	1.70	823	-0.01
SarC13	0.42	908	0.39	14.2	1.69	969	0.03
SarC21	0.50	1089	0.41	13.8	1.74	1011	0.09
SarC36	0.69	1464	0.41	13.5	1.78	1029	0.28

A comparison of the pore volume calculated from V_{N2} and V_{CO2} adsorption experiments is shown in Figure 5.3. V_{CO2} is higher than V_{N2}, only for the 0% activated sample. The other samples show an increasing difference which could be produced by widening process in the micropores during activation; this effect is associated with the activated entry of adsorbate molecules through very narrow pore entrances or constrictions. A sub-classification of the micropore region has been proposed with submicroporosity being defined as pores with size less than 0.7 nm and supermicroporosity to pores with size between 0.7 and 2 nm [219]. The amount of supermicroporosity is usually calculated from $V_{N2} - V_{CO2}$.

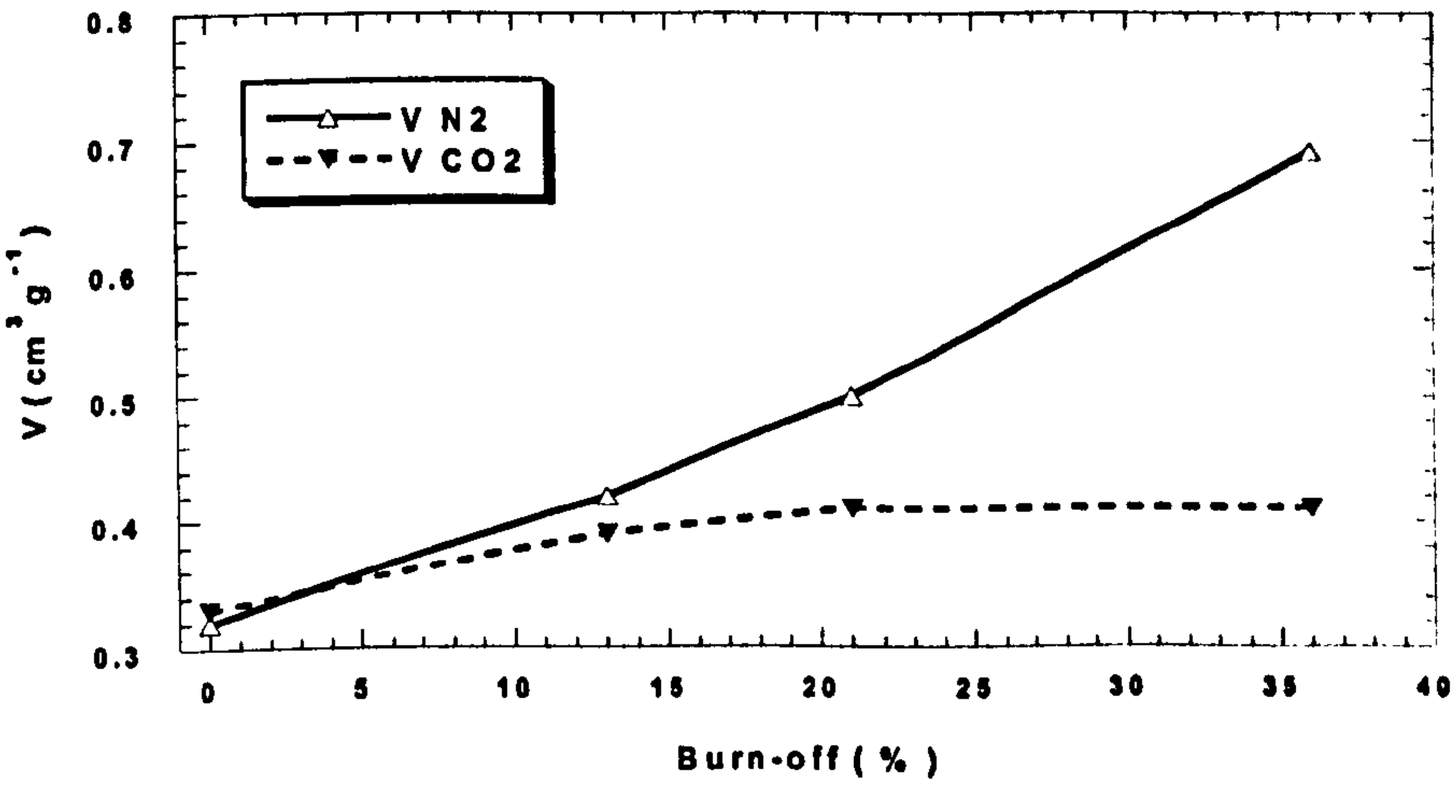

Figure 5.3 : Pore volume calculated from N_2 and CO_2 adsorption for Saran carbons activated to different values of burn-off in carbon dioxide.

5.1.1.2 Air activated carbons

The two Saran carbons prepared in air show similar adsorption behaviour to the carbon dioxide activated carbons. Figure 5.4 displays the N_2 adsorption-desorption isotherms for these carbons in comparison to the unactivated carbon. All of them are type I isotherms without low or high-pressure hysterisis[99]. The pressure equilibrium plateau is reached more or less at the same value of relative pressure and the sharp knee formed at low value of P/Po confirms that they are associated with highly microporous systems.

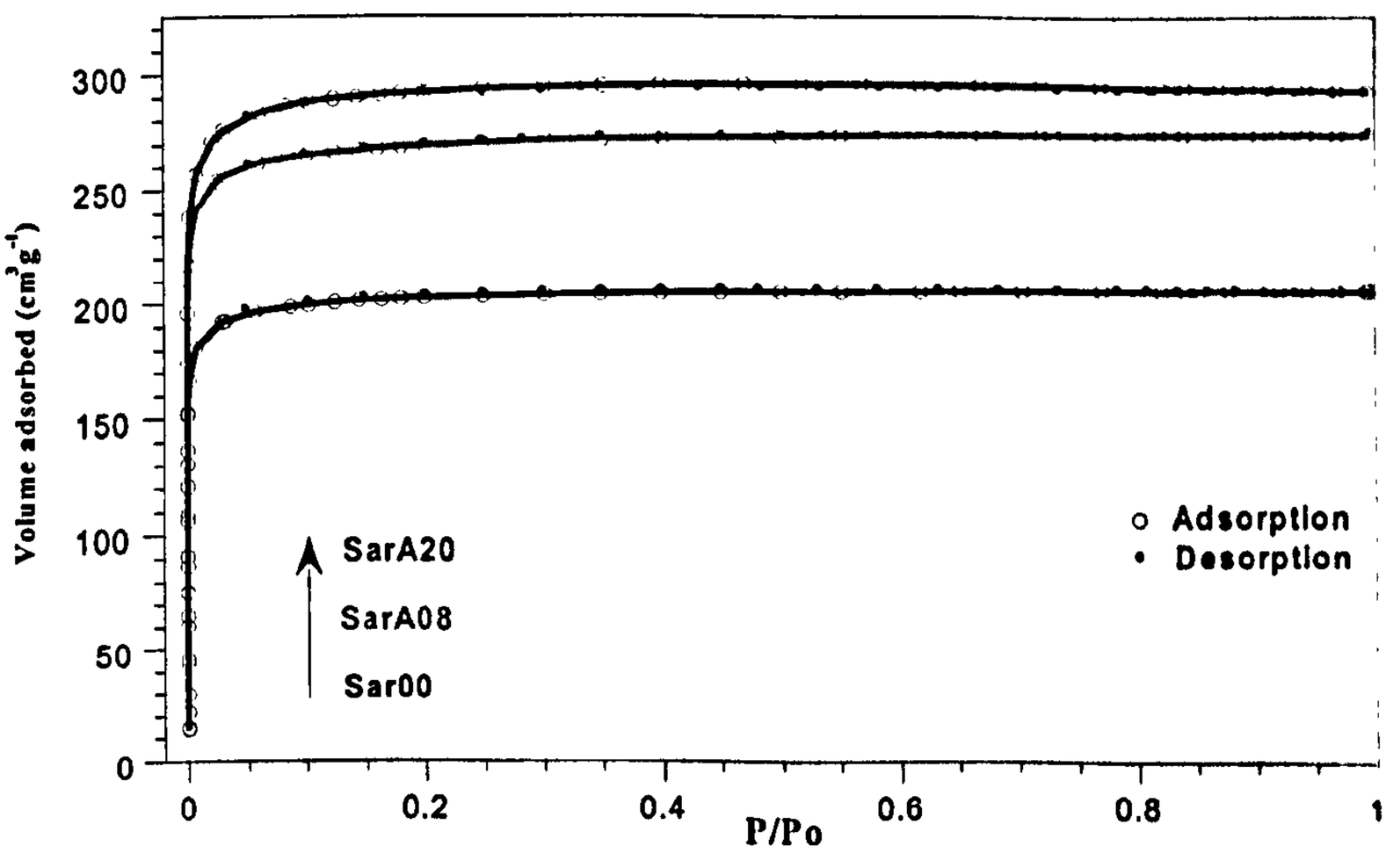

Figure 5.4: 77K nitrogen adsorption-desorption isotherms for Saran carbons activated to different values of burn-off in air.

The CO_2 adsorption results are shown in the Figure 5.5. This graph is in agreement with the information inferred from N_2 adsorption, as it displays high adsorption at low values of relative pressure.

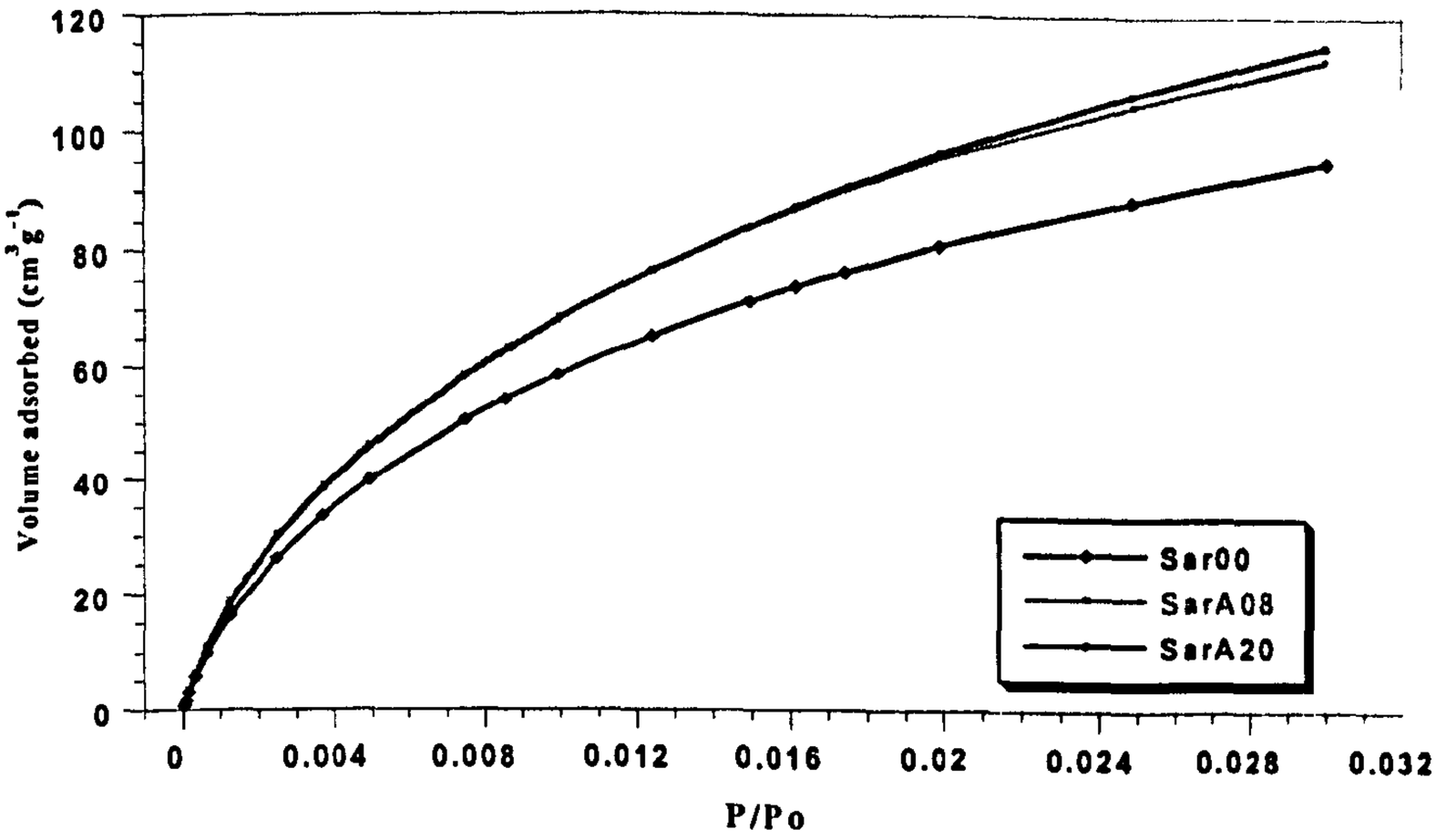

Figure 5.5: 273 K carbon dioxide adsorption isotherms for Saran carbons activated to different values of burn-off in air.

Table 5.3 gives the BET surface areas and pore volumes for the air activated carbons. Figure 5.6 shows that the air activation process has a similar effect on pore development to carbon dioxide, i.e. the pore volumes calculated from N_2 adsorption are higher than the corresponding from CO_2 adsorption values.

Table 5.3: Characterisation of air activated Saran carbons by physical adsorption using N_2 at 77 K and CO_2 at 273 K

Carbon	V_{N2} (cm^3g^{-1})	N_2-BET Surface Area (m^2g^{-1})	V_{CO2} (cm^3g^{-1})	E_{0CO2} ($kJmole^{-1}$)	L_{CO2} (nm)	CO_2-DR Micro Surface Area (m^2g^{-1})	$V_{N2} - V_{CO2}$ (cm^3g^{-1})
Sar00	0.32	681	0.33	14.1	1.70	823	-0.01
SarA08	0.42	901	0.39	14.0	1.71	977	0.03
SarA20	0.45	980	0.40	13.8	1.73	996	0.05

As discussed in Section 2.2.5, gas adsorption leaves many questions unanswered concerning pore development and cannot provide certain important information. For example, is the increase in surface area due to

the creation of new pores, pore widening or the opening of closed porosity? Also, neither nitrogen nor carbon dioxide adsorption can give information about micropore sizes. For this reason, the carbons were also characterised by small angle scattering.

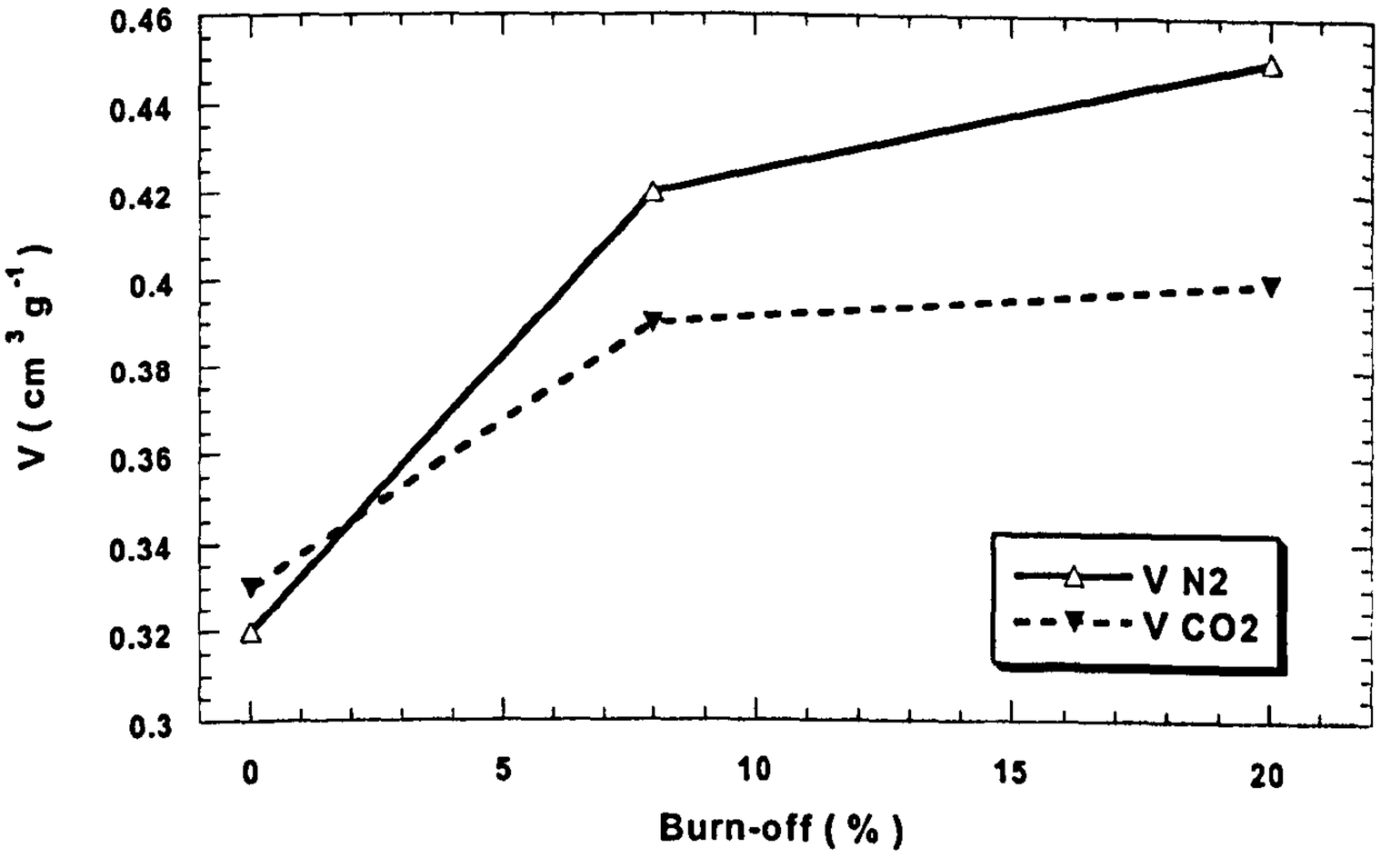

Figure 5.6: Pore volume calculated from N_2 and CO_2 adsorption for Saran carbons activated to different values of burn-off in carbon dioxide

5.1.2 Characterisation of Saran Carbons by SAS

5.1.2.1 Small Angle X-Ray Scattering (SAXS)

Small angle x-ray scattering of the carbon dioxide activated Saran carbons are shown on a *log(I(q))* versus *log(q)* basis in Figure 5.7. The relatively intense scattering at high *q* values indicates scattering from microporous materials [157,158]. It can also be seen that the scattering intensity increases with increasing activation, which is consistent with pore development.

A quantitative analysis of the SAXS curves using the Guinier approach (Equation 2.51) is shown in Figure 5.8, which is a plot of *ln(I(q))* versus q^2.

The radius of gyration of scattering object, *Rg*, is calculated from the slope of the linear region at high q range of this graph. For all Saran derived carbons the plots had a relatively wide linear region ($1.0 < q\ (nm^{-1}) > 4.3$) which indicates a narrow distribution of pore sizes.

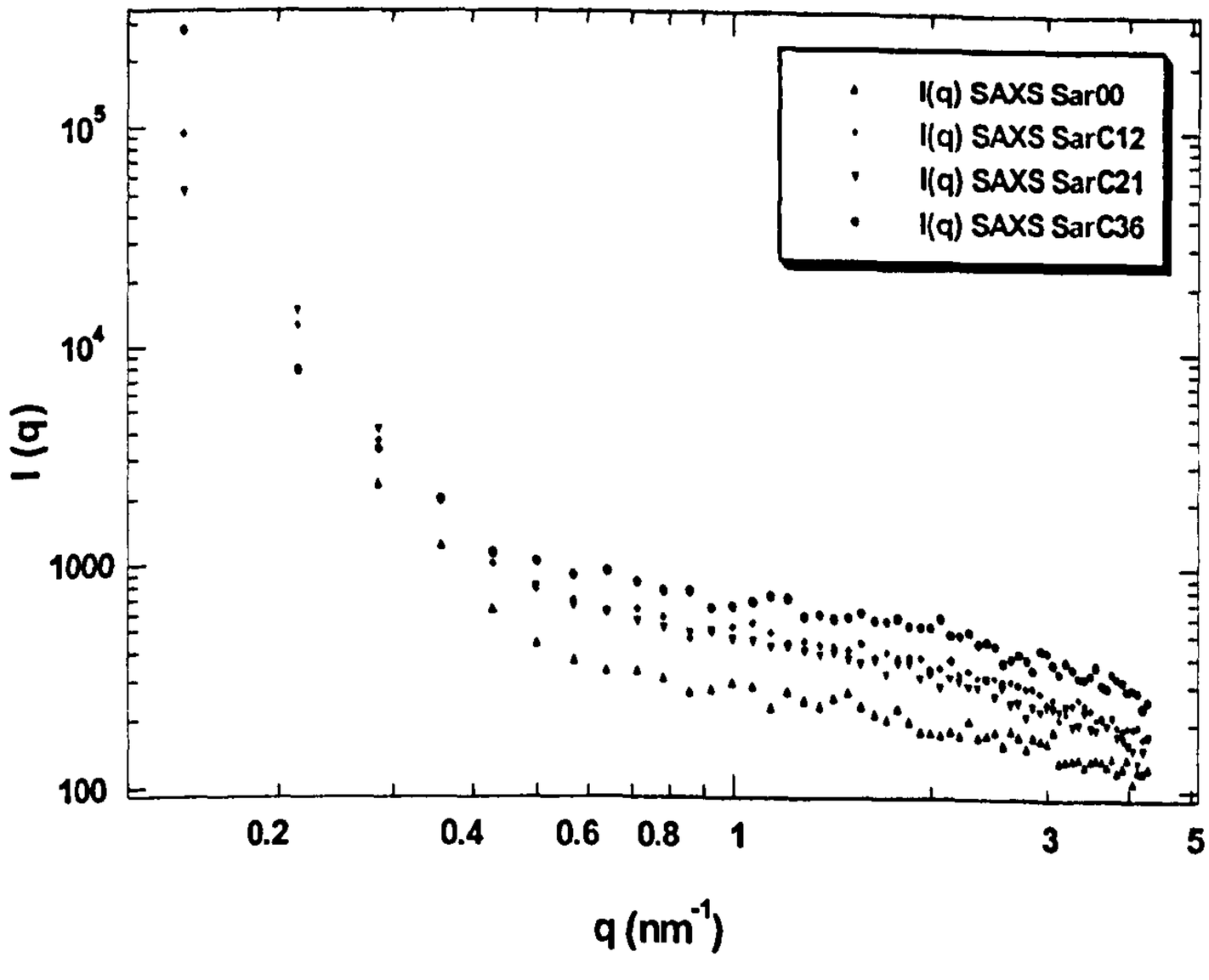

Figure 5.7: Small angle x-ray scattering analysis for Saran carbons activated to different values of burn-off in carbon dioxide.

The values of *Rg* increase from a value of 0.37 nm for the unactivated carbon to a value of 0.44 nm for the 13% burn-off sample. After this the *Rg* obtained remain almost unchanged with the activation process until 36% of burn-off. This indicates that this activation proceeds generating and/or modifying the previous microporosity without a significant widening process.

Table 5.4: Characterisation by SAXS of Saran carbons activated with carbon dioxide, using Porod law and Guinier theories

Carbon	*Rg* (nm)	*d* (nm)	Q (arb units)
Sar00	0.37	0.94	4288
SarC13	0.44	1.13	6877
SarC21	0.43	1.11	6073
SarC36	0.41	1.06	10112

As was discussed in Section 2.3.2, Porod Invariants, Q, can be strictly calculated only when a q^{-4} dependence is found. The carbon dioxide activated carbons display significant deviation from q^{-4} behaviour but nevertheless, Q values provide a useful comparison between samples and also it senses about how the amount of voidage is changing. Q and *Rg* values are given in Table 5.4. If a spherical geometry is assumed the pore size diameter,*d*, is calculated from *Rg* according to Equation 3.52. [215]

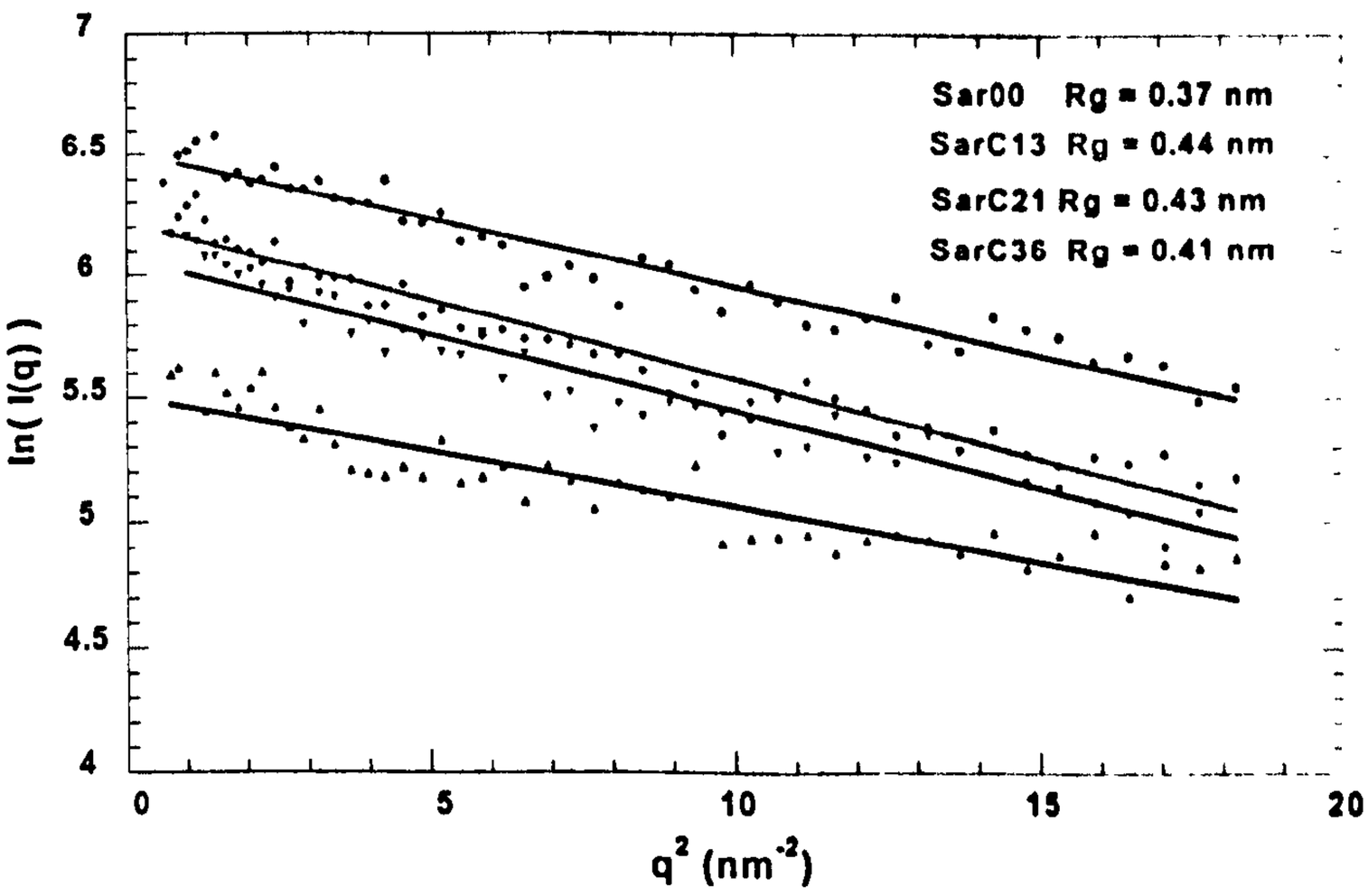

Figure 5.8: Guinier plot analysis from Small angle x-ray scattering analysis of Saran carbons activated to different values of burn-off with carbon dioxide.

In general, the Q values increase with activation. The slight decrease between 13% and 21% of burn-off can be attributed to experimental error.

5.1.2.2 Small Angle Neutron Scattering (SANS)

The complete set of carbon dioxide activated carbons was studied using SANS in the range $0.1 \leq q\ (nm^{-1}) \leq 5.6$. Figure 5.9 shows the small angle neutron scattering patterns for the carbon dioxide activated Saran carbons in comparison with the unactivated carbon. The SANS intensity shows a

maximum to 21% burn-off. The decrease in scattering to 36% could be due to pore wall gasification removing microporosity.

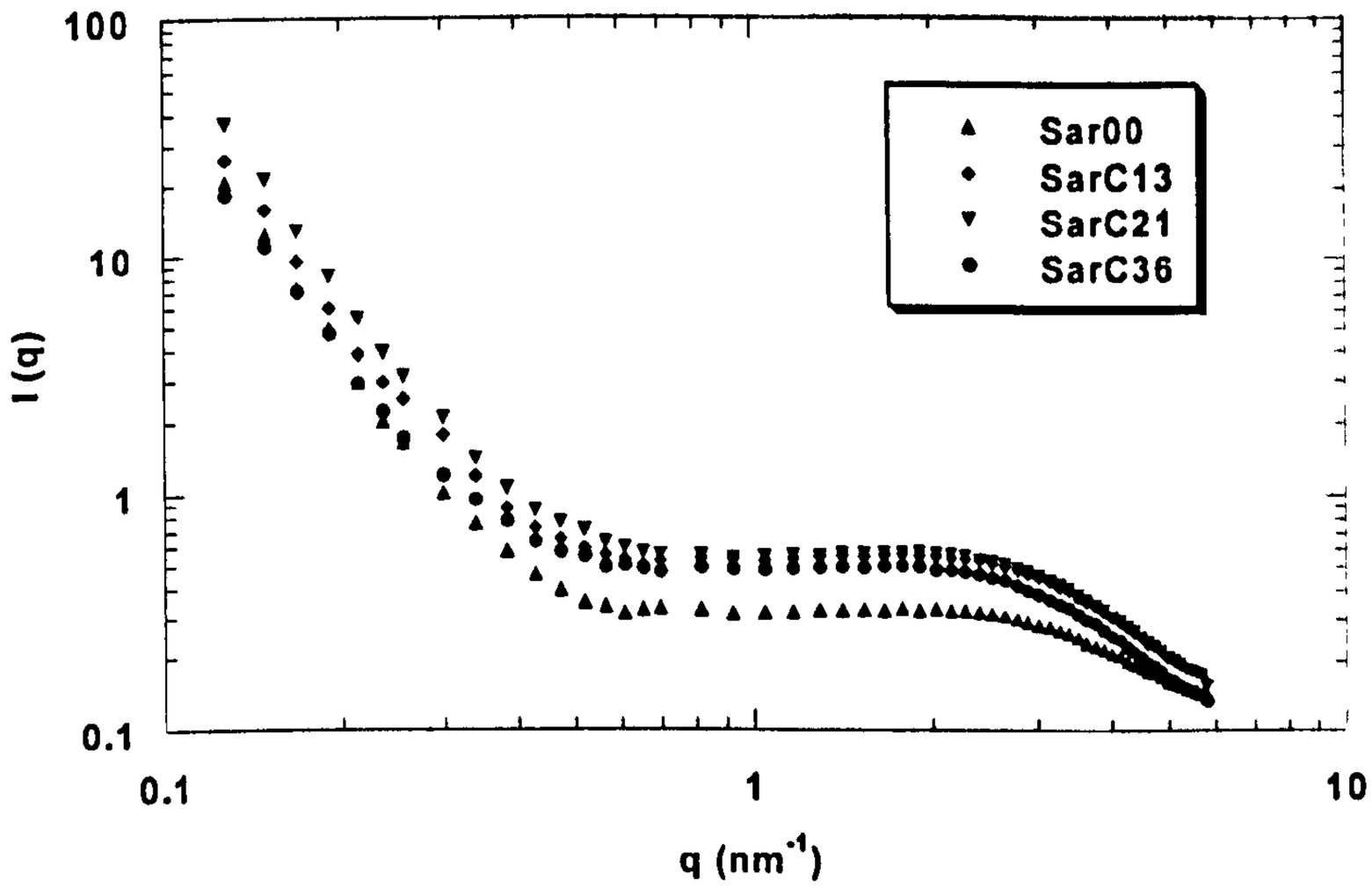

Figure 5.9 : Small angle neutron scattering analysis for Saran carbons activated to varying extents in burn-off with carbon dioxide

Contrast-matching SANS (CM-SANS) data was measured for the unactivated Saran carbon, according to the procedure described in Section 4.3.2.2. It is known that in SANS experiments on dry samples, scattering is from both closed or inaccessible and open or accessible porosity. In CM-SANS experiments scattering contribution from open porosity is eliminated and any residual scattering is attributed to closed porosity [173]. Then, the difference in the scattering intensity data between dry and cm-wet samples is indicative of the open porosity.

The comparison between dry and cm-wet scattering data for the unactivated carbon is presented in Figure 5.10. In this case, the CM-SANS scattering intensity was negligible. Therefore, this graph shows that the total scattering intensity may be assumed be only from open porosity.

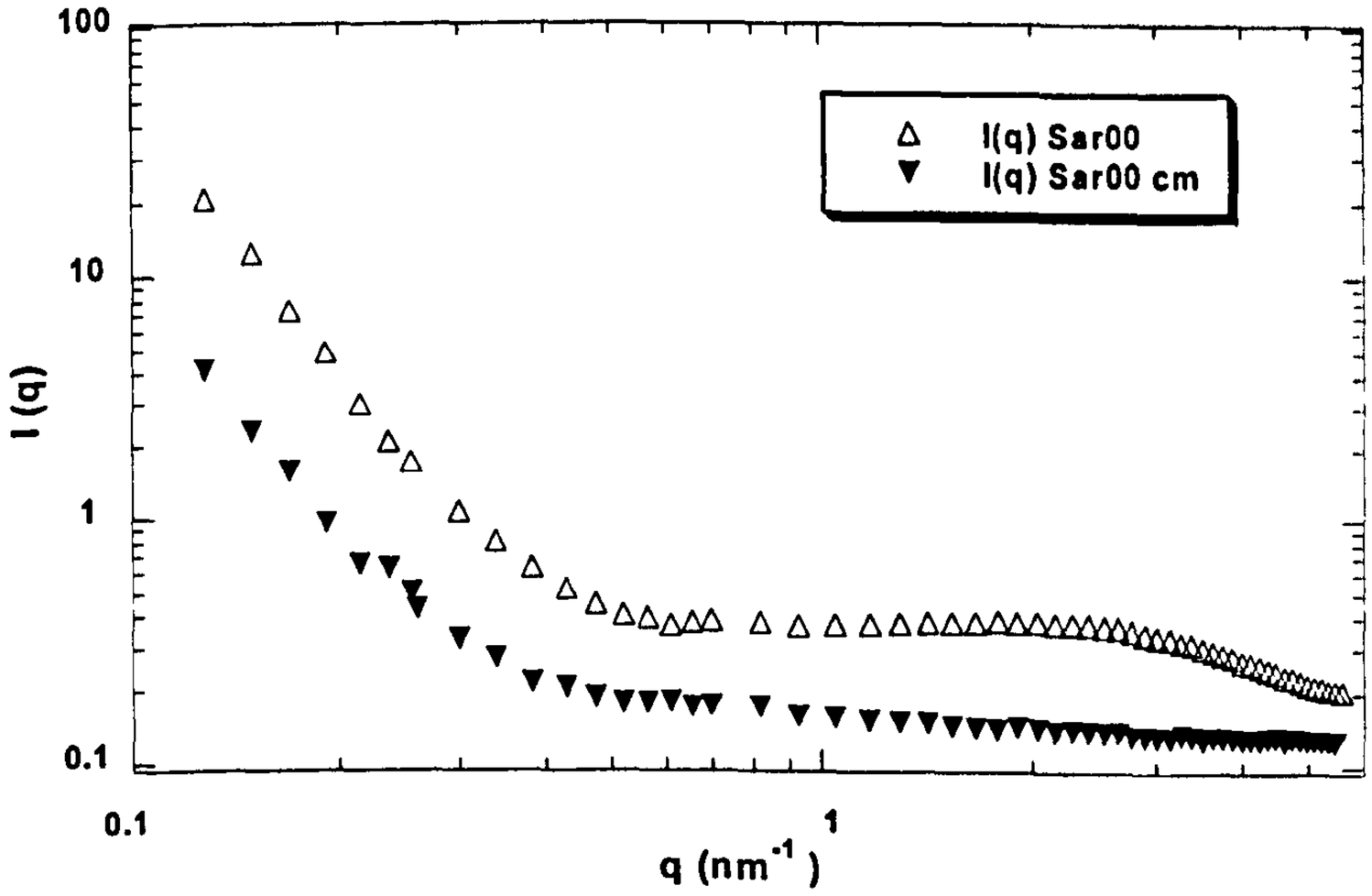

Figure 5.10: CM-SANS experiment from unactivated Saran carbon. The white triangle signs are dry data points, and dark triangle are cm-wet data points after mixing with deuterated toluene.

It is seem from Figure 5.9 that SANS scattering intensity decayed in two different well defined q regions. This kind of scattering intensity data behaviour has been seen for porous coal chars and polymer carbons [171,173]. In these works the scattering intensity data were successful fitted by a fractal model applied to the linear decrease in low *q* region and a polydisperse distributed sphere model applied to the high *q* region.

The fractal dimension, *D*, was calculated from linear region of the log-log plot. The *D* values go through a maximum for the 13% activated sample. A fractal dimension of 3 represents a highly convoluted surface [156]. The initial stages of gasification appear to increase surface roughness and subsequent gasification produces increasingly smooth surfaces.

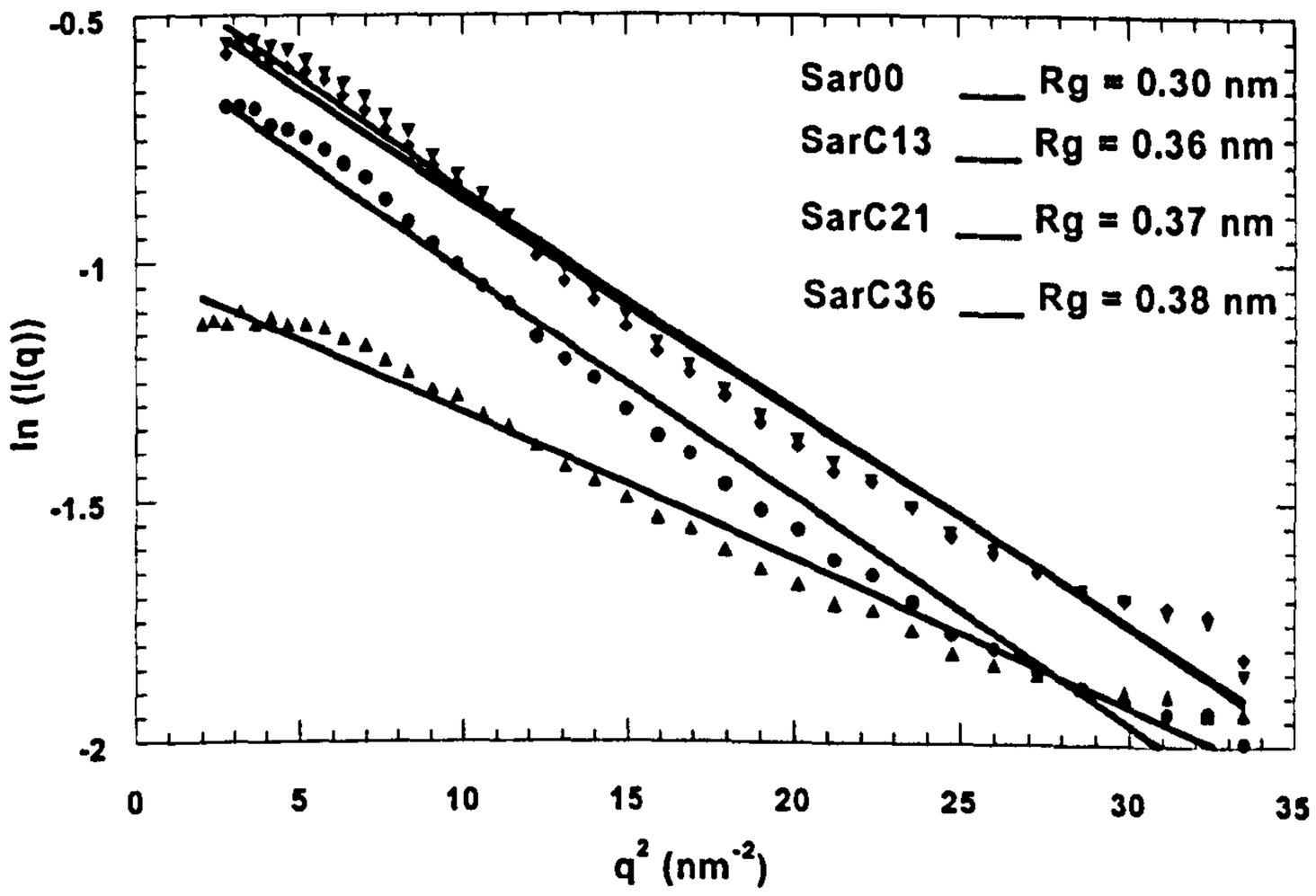

Figure 5.11 : Guinier plot analysis from small angle neutron scattering analysis of Saran carbons activated to different values of burn-off with carbon dioxide.

Modelling of scattering of the SANS data has been applied to provide a qualification of the pore size distribution and mean pore size. Figure 5.11 shows a Guinier plot of SANS data obtained for the carbon dioxide activated Saran carbons. It can be seen that the curves show significant deviations from the least squares fit, suggesting poor agreement with the Guinier law. At lower *q* values the graph curves upwards signifying scattering from a polydisperse system. Despite the poor fits, radii of gyration were calculated and Table 5.5 gives the Rg values for the CO_2 activated Saran carbons. *Rg* is 0.30 nm for the unactivated carbon; the other carbons have a value ranging from 0.36 to 0.38 nm. Over the region of best linearity it can be seen that the values of $q.R_g$ are greater than 1 which indicates that the Guinier law cannot be strictly applied.

To overcome the limitations of the Guinier approach, polydisperse and monodisperse scattering models were applied. A Shultz polydisperse distribution of spheres model does not fit the data [160] but a sphere

monodisperse distribution applied to model the data was successful [141,160].

In this case the form factor was a sphere. As was shown in Equation 2.47 this factor depends only on the radius, *R*. Using this model the mean micropore radius, R_m, obtained for Saran active carbons varying from 0.37 to 0.45 nm in the *q* range. Good agreement was found between the trend showed by *Rg* and the mean radius of the monodisperse spheres. The unactivated carbon had the lower R_m value, 0.37 nm. At 13% of burn-off R_m reached 0.43 nm and then this value increased slightly until 0.45 nm for the higher burn-off, i.e. 36%. Figure 5.12 shows the fits using a combined model obeying fractal and monodisperse sphere.

Table 5.5: Characterisation of Saran carbons activated with carbon dioxide by SANS, using Guinier and Porod law approaches, and a combined fractal and monodisperse sphere models

Carbon	*Rg* (nm)	*d* (nm)	Q (arb. Units)	D	R_m (nm)
Sar00	0.30	0.78	13.2	2.70	0.37
SarC13	0.36	0.94	18.6	3.00	0.43
SarC21	0.37	0.95	18.8	2.65	0.44
SarC36	0.38	0.97	15.7	2.56	0.45

5.1.3 Characterisation of Saran Active Carbons by Positron Annihilation Spectroscopy (PALS)

The Saran derived carbons activated with carbon dioxide and steam were analysed by positron annihilation spectroscopy. The experimental positron annihilation spectra were fitted using the Positronfit deconvoluting program [216,217] to obtain the lifetimes, τ_i, and their intensities, I_i (Section 2.4). The fit was attempted for two, three and four lifetimes (100, 400, 5000 and 30000 ps), for all of Saran derived carbons the best statistical analysis was obtained using two lifetime components. The instrument time resolution (FWHM) was 240-250 ps.

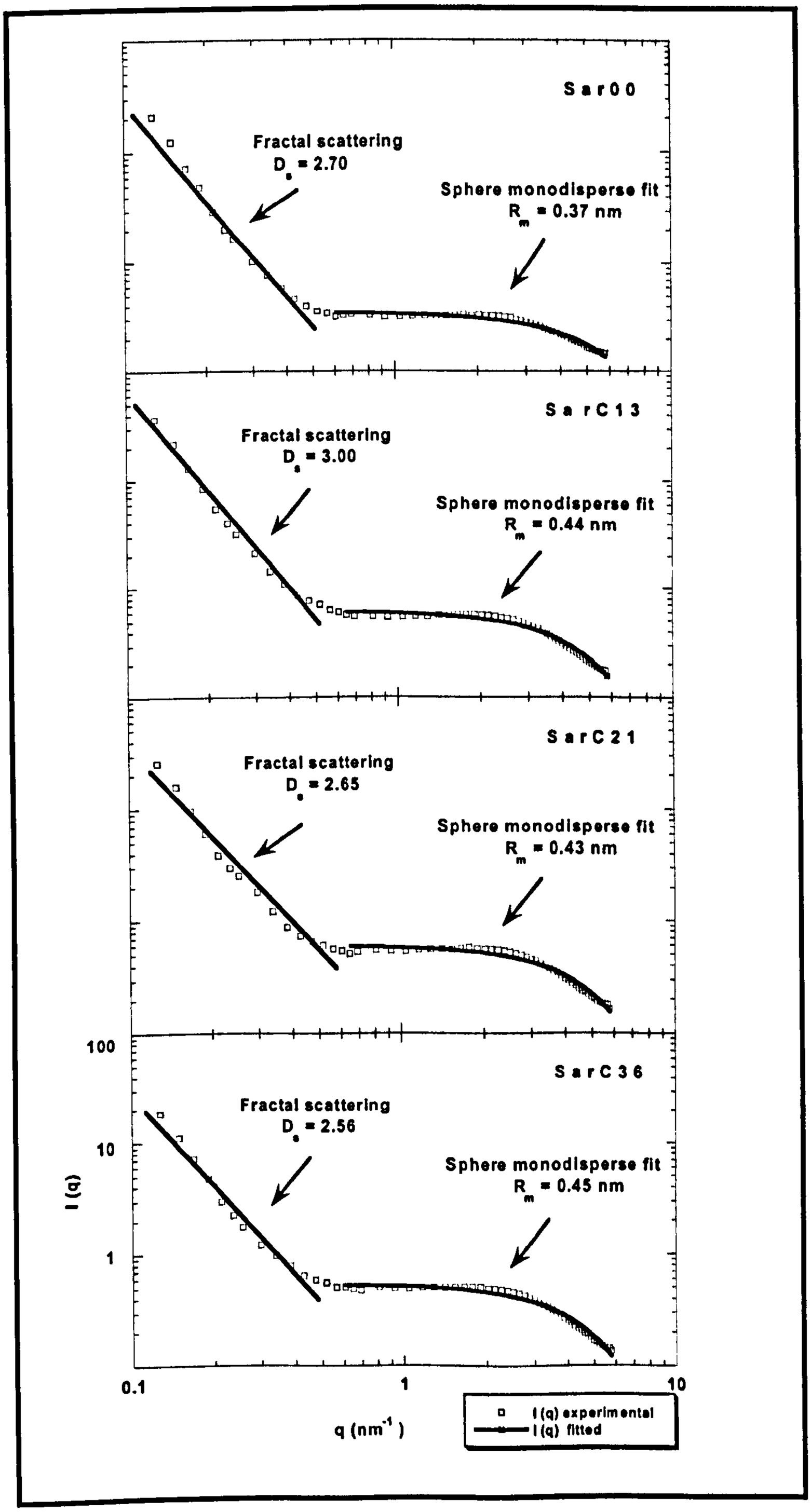

Figure 5.12 : Modelling of SANS from Saran carbons gasified with carbon dioxide at 1173 K in terms of fractal and monodisperse sphere model. The square signs are the experimental data points, and the continuous line is the model fitted.

The spectra were dominated by a short lived component ranging from 382 to 401 ps with ± 1 ps of variance. A minor long lived component ranging from 2235 to 3707 ps with a high variance of ± 1000 ps was also detected. The intensity for the shorter lifetime component was near to 99 ± 0.1%. (see Table 5.6) The longer lifetime was probably due to a minor surface annihilation effect and was neglected. Hereafter, the analysis is based on the existence of only one lifetime component (τ_1 ~ 400 ps).

Table 5.6: Lifetimes and intensities derived by fitting the spectrum from PALS for carbon dioxide and air activated Saran carbons

Carbon	τ_1 (ps)	I_1 (%)	τ_2 (ps)	I_2 (%)
Sar00	382	99.8	2365	0.2
SarC13	382	99.9	3707	0.1
SarC21	388	99.9	2648	0.1
SarC36	401	99.7	2235	0.3
SarA08	383	99.9	2950	0.1
SarA20	382	99.9	1635	0.1

In Section 3.4.4 it was shown that a lifetime near to 400 ps in carbons materials had been assigned to annihilation of positrons by interaction with the electron density at the surface and surfaces around pores or voids for porous solids [193-195,197,199]. The fact that no bulk annihilation was detected is because of the highly disorder nature of the Saran derived carbons [203-206]. The lifetime of free positrons in the perfect graphite lattice is estimated to be 215 ± 10 ps [193,195].

Here, no o-positron atom annihilation lifetime was found after deconvolution of the spectra of Saran derived carbons. This lifetime component had been reported from well defined mesoporous materials, like zeolites (NaHY and NaHM type), silica gel or vycor glass [220-222]. Two o-Ps components with annihilation lifetimes of 4 and 30 ns were reported for porous XAD styrene-resins [186]. XAD-2 and XAD-4 resins had high

BET-surface areas, 300 and 800 m^2g^{-1}, and an average pore diameter of 5 and 9 nm, respectively. For these mesoporous adsorbent resins, a third predominant short lived component was also found about 400 ps (76 and 69 % for XAD-2 and XAD-4 respectively).

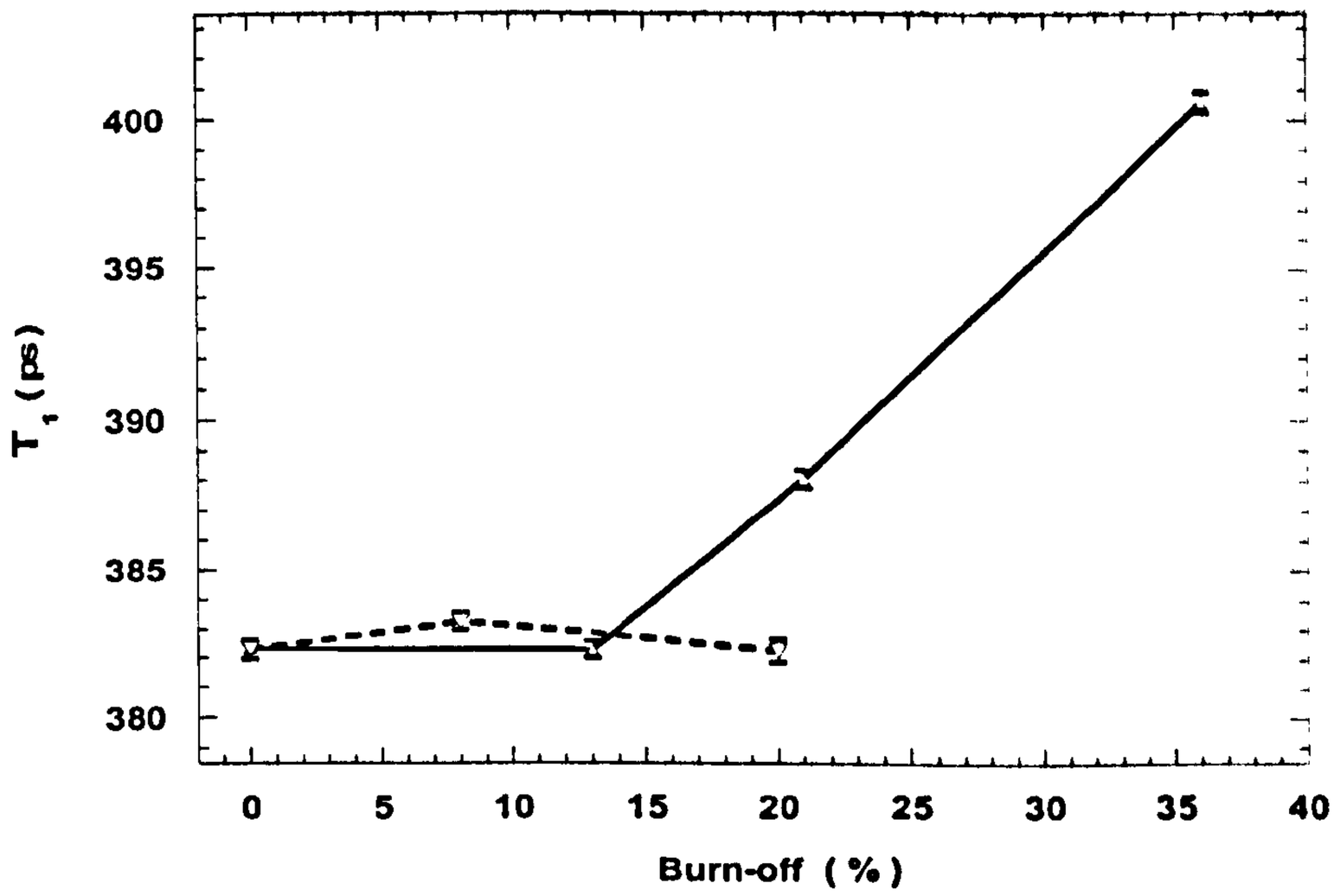

Figure 5.13: Positron annihilation lifetime for Saran derived carbons. Carbon dioxide activation at 1173 K is represented by continuous line and filled triangles signs. Air activation at 673 K is represented by dashed line and inverted triangles signs. Error bars are included.

Figure 5.13 compares the variation of the annihilation lifetime found for Saran derived carbons as a function of burn-off in carbon dioxide and air. It can be seen that the lifetime remains constant in the initial stages of burn-off (<13%) and then increases steeply until the maximum burn-off in carbon dioxide activation. The graph also shows that the positron lifetime does not vary significantly for air activated Saran carbon on the range of burn-off studied.

5.1.4 Correlation of the Characterisation by Positron Annihilation Spectroscopy (PALS) with Gas Adsorption and Small Angle Scattering

Figure 5.14 compares *Rg* values calculated from intensity scattering data of SAXS and SANS analysis against the inverse value of the energy of the process of the adsorption of CO_2 at 273 K into the microporosity of Saran

derived carbons. The inverse adsorption energy value and *Rg* can be directly related to mean pore size. It is seem that while the estimate of the pore size obtained from CO_2 adsorption between unactivated carbon and the sample activated at 13% of burn-off remains constant, Rg from both SAXS and SANS increases. *Rg* values calculated for SarC21 and SarC36 are similar but the CO_2 adsorption differs and shows a increase of the pore size (see Tables 5.2, 5.4 and 5.5). If the mean diameter calculated assuming a spherical geometry from SAS, *d*, is compared with the pore size deduced from CO_2 adsorption, L_{CO2}, it is noted that L_{CO2} values are higher than d values. That means that CO_2 adsorption is taken account for both large porosity and the filling mechanism is not followed [223-226]. Some researchers have expressed limitations related to the quadrupole moment of the CO_2 molecule which influences the mechanism of adsorption on porous carbon surfaces [127,133]. Therefore, it is recommendable to be cautions about information obtained from CO_2 adsorption to the microporosity system.

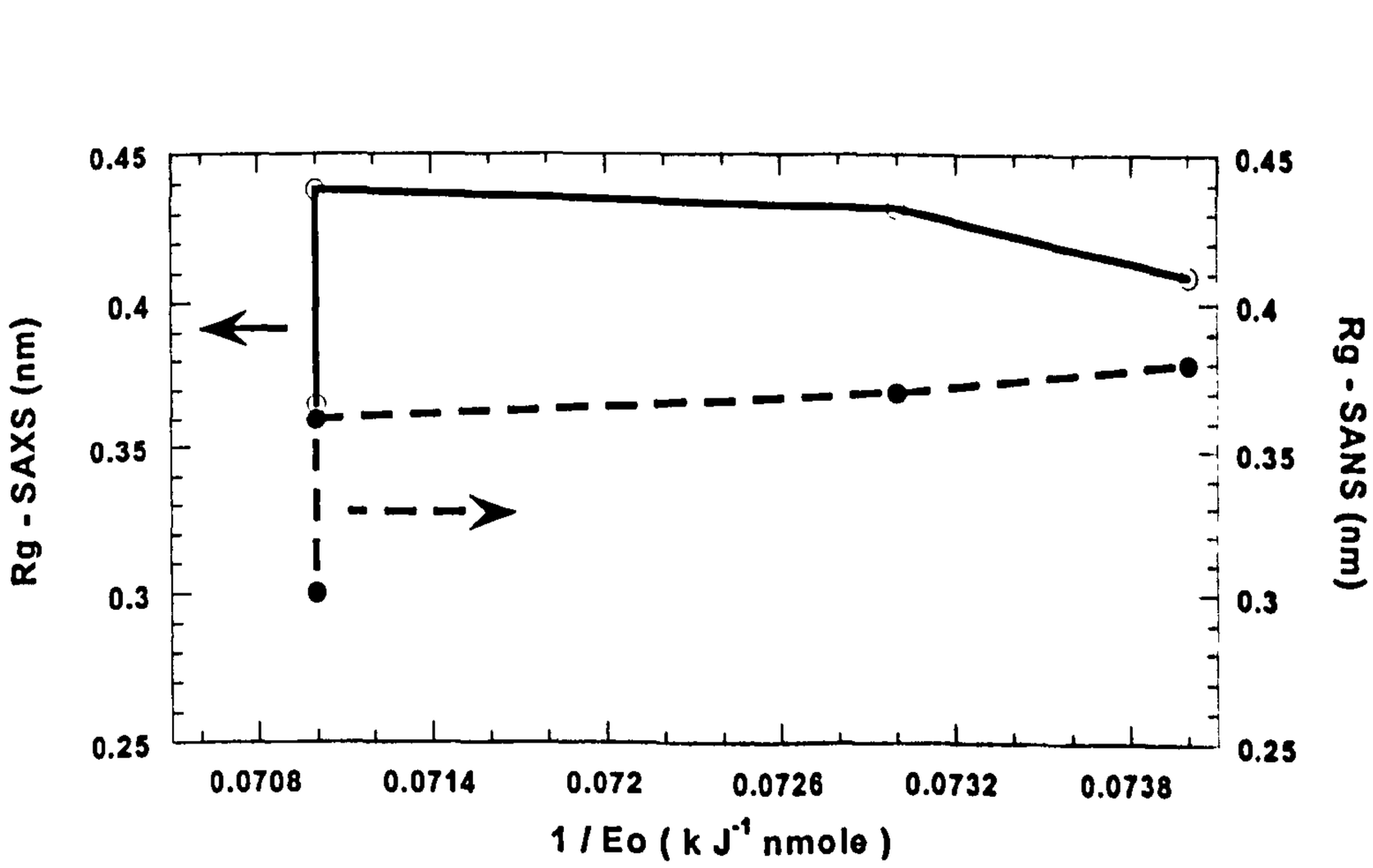

Figure 5.14: Correlation between pore size measured from CO_2 adsorption at 273 K which is inferred from 1/Eo, and *Rg* calculated from SAXS and SANS analysis.

For all carbon dioxide Saran carbons studied the mean pore size deduced from SANS, d_{SANS} was lower than the corresponding value obtained from

SAXS, d_{SAXS}, and the latter was lower than the value obtained from CO_2 adsorption, L_{CO2}. However d_{SAXS} and d_{SANS} were very close. That is, the mean pore value from SAS varies between 0.7 to 1.1 nm while, from CO_2 adsorption varies between 1.7 to 1.8 nm.

Figure 5.15 relates surface area (from N_2-BET) and micro surface area (from CO_2-DR) with Porod Invariant from both SAXS and SANS techniques. The trend noted in Figure 5.14 shows the increase of the Q_{SAXS} according to the SA-N_2 and MSA-CO_2, while Q_{SANS} shows an increase from Sar00 to SarC21 and a steeply decrease for SarC36 in comparison with both SA-N_2 and MSA-CO_2. More even, it is noted that the Q_{SANS} for SarC36, the most activated carbon, has a lower value than SAR00, the unactivated carbon, despite that SA-N_2 and MSA-CO_2 increasing for SARC36 compared to Sar00. The tendency agreement between SA-N_2 and MSA-CO_2 and Q_{SANS} and Q_{SAXS} accounts for the evolution in the void fraction during the activation of Saran carbons until 21% of burn-off, SarC21. For SarC36 there is evidence of a strong change in the pore size distribution which is only detected using SANS studies.

It was found that there are differences between SAXS and SANS evaluation of scattering intensity data after the comparison of the Q values, SA-N_2 and MSA-CO_2 and pore size dimension. In comparison SAXS presents some differences for active carbons than SANS, but both techniques coincide to give a clear difference in the intensity decay of the unactivated to the other activated carbons. The mean pore size expressed by *Rg* or for the modelled (*d*), from SAXS were higher than SANS, it could be a result of the length range cover for SANS experiments that included the part of the very narrow microporosity which is blind for the X-ray beam. Hereafter, SAXS and SANS information will be compared in more detail.

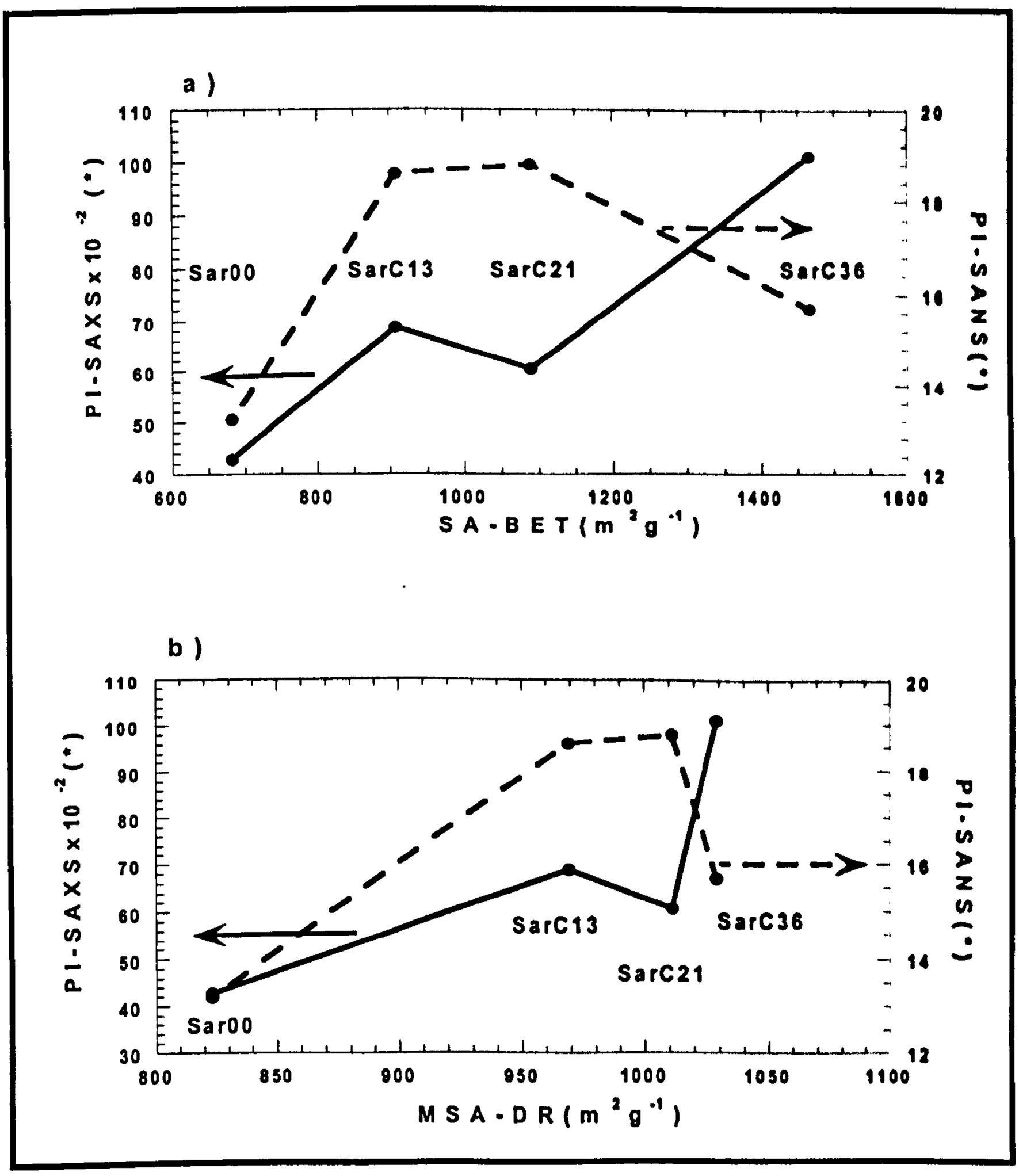

Figure 5.15: Correlation between surface area measured from a) N_2 and b) CO_2 adsorption at 77 and 273 K respectively, and *Q* calculated from SAXS and SANS analysis (the symbol * means arbitrary units).

Figure 5.16 presents the comparison between the scattering intensity data from SAXS and SANS for Saran carbons activated with carbon dioxide. As it is displayed, the scattering curves for Sar00 and SarC21 exhibited the same power law behaviour at low *q*, indicative of a fractal nature. However, SarC13 and SarC36 curves present increasing in the scattering at low *q* range sensed by SANS by not for SAXS data.

The notorious shoulder from $q > 0.3$ nm^{-1} in both SAXS and SANS data is characteristic of scattering from micropores. However, there is a marked difference between the SAXS and SANS intensities in this high q range or microporosity region. The SANS scattering intensity is greater and the q range covered by SANS was extended to high values.

According to the basic relationship between the scattering cross section, $I(q)$, and q (Equation 2.45) for SAS analysis, the contrast factor between the pore void and the solid, $C_{s,p}$, is derived different for both techniques, SAXS and SANS, depending of the nature of the source incident, X-ray and neutrons respectively. In SAXS this is defined as the electron density difference, $\Delta\rho_e$, while in SANS this is the neutron scattering contrast factor, b. It is usually assumed that $\Delta\rho_e$ is determined only by the electron density of the solid, and that this is constant, then it is feasible to put out of the integral. It was stated in Section 2.2.4 that the adsorption of gases in micropores produces an enhancement in the potential energy involved in the adsorption phenomenon as consequence of overlapping potentials from the pore walls. Therefore it can be assumed that the electron density within the micropores effectively reduces the scattering contrast between the solid and the pore void, as consequence the apparent reduced scattering intensity in the micropore region in SAXS compared with SANS can be explained and, $\Delta\rho_e$ should be a function of the micropore size, that is $\Delta\rho_e(r)$, which must be retained within the integral for SAXS analysis. On the other hand, neutron scattering is produced by interactions of neutrons with nuclei and depends only of the pore size and nothing more within pore void contributed to change b.

In summary, if SAS analyses are considered the Saran derived carbons have a microporous character with a narrow pore size distribution but, CO_2 adsorption accounts for essential microporous system with a broad distribution including a mesoporous contribution. Also, it was found that Rg remained constant when SA-N_2 and MSA-CO_2 increased which means

that the gasification proceeds not by widening of the microporous size but that new microporosity is developed. The opening of closed porosity was neglected because both no closed porous was detected by the CM-SANS experiment and at there is an agreement between BET-Surface area and Q_{SAXS}.

Figure 5.17 shows a comparison between pore width estimated from CO_2 adsorption and small angle scattering of the Saran activated carbons. The whole characterisation is provided for carbon dioxide activated carbons while for air activated carbons the comparison is restricted between gas adsorption again lifetime from positron annihilation spectroscopy. In general terms there is an agreement between the pore dimension calculated from gas adsorption with the information inferred from PALS which is highlighted by the line. In particular, it is noted that both pore width and τ for air activated samples remain practically constant in the range of burn-off studied. For carbon dioxide activated samples both L_{CO_2} and τ show a considerable increase which is evidence of pore widening conforming activation.

Similar information were draw between τ and Rg calculated from SAXS and SANS for carbon dioxide derived-carbons. In the case of Rg_{SAXS}, the Rg value increased steeply in comparison of a few change registered by τ between unactivated and 13% activated carbon. After this level of burn-off was noted a slightly decrease of Rg value which was calculated on the high q, region assigned to micropores. Rg_{SANS} exhibited the same behaviour than Rg_{SAXS} for the first step of activation (< 13% of burn-off). Then, between SarC13 and SarC36 Rg_{SANS} presented a opposite trend that Rg_{SAXS}, i.e. Rg_{SANS} was increased.

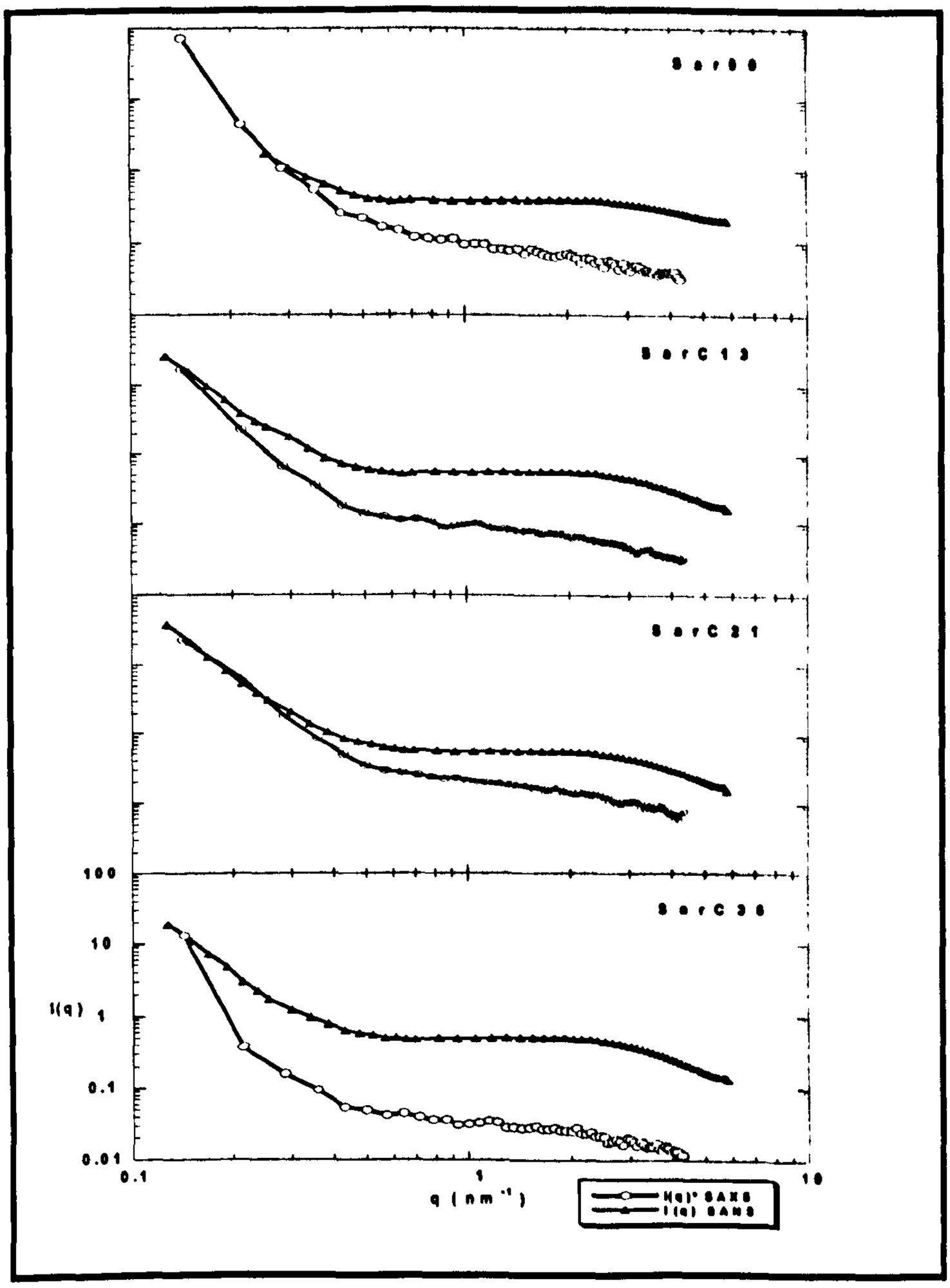

Figure 5.16: SAXS and SANS scattering intensities for Saran active carbons gasified with carbon dioxide at 1173 K. The black filled triangle signs are the SAXS data points and the white circle signs are the SANS data points.

The positron annihilation means that the lifetime depends on the overlap of positron wave function with the electron cloud around the void, thus it depends on the void size. Also, it was established that the intensity data from SAS depends on the radius size, electronic and neutron density change between void and solid phases and of shape assumed to modelled the data, i.e.,

$$I(q) = C_{1,2}^2 \, (1/V) N_p V_p^2 \, |F(q)|^2 \, S(q) \qquad (2.45)$$

First stage of gasification with carbon dioxide of Saran derived carbons, (0→ 13% burn-off): The mean electronic density, η_e, sensed by PALS remains constant, this is mean that mean pore size no change between Sar00 and SarC13 which can be justified by a compensation between ultramicro pore creation as was sensed by SAS; $d_{sas} > L_{CO2}$, and a widening process from ultramicropores to supermicropores. CO_2 molecules can be no accesses very narrow ultramicropores, $L_{CO2} > d_{sas}$. In fact mean pore width from CO_2 adsorption change agreed with the change of η_e from PAL.

Intermediate stage of gasification with carbon dioxide of Saran derived carbons, (13 → 21% burn-off): PALS showed a slight decrease of the mean η_e which account of few pore size changes. This consideration support the information obtained from SAS data analysis where intensity patter remained constant. In this case the SAXS intensity may be remain constant because $\Delta\rho_e$ inferred from PALS and radius size was invariable. Additionally, it must be concluded for these stage the shape was also constant.

The third stage of gasification with carbon dioxide of Saran derived carbons, (21 → 36% burn-off): For this step was represented by the highest decrease of the mean electron density, η_e, observed by PALS. This indicates, clearly the evolution from ultra to super micropores and of the possible formation of mesopores. Then, as is expected from the equation 2.45, *I(q)* from SAXS must be governed by both *R* and mainly by η_e. Therefore, for this stage the contrast term $\Delta\rho_e$ must be kept inside of the integral that give the intensity data. Effectively, N_2 BET-SA showed a high increase in opposition to CO_2 DR-MSA that remained constant. This is, probably by adsorption of N_2 following a multistage layers mechanism in the ultramicropores.

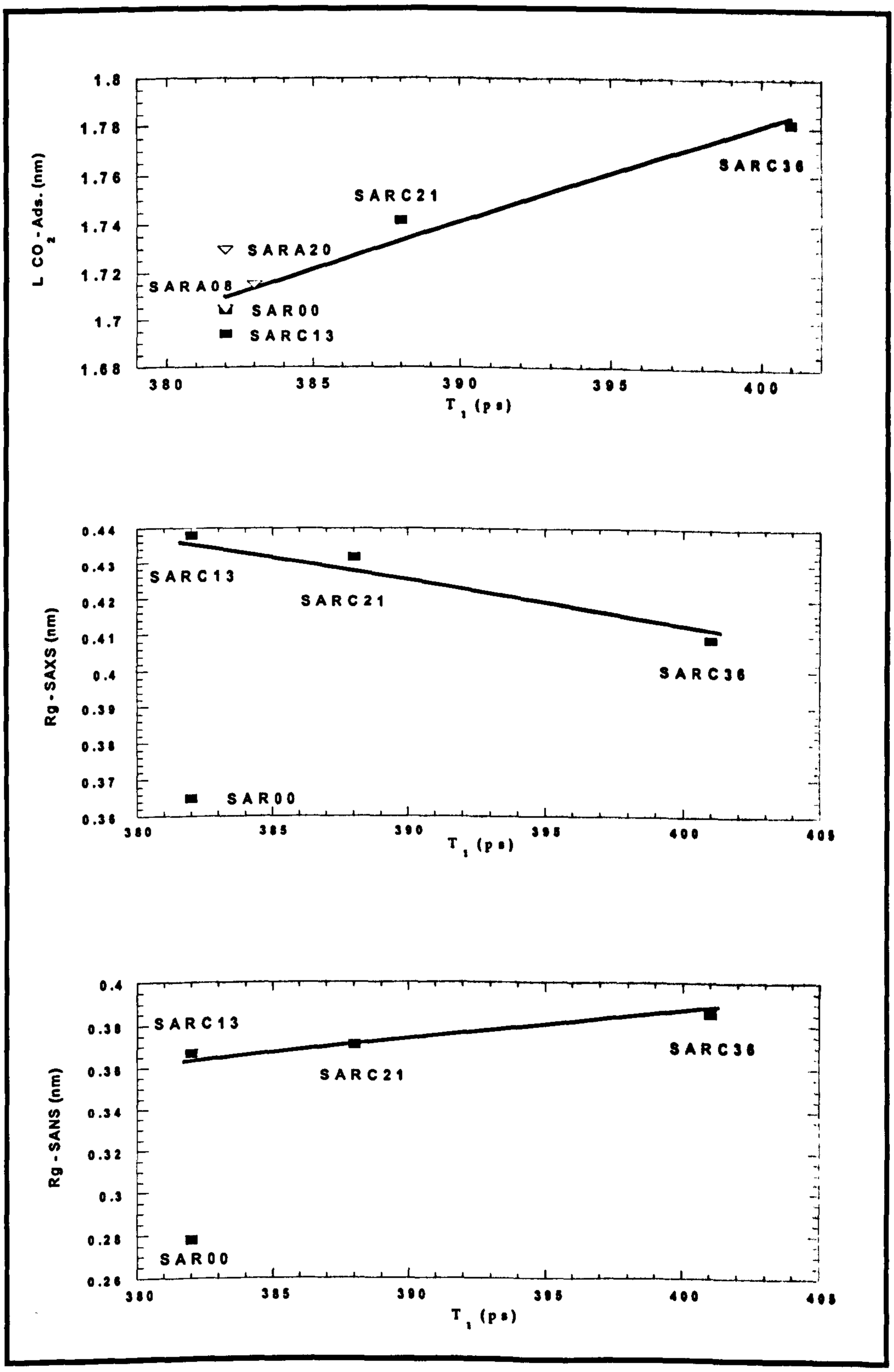

Figure 5.17: Correlation of positron annihilation lifetime with pore width deduced from gas adsorption and small-angle scattering techniques for Saran activated carbons.

For air gasification of Saran carbons: It is deduced from the comparison between gas adsorption and PALS that this activation carries on in similar

way than carbon dioxide activation. The first step (0 → 21% burn-off) exhibited that the mean electronic density and pore width were constant but the total pore volume increased. This behaviour could be represent for the apparition of new ultramicropores and join to the widening of pore size of ultramicropores. Intermediate stage of activation (8 → 20% burn-off) showed that η_e was constant; pore size from CO_2 adsorption increased slightly, the total volume increase but the micropore volume was constant. In comparison, air activation proceeds under a widening regimen at low burn-off stage than CO_2 activation.

5.2 ACTIVATED CARBON FIBERS CHARACTERISATION

In consideration that carbon fibres are essentially microporous carbon materials were selected to characterise using the conventional techniques in comparison with the novel application of the positron annihilation lifetime spectroscopy applied to this kind of materials. The original fibre was activated with carbon dioxide, the identification code is CFC then follows of the percentage of burn-off, and in the case of steam, as activating agent the code is CFS followed by the percentage of burn-off.

5.2.1 Characterisation of Active Carbon Fibers by Gas Adsorption

Carbon fibre samples was characterised by N_2 adsorption at 77K and by CO_2 adsorption at 273K. Table 5.7 shows the micropore volume calculated using DR equation (2.23) from N_2/CO_2 adsorption data, and also it is included the N_2-BET surface area. Some authors proposed a sub-classification of the micropore region defined by IUPAC (< 2 nm), [99,212] It was named submicroporosity to pores with size less than 0.7 nm and supermicroporosity to pores with size between 0.7 and 2 nm. In consideration of this for this kinds of microporous materials it is possible to

assume that the total volume is determined by the amount of N_2 molecules adsorbed at 77K and that narrow microporosity is well characterised by CO_2 adsorption at 273K. [130,225,226]

Table 5.7 shows that apparently at low percentage of burn-off (< 27%) the samples, independent of the activating agent, present a V_{N2} minor than V_{CO2} which indicates the existence of narrow microporosity caused by limited diffusion of nitrogen molecules during the adsorption. For higher percentage of burn-off, the V_{N2} is equal or higher than the V_{CO2}. This could be explained assuming a micropore widening process, which accounts for a significant quantity of supermicroporosity, calculated as V_{N2} - V_{CO2}. The presence of mesoporosity was negligible after the analysis of the respectively isotherms [125].

Table 5.7: Characterisation of active carbon fibres by physical adsorption using N_2 at 77 K and CO_2 at 273 K

Carbon Fiber	V_{N2} (cm^3g^{-1})	N_2-BET Surface Area (m^2g^{-1})	V_{CO2} (cm^3g^{-1})	V_{N2} - V_{CO2} (cm^3g^{-1})
Original	nm	nm	0.16	
CFC11	0.13	nm	0.23	-0.10
CFC40	0.37	846	0.36	0.01
CFC50	0.78	1770	0.35	0.43
CFS27	0.29	644	0.29	0.00
CFS54	0.69	1500	0.30	0.37

Nm: not measured

From the DR linear plots, the characteristic energy (Eo, in $kJmol^{-1}$) according the equation 2.23 were estimated. The mean pore size width (L_{CO2}, in nm) proposed by Stoeckli et al. was calculated according to the Equations 2.29 and 2.30. [134,219] These values are shown in Table 5.8.

It is observed that the characteristic energy, from N_2 y CO_2 adsorption data, decreases as result of increasing the mean pore size with the burn-

off. Also L was calculated from N_2 adsorption data, these results are higher than those obtained from CO_2 adsorption data, resulting in the presence of supermicropores. The clear divergence of results between both N_2 and CO_2 adsorption data is indicative of wide micropore distribution, therefore to select one of these set of values could be seen as a mistake and the mean pore size calculated is not representative. Despite of the qualitative information obtained from the N_2 / CO_2 adsorption analysis it is necessary the use of other techniques to get more confident information of the pore structure.

Table 5.8: Adsorption energies and mean pore size derived by DR from CO_2 adsorption data at 273 K

Carbon Fiber	$E_{o\,N2}$ (kJmole^{-1})	L_{N2} (nm)	$E_{o\,CO2}$ (kJmole^{-1})	L_{CO2} (nm)
Original	nd	nd	35.4	0.45
CFC11	nd	nd	33.5	0.48
CFC40	22.8	0.95	27.4	0.68
CFC50	15.1	1.59	25.7	0.76
CFS27	23.1	0.92	29.0	0.61
CFS54	13.4	1.79	24.8	0.81

nd: not determined

5.2.2 Characterisation of Active Carbon Fibers by Small Angle X-Ray Scattering (SAXS)

Figure 5.18 shows SAXS data expressed as $log(I_{(q)})$ - $log(q)$ plots for the carbon dioxide and steam activated carbon fibres. The scattering intensity tends to increase with burn-off due to the development of porosity. The general approach proposed by Guinier was used to estimate the radius of gyration (Rg) and the mean pore size according to the Equations 2.51 and 2.52. The plot of $ln(I_{(q)})$ versus q square was linear in a wide range of q values. The pore diameter was calculated assuming spherical particles by the Equation 2.52.

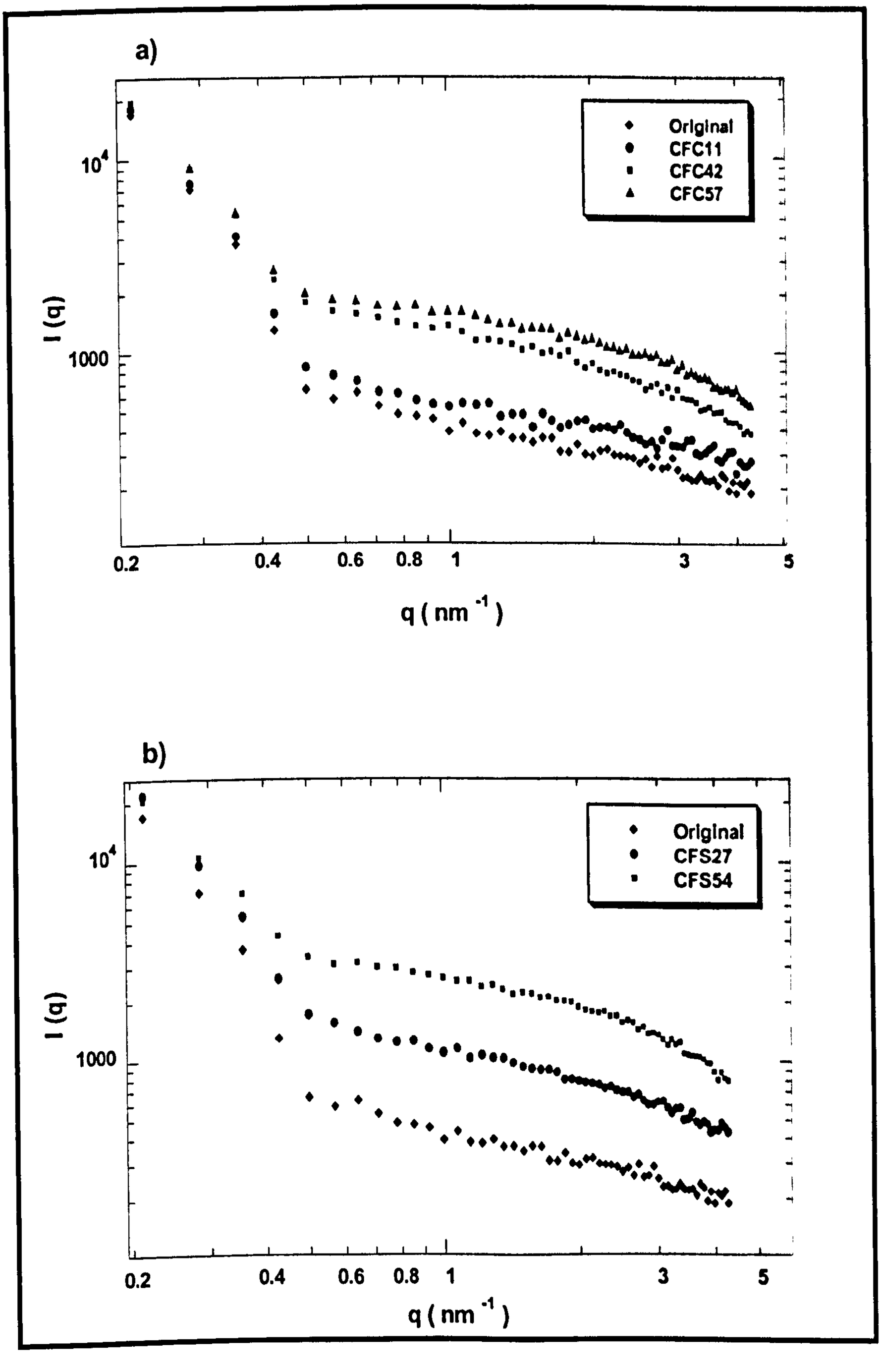

Figure 5.18: SAXS log-log plot for carbon fibres activated to different values of burn-off by activation with a) carbon dioxide and b) steam

Table 5.9 shows the values of *Rg* and *d*. It can be observed that pore size increases with burn-off. The CFC40 presents similar pore size value than CFS27 in spite of the different burn-off. In general terms, the pore size

values obtained for the carbon fibres activated with carbon dioxide are larger than those from steam activation.

Table 5.9: Radius of gyration (*Rg*) and mean pore diameter derived by Guinier formulations from SAXS data for carbon dioxide and steam activated carbon fibres

Carbon Fiber	*Rg* (nm)	*d* (nm)
Original	0.67	1.73
CFC11	0.69	1.78
CFC40	0.73	1.88
CFC57	0.75	1.94
CFS27	0.73	1.88
CFS54	0.79	2.04

5.2.3 Characterisation of Active Carbon Fibers by Positron Annihilation Spectroscopy (PALS)

Positron annihilation spectra were fitted to obtain lifetimes (τ_i) and the corresponding intensities (I_i). For these active carbon fibres the best fit was obtained deconvoluting into two lifetimes, a short lived component ranging from 376 to 393 ps and a long lived component ranging from 1247 to 1898 ps. Table 5.10 shows the parameters obtained for the samples analysed. According to the Section 2.4.5, it was established that a lifetime of 400ps has been assigned to annihilation of positron by interaction with the electron density at the surface and near-surface regions, and the longest lifetime is assigned to annihilation of ortho-positronium previously formed in specific defects on the surface of the activated carbon fibres. A previous work [197] on PAN-based carbon fibres assumed that the only one lifetime found, ranging from 373 to 441 ps, represents the electron density at near-surface region according to the heat and chemical treatments which change their chemical composition and the specific surface area.

It is noted that when the pores are wider the probability of interaction between the positron and the surface electron density in the micropore walls decreases. The shortest lifetime presents the highest intensity,

approximately 90% of the total intensity. In this case it is possible to attribute to positron annihilation into the microporosity which is the main characteristic of these samples. This argument can explain the reduction of the intensity of the samples with the similar burn-off, i.e. CFC57 (98.1%) and CFS54 (86.5%), and similar conclusion can be inferred of the comparison of CFS27 (94.3%) and CFS54 (86.5%); in fact the last sample CFS54 has the widest pore size.

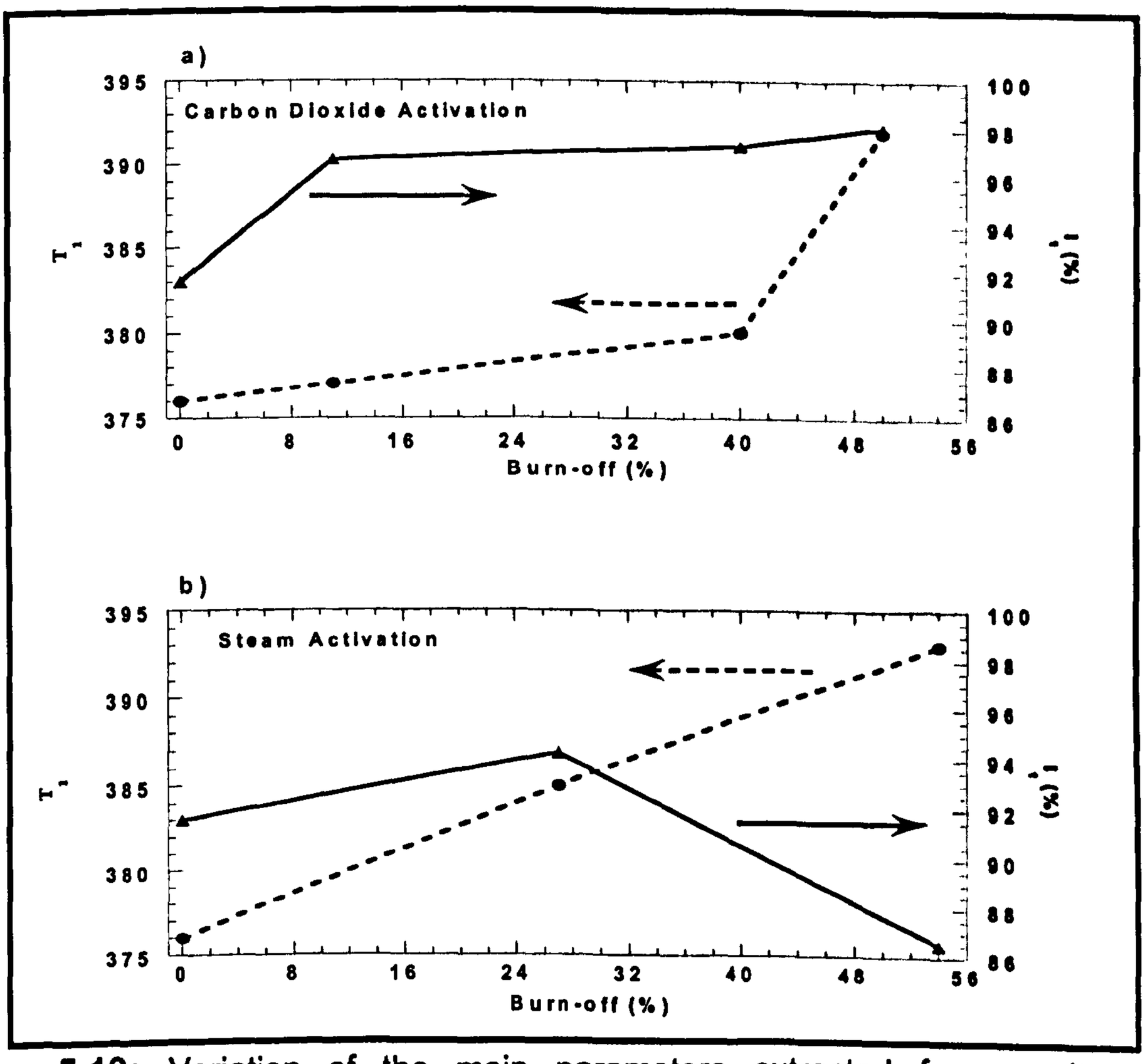

Figure 5.19: Variation of the main parameters extracted from positron annihilation spectrum, τ_1 (ps), and I_1 (%) with burn-off, a) Carbon dioxide and b) Steam

Figure 5.19 shows the intensity and the τ_1 value against burn-off. There is a clear increasing tendency of τ_1 and I_1 with the activation by CO_2, which is evidence of the developing of microporosity by this gas. The τ_1 analysis for steam activated fibres follows the same behaviour than those activated

with carbon dioxide. However, the value intensity decreases at higher conversions showing a reduction in its microporosity character.

Table 5.10: Lifetimes and intensities derived by fitting the data from PALS for carbon dioxide and steam activated carbon fibres

Carbon Fiber	τ_1 (ps)	I_1 (%)	τ_2 (ps)	I_2 (%)
Original	376	91.6	1302	8.4
CFC11	377	96.7	1515	3.3
CFC40	380	97.3	1562	2.7
CFC50	392	98.1	1898	1.9
CFS27	385	94.3	1463	5.7
CFS54	393	86.5	1247	13.5

5.2.4 Correlation of the Characterisation by Positron Annihilation Spectroscopy (PALS) with Gas Adsorption and Small Angle Scattering

Firstly, the microporosity data obtained by gas adsorption and SAXS will be discussed. Figure 5.20 compares the characteristic energy calculated from CO_2 adsorption with the *Rg* obtained from SAXS. Here, it is considered that the inverse value of *Eo* and *Rg* are proportional to the pore size. The plot shows a good agreement between both techniques.

However, it is observed that for all the samples the mean pore size; calculated from *Rg* assuming spheres, is larger that one calculated using the experimental equations proposed for CO_2 adsorption analysis, (Equation 2.52, 2.29 and 2.30). From the analysis of mean diameter, *d*, calculated of *Rg*, it is deduced an essentially microporosity system.

As result the similar trend of SAXS and CO_2 adsorption it is possible now to relate this behaviour with the results found from positron annihilation spectroscopy.

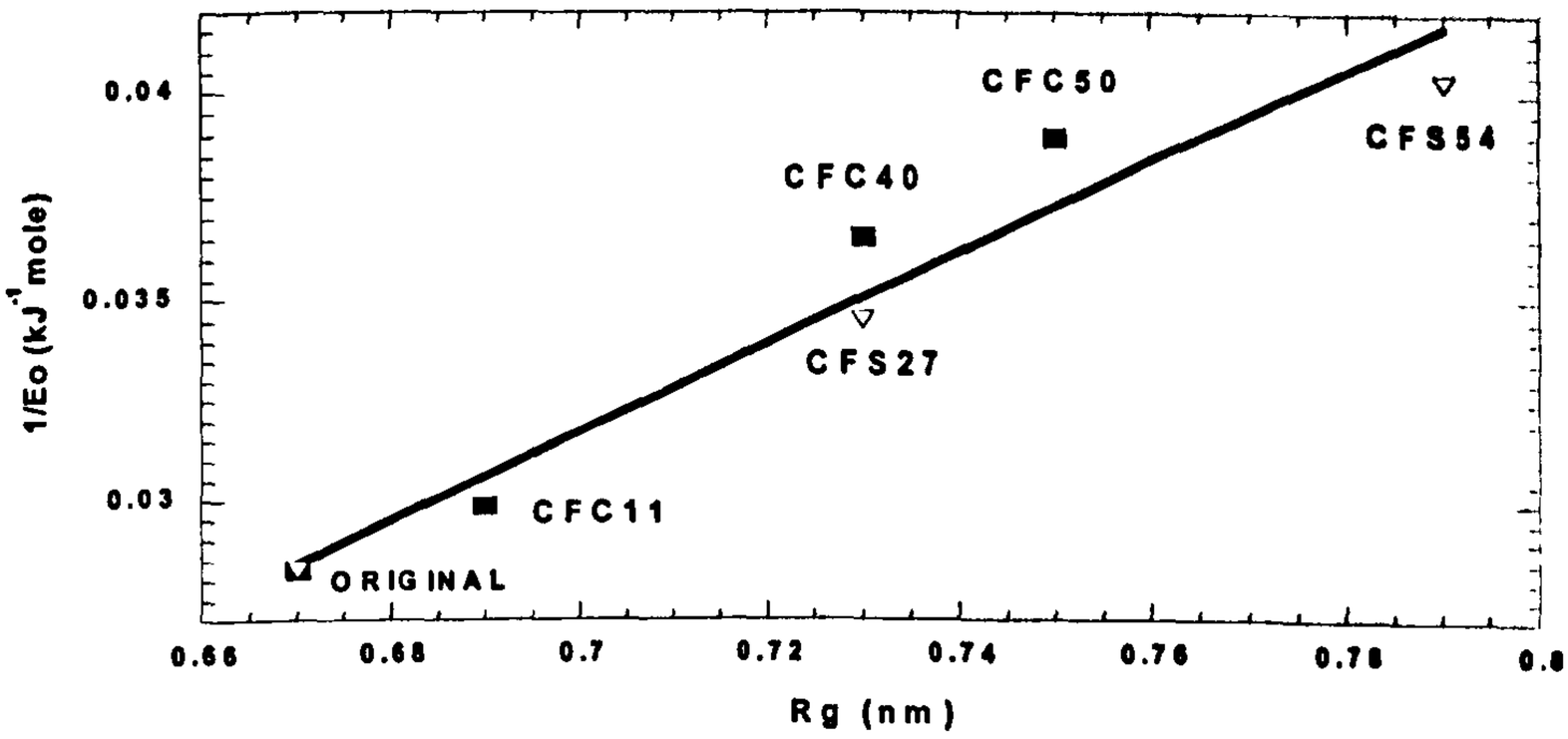

Figure 5.20: Correlation between the characteristic energy (*Eo*) evaluated from CO_2 adsorption at 273K and radius of gyration (*Rg*) from SAXS for ACF

Figure 5.21 shows the comparison between pore size estimated from gas adsorption and SAXS with the shortest lifetime. A good linear tendency is deduced from these plots between τ_1 and pore size for both carbon dioxide and steam activated carbon fibre sets. Previous research found a dependence of τ_1 and others surface parameters, like surface area, but they did not clearly settle the relationship found in this work for these materials [193,194,199].

Figure 5.22 shows the correlation between the longest lifetime, o-Ps, with the pore size parameters, calculated from CO_2 activated carbon fibre samples. There is a good correlation between τ_2 and both *L* and *d*. For the highest activated CFS sample there is a clear deviation of the tendency exhibited for similar activated CFC sample, as a result is not possible to generalise any trend against τ_2 for these samples in the range of burn-off studied.

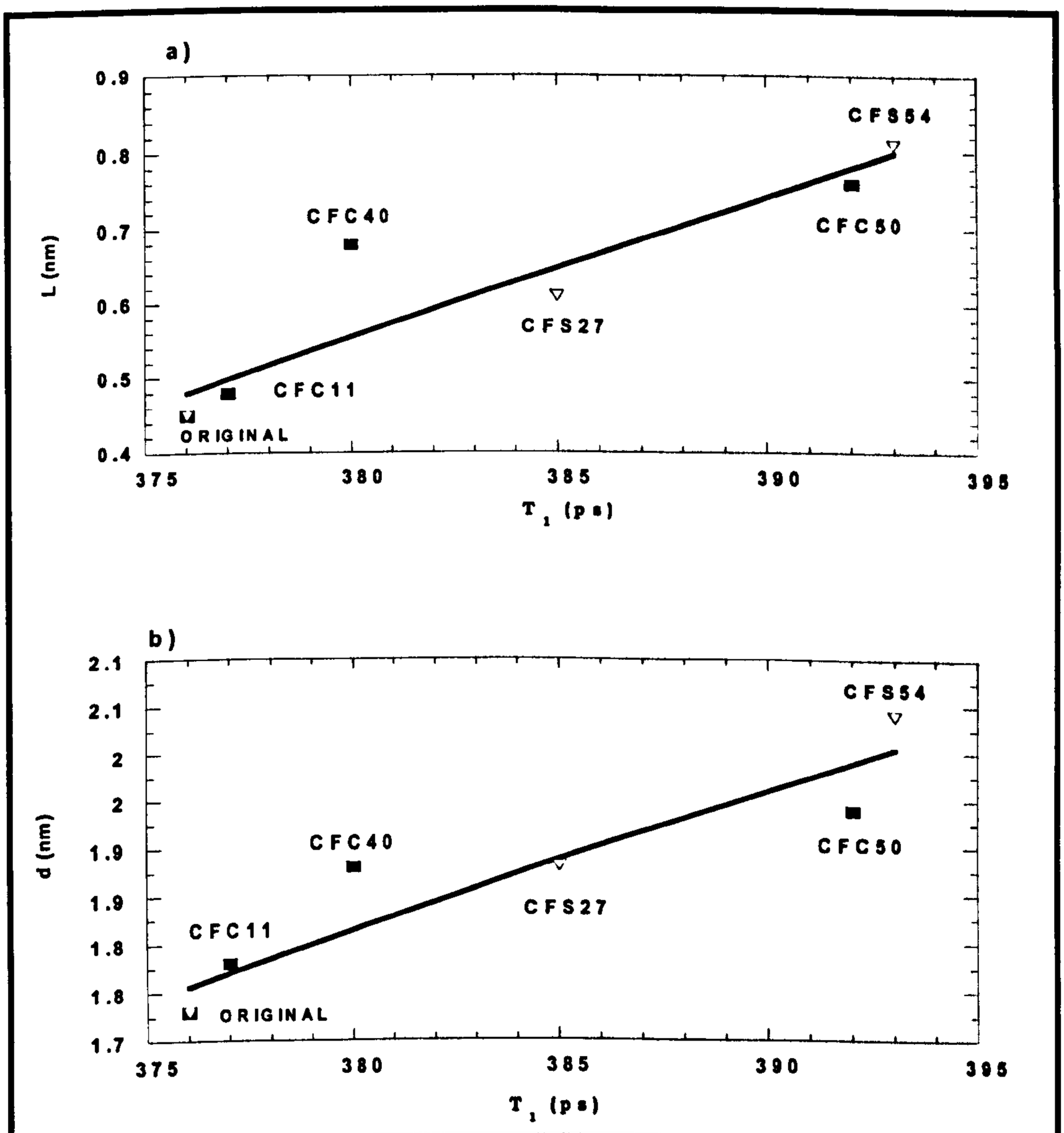

Figure 5.21: a) Pore size (*L*) evaluated from CO_2 adsorption at 273K, and b) width dimension (d) from SAXS are compared to the shortest annihilation lifetime (τ_1) calculated from PALS for ACF

Mean lifetime which was defined by the Equation 2.74 is represented again the mean pore size, *L*, obtained from SAXS in Figure 5.23. It is observed the same behaviour as τ_2, suggesting that the longest lifetime controlled the mean annihilation process in these porous solids but its intensity, I_2%, or amount of positrons which annihilates by a determined mechanism is secondary compared with I_1%. This means, that the main characteristic sensed by PALS is the correlation between τ_1 and microporosity character, as was inferred by gas adsorption and SAXS analysis.

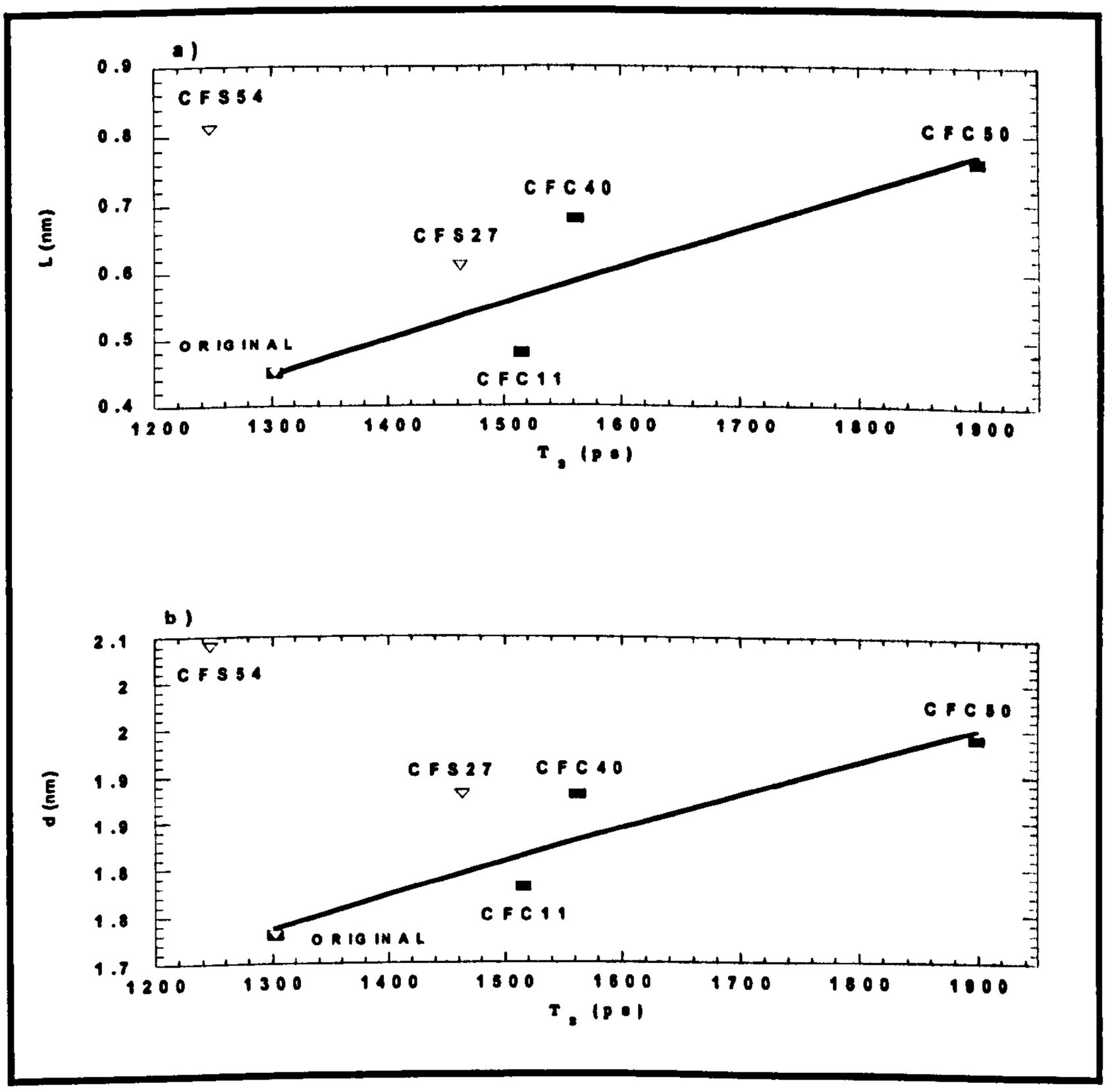

Figure 5.22: a) Pore size (L) evaluated from CO_2 adsorption at 273K and, b) width dimension (d) from SAXS compared to the longest annihilation lifetime (τ_2) calculated from PALS for ACF

In section 2.4 it was mentioned that the annihilation rate of positrons in a medium, obtained from PALS is only function of its inherent electronic density (Equation 2.66). Accordingly, from the results above described, it is inferred that electron density in the structure of ACF is changing with the evolution of microporosity. Also, it was found from the gas adsorption and SAXS that the pore size changes. In the first steps of the gasification when the developing of microporous is predominant, the pore size increases against of the decrease of the electron density, on the high steam activated fibre, it was found an inverse behaviour. It is published in a number of investigations that steam gasification on carbonaceous

materials essentially trends to widen the pore instead to develop new microporosity at high levels of burn-off [56,98,228-230].

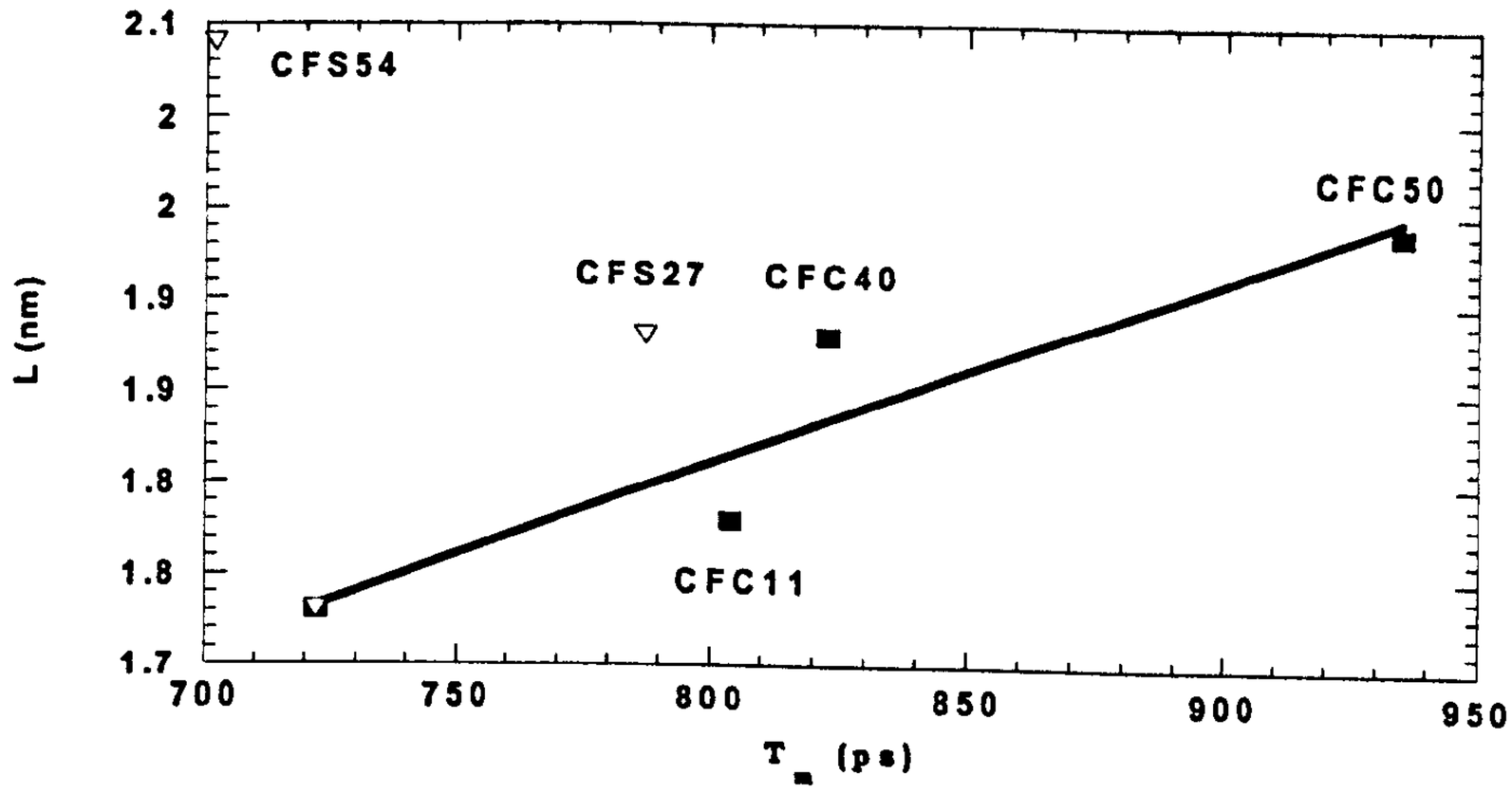

Figure 5.23: Correlation of the pore size expressed width dimension (d) from SAXS against the mean annihilation lifetime (τ_m) calculated from PALS for ACF

SAXS intensity is function, similar to PALS, of the electronic density as well as of structure form factor, which depends of the radius and geometry of the pore (Equation 2.45). In this sense, it is not feasible to attribute the increase of the intensity seen in SAXS analysis only to radius evolution as was derived for the mean electronic density from PALS. Because the pore size reaches a value determined, the shape plays a important role modifying the scattering intensity value. At low levels of burn-off the scattering intensity data depended essentially of the change in the electronic density in ACF microporosity .

6. RESULTS AND DISCUSSION: GASIFIED COAL CHARS

6.1 CARBONISATION AND ACTIVATION OF SAMPLES

Coal is an important feedstock for the production of activated carbons; the literature shows much interest in development of further high value added products from coal. Generally activated carbons, after a gasification process, reach commercially interesting surface areas of the order 500 m^2/g.

There are two characteristics that determine the properties of an active carbon, one is the chemical nature of its surface; and the second is significant to the pore structure. The development of porosity in coal chars during combustion, gasification or activation is of considerable fundamental interest; but the control of the pore structure in these reactions is not an easy task, since to the complexity of the processes involved. This chapter is mainly concerned with the characterisation of the porosity in activated coal chars at low burn-off, due that this early stage is significant to control of the porosity in the production of active carbon from coal.

Pittsburgh and Illinois Argonne Premium coals were treated according to experimental procedure described in Section 4.2.2. The char yield obtained in the pyrolysis was 63.5% and 58.2% for Pittsburgh and Illinois, respectively. These coals are bituminous, high rank coals that contain large amounts of aliphatic or hydroaromatic clusters connected by weak aliphatic and ether bridges [210,227]. Pittsburgh coal, different to Illinois, has low crosslink density and goes through fluid phase during pyrolysis. As a result of these considerations, carbonisation yield was high for both

charcoals and it was expected a low or nonporous materials, which will be analysed thereafter.

Table 6.1 : Description of the samples prepared according to the parental coal, the activation gas, and the Burn-off (%) level.

Activation Agent	Char Code	Burn-off (%)*	Ash (%)*
Gasified Pittsburgh chars			
Unactivated	Pit00	0.0	14.1
Air	PitA05	5.0	15.7
	PitA16	15.5	16.7
	PitA22	22.4	18.6
Carbon dioxide	PitC04	4.3	14.7
	PitC09	8.7	15.4
	PitC13	13.1	16.2
Steam	PitS09	8.8	15.2
	PitS11	11.0	16.4
Gasified Illinois chars			
Unactivated	Ill00	0.0	25.3
Air	IllA04	4.2	26.8
	IllA09	8.8	28.6
	IllA17	16.6	31.4
Carbon dioxide	IllC03	2.5	25.9
	IllC08	7.6	27.5
	IllC11	11.4	28.5
Steam	IllS10	10.2	25.9
	IllS21	21.0	31.7

* dry basis

Table 6.1 shows the different values of burn-off (%) after activation with dry air at 673 K, carbon dioxide at 1173 K and steam at 1173 K. The code used in this work describe the parental coal as Pit for Pittsburgh, and Ill for Illinois; the activation process is represented by a capital letter, thus: A to air activation, C to carbon dioxide activation, and S to steam activation; and the percentage of burn-off is represented in the last two digits. For example, PitA05 means Pittsburgh coal char activated in air at 5 % of burn-off.

6.2 GAS ADSORPTION CHARACTERISATION

Activated Pittsburgh chars were characterised using nitrogen adsorption at 77K. Figure 6.1 and 6.3 show the 77K nitrogen adsorption isotherms. They were isotherms of type II according to the IUPAC classification [99,113]. This shape is typical to either a nonporous material, or a mix of

meso- and microporous material with low porosity. The nitrogen adsorption of the unactivated Pittsburgh coal char was negligible.

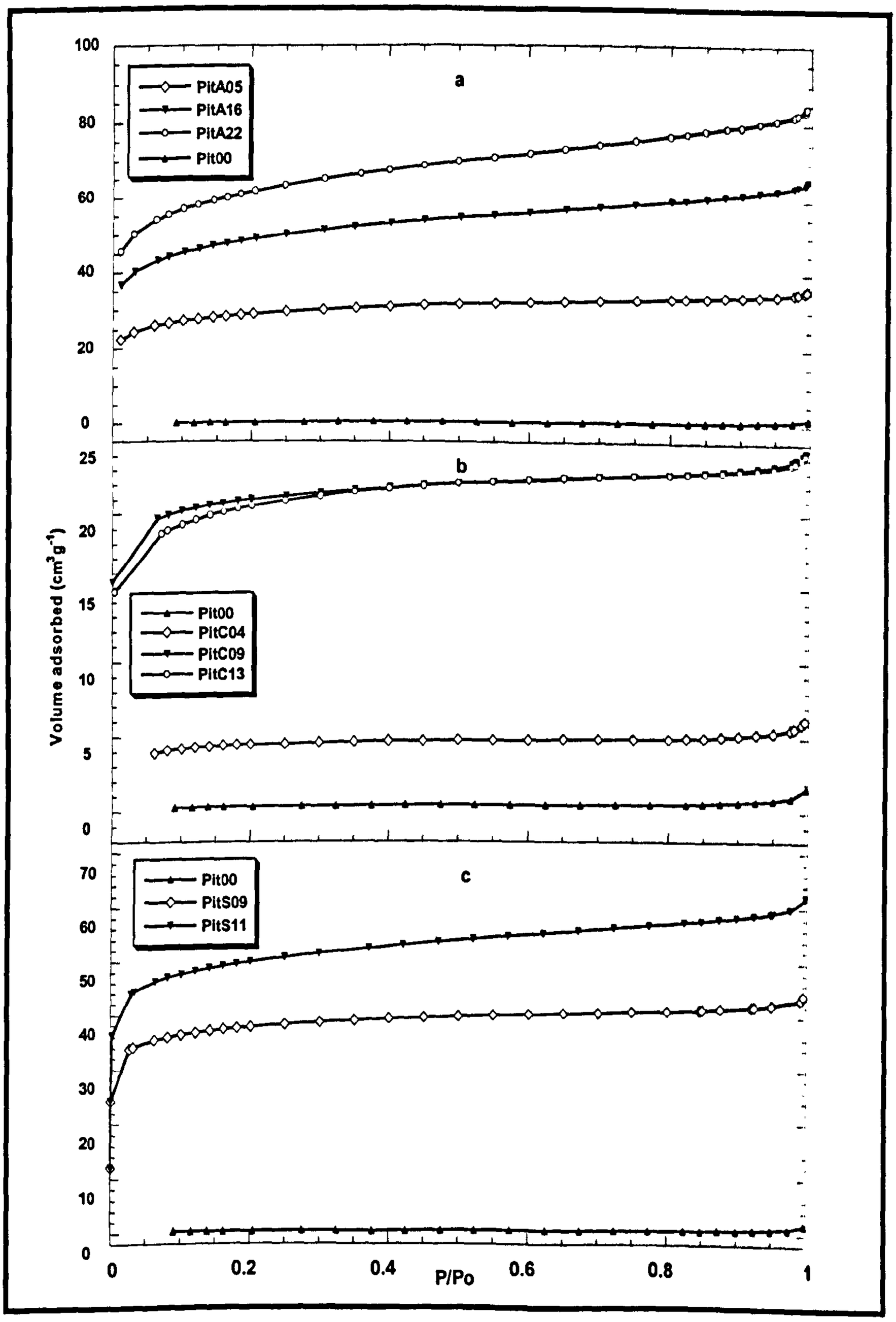

Figure 6.1: 77K N_2 adsorption isotherms for activated Pittsburgh coal chars in: a) air at 673K, b) carbon dioxide at 1173K, c) steam at 1173K.

The Pittsburgh activated coals chars showed an important increase of gas adsorption at low relative pressure, it can be associated to microporous contribution. A general analysis of the adsorption nitrogen capacity shows

an increase of porosity, in the order of: air, steam and carbon dioxide activation. Also, 77K nitrogen adsorption-desorption isotherms were carried out for activated Pittsburgh chars; however the desorption points were not included in Figure 6.1 and 6.3, in order to simplify the graph. For comparison with Figure 2.2, it was found that the isotherms presented hysterisis loops of type H4; this fact is often associated with capillary condensation in mesopore structures with narrow slit-like pores [106]. Low pressure hysteresis was also observed. As a result of the considered in the Section 2.2.5 a possible explanation for this phenomenon can be attributed to irreversible retention of nitrogen molecules in pores with approximately the same width in comparison to the nitrogen molecule size, as well to diffusion of nitrogen molecules through microporous constrictions.

Surface areas for activated Pittsburgh chars were calculated using BET nitrogen adsorption approach (2.14), because this is the most widely used analysis for the isotherms of type II or IV; however I recognize the limitations of this approach. The range of linearity of *P/Po* used to calculate the surface area was of 0.06-0.20. Table 6.2 shows the values of surface area found for activated Pittsburgh and Illinois coal chars. Analysis of BET surface area values in Pittsburgh coal chars showed an increase of surface area with the activation process, which suggests development of porosity, and this tendency is not depending of activate gas. This has been previously observed [85,94,134] and is essentially indicative of new micropore systems for low degree of activation. That is not happened in the activation for Illinois coal chars. Air and carbon dioxide gasification in Illinois chars showed a decrease of the surface area (BET) to the char activated above of 10% of burn-off. The other hand, steam gasification showed a drastic effect on Illinois chars; as a result high surface area values were obtained.

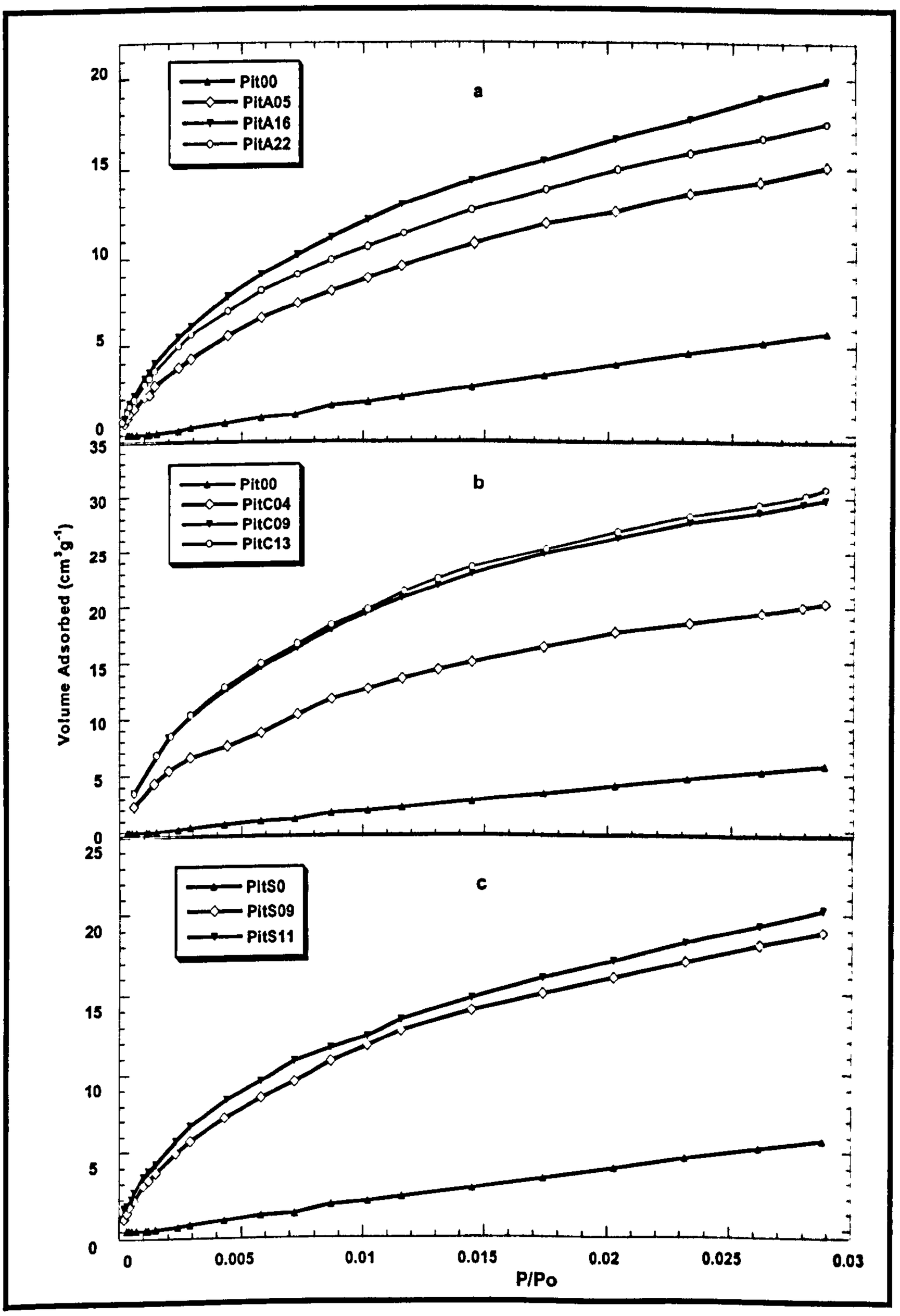

Figure 6.2: 273 K CO_2 adsorption isotherms for activated Pittsburgh coal chars in: a) air at 673K, b) carbon dioxide at 1173K, c) steam at 1173K.

At this time, the increase in surface area could be attributed to an increase of microporosity or/and a increase of mesoporosity. As usual in adsorption characterization to deal with this matter, it is recommended to run adsorption experiments using other molecule probes. A number of research papers suggest CO_2 adsorption experiment to characterise a

microporous carbon materials [37,49,113,130]. In this work was carried out the CO_2 adsorption experiment for coal chars.

The Figure 6.2 and 6.4 show the CO_2 adsorption isotherms at 273K of activated Pittsburgh and Illinois coal chars, respectively. The CO_2 volume adsorbed increase according to burn-off per cent. It could be associated to developing of microporosity, but pore filled mechanism of the CO_2 molecules in mesoporous also it is possible. Also, the form of these graphs do not defined clearly a microporous material, because they neither exhibit a long and well defined plateau, nor a sharp neck a low P/Po; which are characteristics that define a micropore system (see Figure 2.2, in order to compare).

It is noted, different to the N_2 adsorption analysis, that unactivated Illinois coal char adsorbed a considerable volume of CO_2, then a micropore system can be inferred, which is not assessable by N_2 molecules, this is so-called ultramicroporosity (micropores < 0.7nm). Consequently, the microsurface area value were 110 and 374 m^2/g for unactivated Pittsburgh and Illinois coal chars, respectively.

The Table 6.2 also shows equivalent microsurface area values calculated using to the DR approach for all samples. In general terms, the value of microsurface area increase according to burn-off for Pittsburgh activated chars, (the exception is PitA22), and decrease for Illinois activated chars, (the exception is steam series). Therefore, the origin of the parental coal determines the development of porosity. For Illinois coal chars at low burn-off suddenly increased the micoporosity, specially with carbon dioxide and air activate. For Pittsburgh coal char the develop of porosity was very slow.

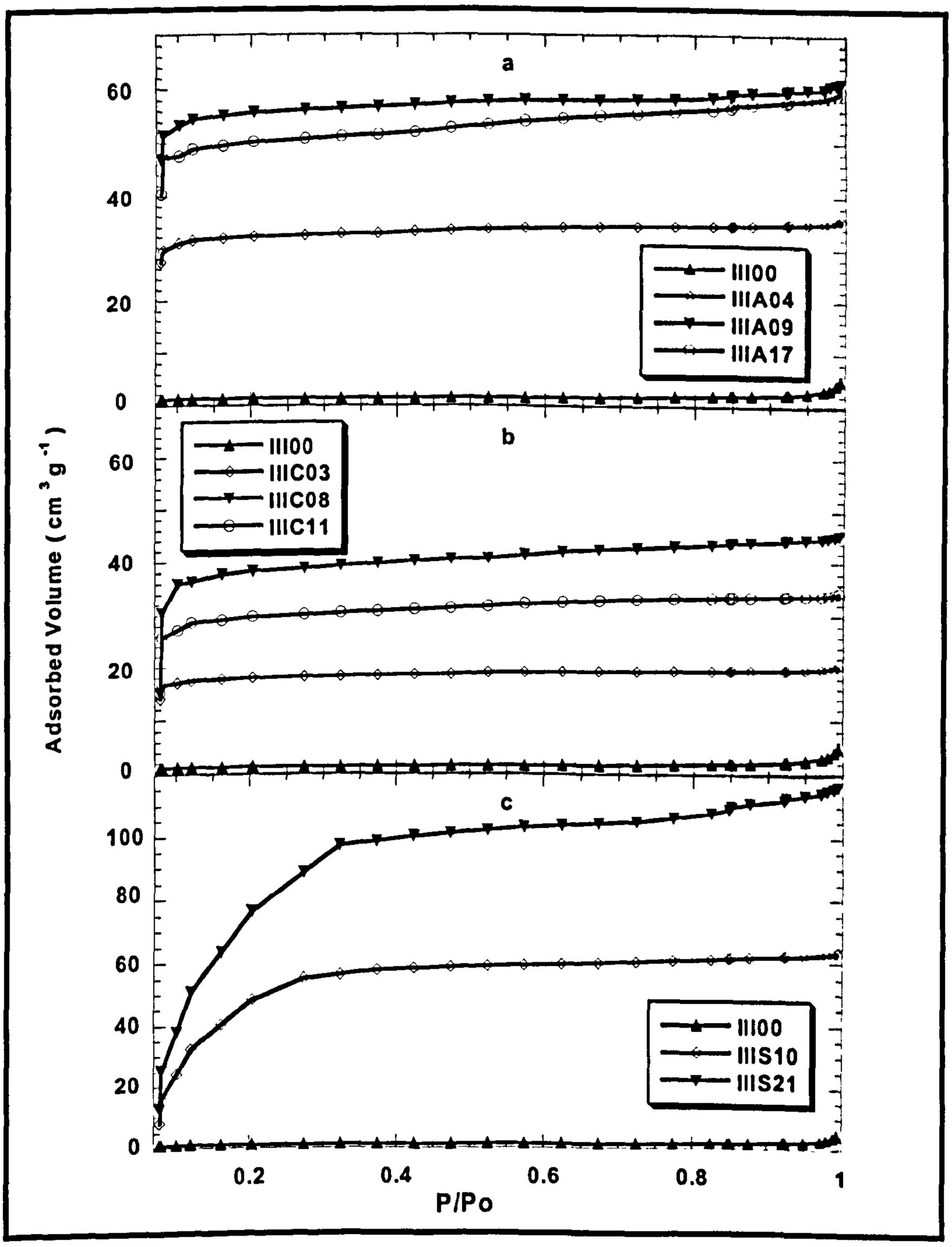

Figure 6.3: 77K N_2 adsorption isotherms for activated Illinois coal chars in: a) air at 673K, b) carbon dioxide at 1173K, c) steam at 1173K.

Figure 6.5 and 6.6 show a comparison between the volume adsorbed of N_2 and CO_2, because the surface area value by either BET or DR approaches depends of the original data in adsorption experiments, (i.e. the quantity of volume adsorbed). It can see a gap between volume adsorbed of N_2 and CO_2 (with exception of steam gasification), just after

that the gasification process starts, and therefore molecular sieve behaviour is noted for both coal chars. In terms of the use of these materials, this characteristic is very important for gas-phase applications (for example to flue gas cleanup, to selective retention of pollutant removal from waste water or to confine molecules).

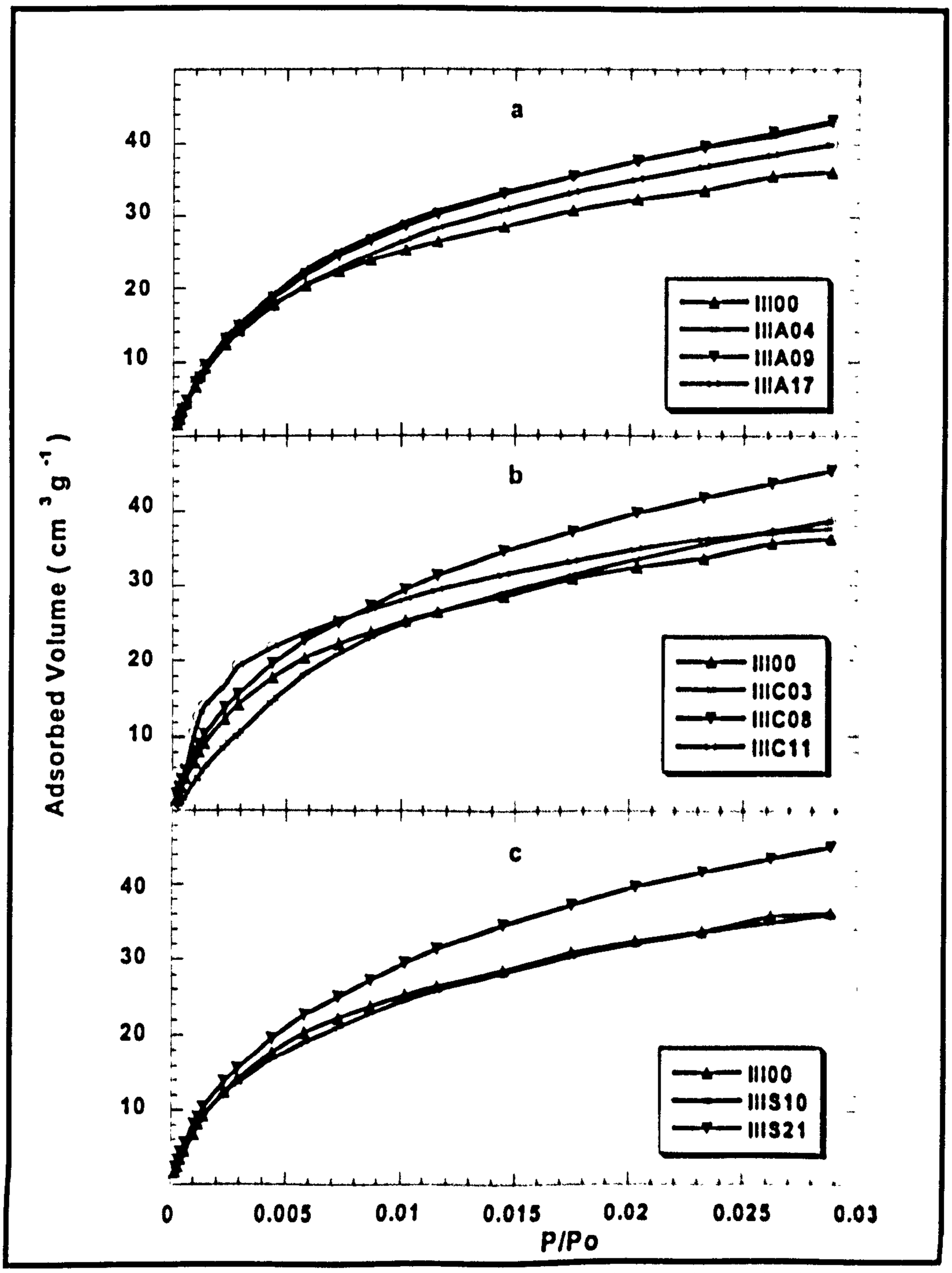

Figure 6.4: 273 K CO_2 adsorption isotherms for activated Illinois coal chars in: a) air, b) carbon dioxide, c) steam.

Table 6.2: Characterisation of Pittsburgh and Illinois coal chars, activated with air, carbon dioxide and steam by physical adsorption using N_2 at 77 K and CO_2 at 273 K

Carbon	V_{N2} ($cm^3 g^{-1}$)	N_2-BET Surface Area ($m^2 g^{-1}$)	V_{CO2} ($cm^3 g^{-1}$)	CO_2-DR Micro Surface Area ($m^2 g^{-1}$)
Gasified Pittsburgh chars				
Pit00	0.003	2	0.044	110
PitA05	0.054	99	0.055	137
PitA16	0.098	174	0.070	174
PitA22	0.127	215	0.063	156
PitC04	0.010	15	0.089	223
PitC09	0.038	69	0.115	287
PitC13	0.038	72	0.116	290
PitS09	0.068	99	0.070	174
PitS11	0.096	174	0.071	177
Gasified Illinois chars				
Ill00	0.008	4	0.149	372
IllA04	0.060	116	0.183	456
IllA09	0.099	187	0.173	431
IllA17	0.081	177	0.154	385
IllC03	0.035	63	0.198	494
IllC08	0.083	137	0.165	412
IllC11	0.057	105	0.155	387
IllS10	0.105	202	0.140	355
IllS21	0.190	354	0.167	416

Experimental reproducibility ranged between 1.8 and 6.1%, which was calculated with a second run with fresh sample of char.

It was noted that N_2 adsorption presented evidence for activated adsorption caused by microporous constrictions. The other hand, CO_2 adsorption could be caused by contribution of micropores and mesopores. Despite of the limitations to obtain quantitative information about the porosity in these materials by N_2 and CO_2 adsorption methods, some characteristics were cleared out.

A general analysis can be infer that there is development of porosity for air, carbon dioxide and steam gasification, probably with broad pore size distribution in Pittsburgh chars because a mixture of meso- and micropores was inferred.

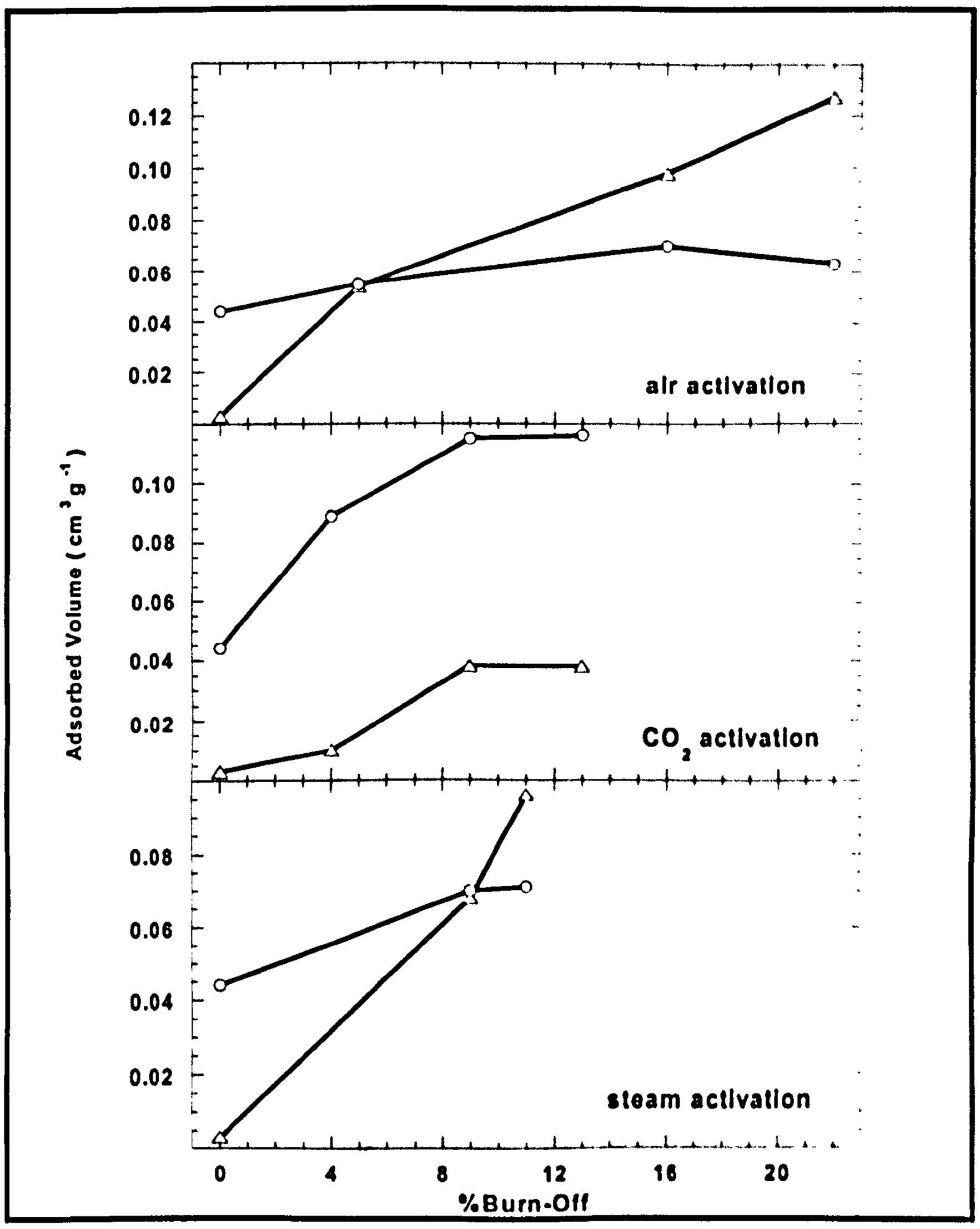

Figure 6.5: Nitrogen and carbon dioxide volume adsorbed in Pittsburgh coal chars. Δ N_2, O CO_2

In particular, it was found that the development of microporosity is promoted by CO_2 gasification (below 15% of burn-off), for both Pittsburgh and Illinois coals, in the case of Illinois, also by air activation. As a result for these chars; until 15% of burn-off shows molecular sieve properties, above this value the pore size apparently increased. Steam gasification produces; apparently a mesoporous chars with narrow distribution in the range of burn-off studied.

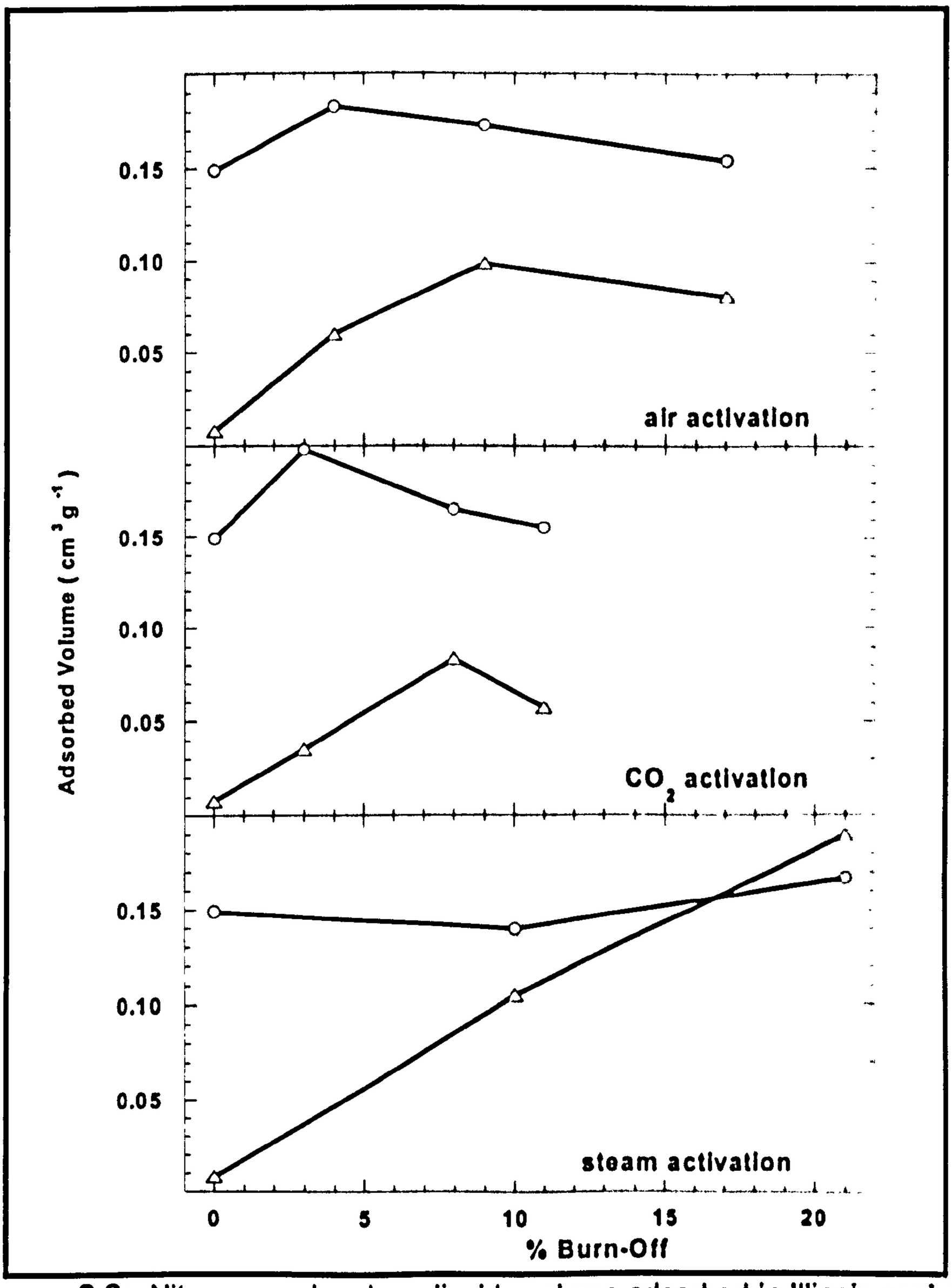

Figure 6.6: Nitrogen and carbon dioxide volume adsorbed in Illinois coal chars. $\Delta\ N_2$, O CO_2

Hence, adsorption methods allow for an important qualification of the porous chars, in addition this work characterised by SAS and introduced the use of PALS technique in order to obtain the best approach to the pore system formed, and therefore information about of the gasification

mechanism. SAS and PALS are enable techniques to sense the electron density into near surface regions in condensed materials.

6.3 Small Angle Scattering Characterisation (SAXS-SANS)

In the section 2.3 was settled that the scattering intensity mainly depends of the contrast factor, $C_{i,j}$ (Equation 2.45); which is defined as the electronic density (electrons) or length (neutrons) difference between two phases, if the ideal two phase model is assumed. In this case, it is assumed that one phase is the dense coal char, and the other one is the pore fraction originated during gasification of char. As usual, the best way to represent SAS results is through of a log-log small-angle scattering curve of the intensity I(q) versus the vector q; Figure 6.7 and 6.8 show SAXS, and Figure 6.9 and 6.10 show SANS results for Pittsburgh and Illinois coal chars respectively.

In the case of Pittsburgh char activation, SAXS curves showed that all of the intensity of the gasified char was higher than unactivated char. It was noted a increase of SAXS intensity data with burn-off, in particular using air and steam. However, the comparison between gasified chars showed small differences.

Assuming that the SAXS intensity data is only produced by scattering in porous medium again coalchar, it can be noted that at low activation level, (PitA05 and PitC04), the micro and meso pore region showed a considerable development, whereas the activation between 5 and 22% of burn-off produce a slight changes in the porosity. For PitS09 and PitS11 there was evidence of mesopores formation; however, the intensity profiles were very close.

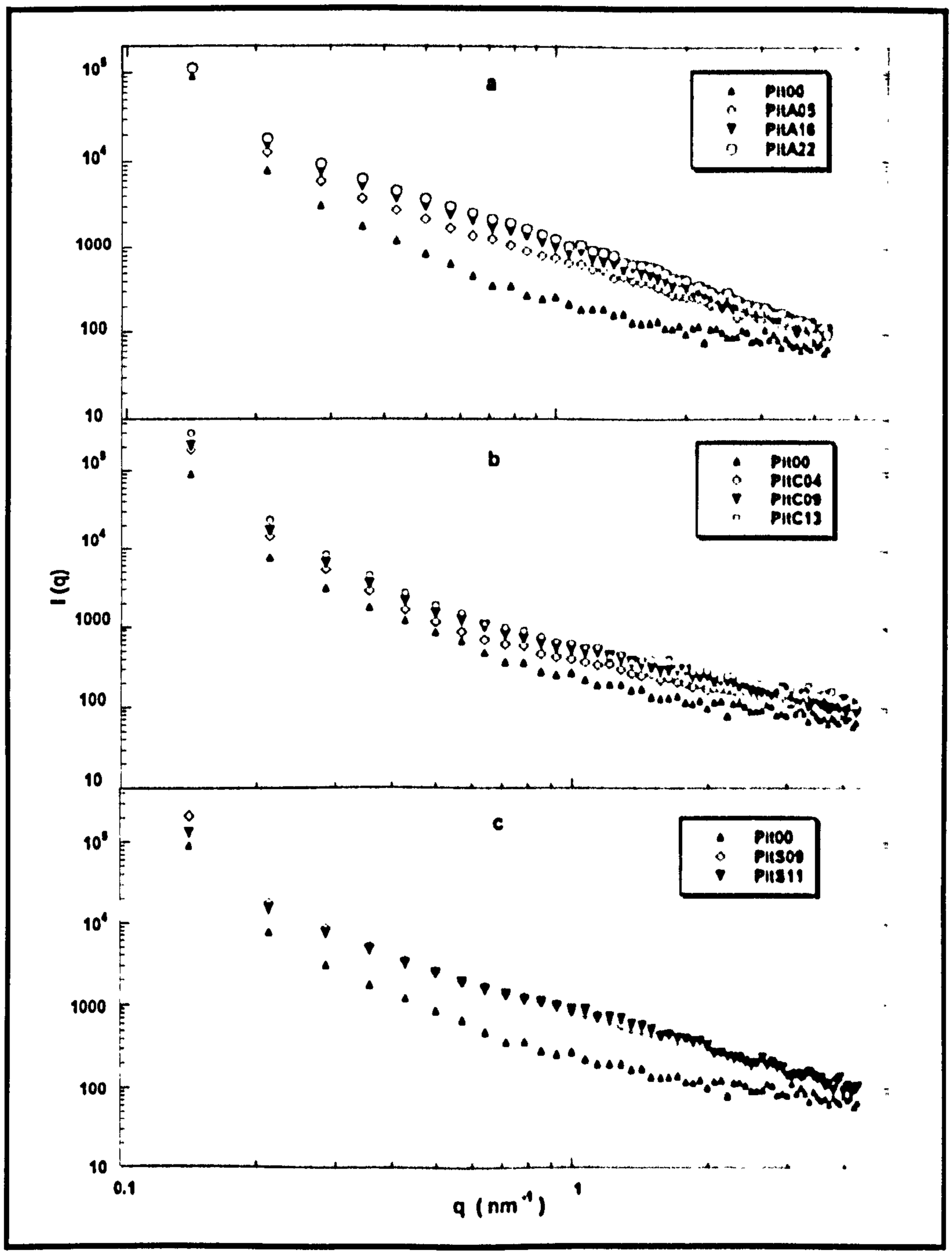

Figure 6.7: SAXS log-log plots for activated Pittsburgh coal chars with: a) air at 673K, b) carbon dioxide at 1173K, c) steam at 1173K.

In the case of Illinois, only the activation with steam at 21% of burn-off showed a considerable difference in SAXS intensity compared again the unactivated char. For chars gasified with air this difference was negligible and slight in the case of carbon dioxide activation. That means there is development of microporosity in carbon dioxide gasification and very evident creation of mesoporosity in steam gasification.

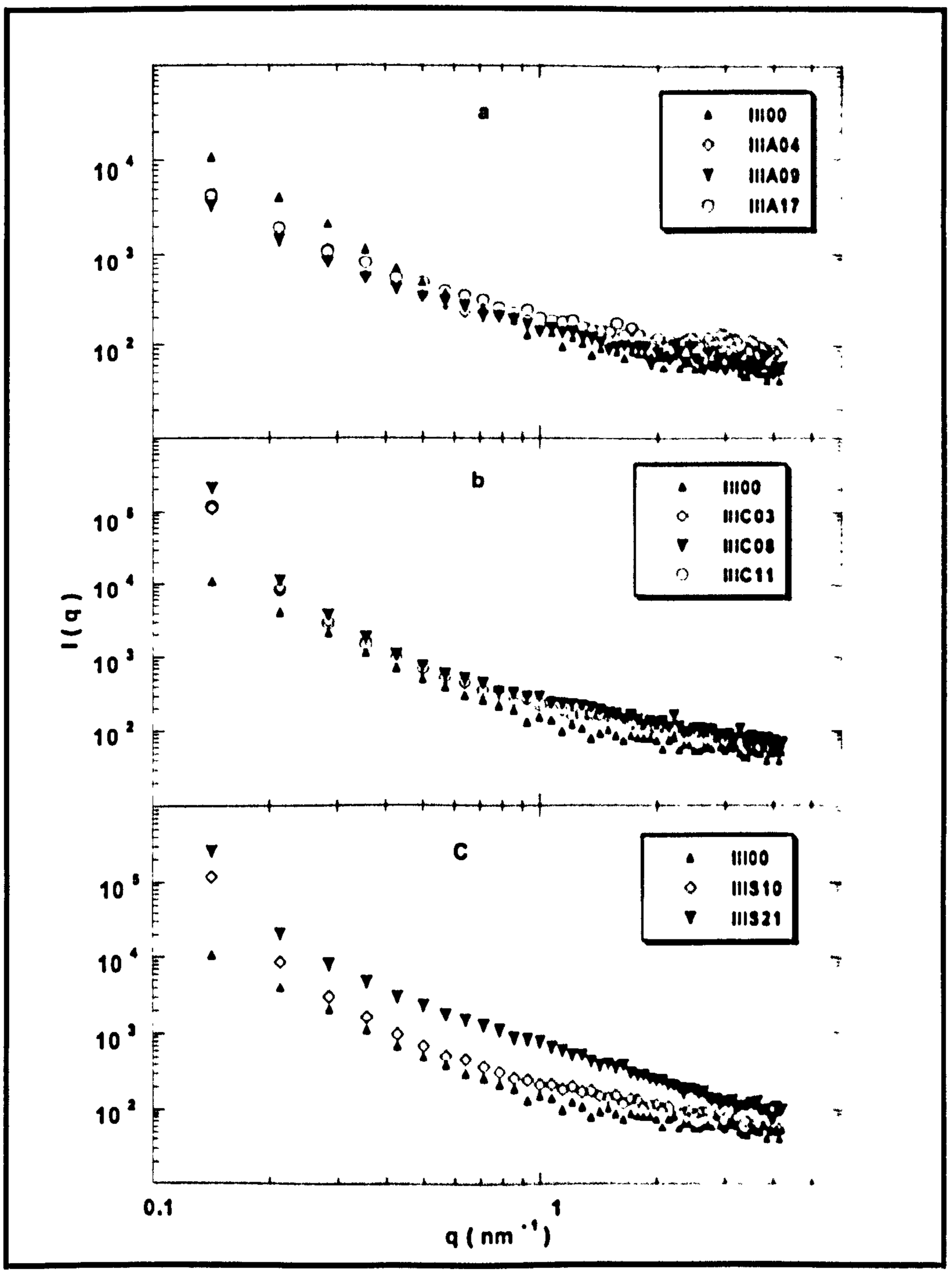

Figure 6.8: SAXS log-log plots for activated Illinois coal chars with: a) air at 673K, b) carbon dioxide at 1173K, c) steam at 1173K.

After this qualitative information from SAXS curves; it is necessary to obtain some quantitative approaches. According to Equation 2.54, the I(q) can be directly related to the total interfacial area, usual named as Porod Invariant (*Q*). For the aim of this work is important found *Q* from SAXS however dependence of q^{-4} over a large range of q was not found for any sample; then is not possible formally to calculate Porod scattering

invariants. Nevertheless values of $\int I(q)q^2dq$ were evaluated in order to get a comparative indication of interfacial area. *Q* values are showed in Table 6.3. *Q* value increased consequently with burn-off for Pittsburgh char gasification, which indicates development of meso and microporous; the exception was steam activation, because *Q* value for PitS11 decreased compared to PitS09. Illinois gasification showed that *Q* values (SAXS) have not clear tendency with burn-off.

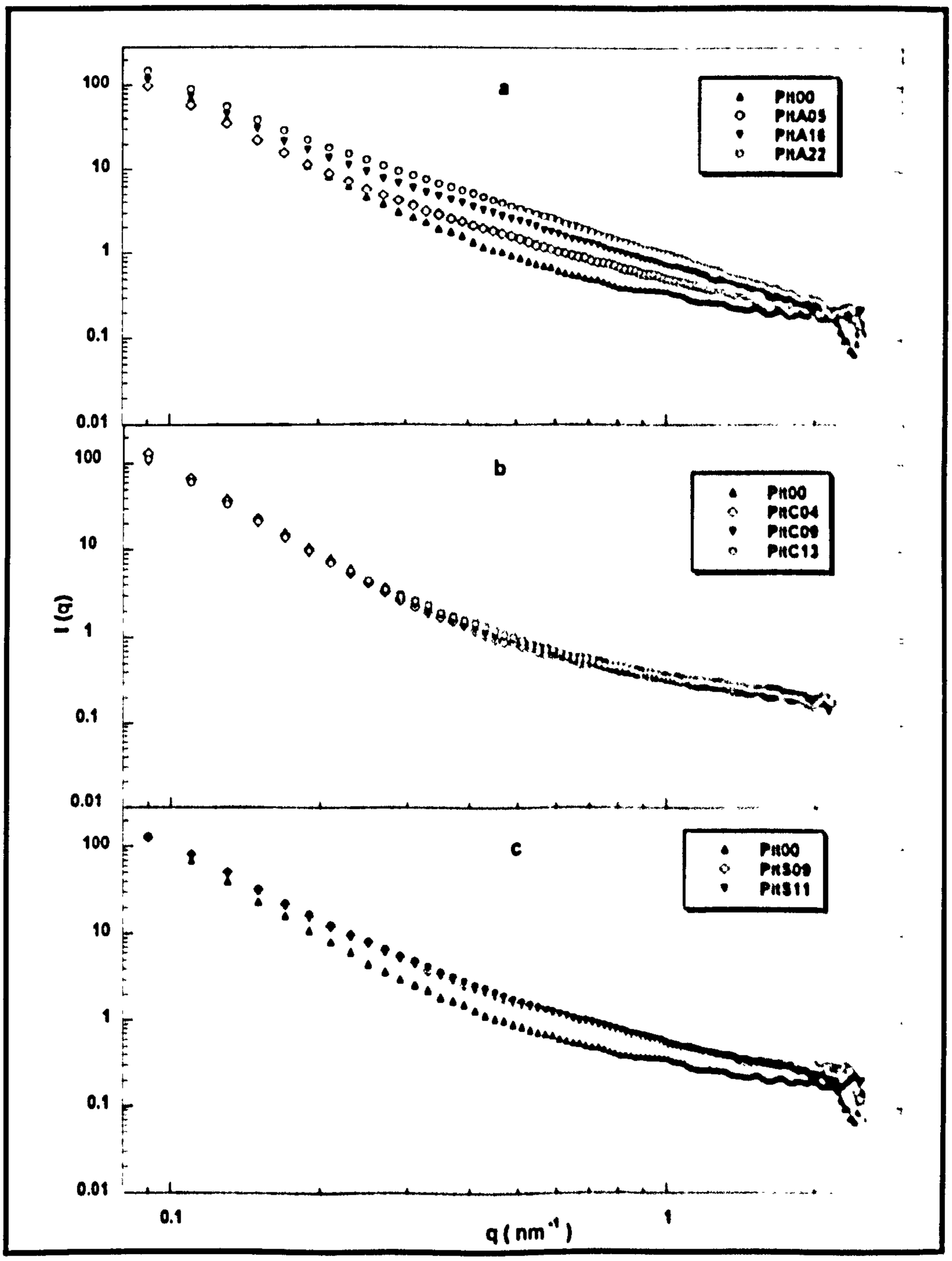

Figure 6.9: SANS log-log plot for activated Pittsburgh coal chars with: a) air at 673K, b) carbon dioxide at 1173K, c) steam at 1173K.

Another parameter than can be useful for porosity characterisation is the radius of gyration scattering object; Rg (Equation 2.51), this is a measure of the scatterer size. Rg parameter was calculated from the slope of the linear region at high q in a Guinier plot. Radius of gyration is listed in Table 6.4. As reference, if a sphere form is assumed to the scattering object, the diameter (d) is calculated using Equation 2.52. The linear plot region was obtained over a short range of q, and then Guinier law cannot be strictly applied. However it is noted that Rg increased with activation which indicates that there was a widening process of the pore size.

Table 6.3: Characterisation by SAS of Pittsburgh and Illinois coal chars; activated with air, carbon dioxide and steam, using Porod law and Guinier approaches

Coal Char	SAXS			SANS
	Rg (nm)	*d* (nm)	PI (a.u.)	PI x 10^3 (a.u.)
Gasified Pittsburgh chars				
Pit00	0.36	0.93	2546	1127
PitA05	0.51	1.32	4860	1470
PitA16	0.52	1.34	5681	1503
PitA22	0.54	1.39	6447	1989
PitC04	0.44	1.14	3783	1275
PitC09	0.46	1.19	4432	1213
PitC13	0.44	1.14	5339	1257
PitS09	0.49	1.26	5191	1847
PitS11	0.48	1.24	5007	1736
Gasified Illonois chars				
Ill00	0.35	0.90	1576	1429
IllA04	0.21	0.54	2579	1239
IllA09	0.37	0.96	1682	1392
IllA17	0.37	0.96	2294	1359
IllC03	0.29	0.75	2239	1023
IllC08	0.45	1.16	2791	986
IllC11	0.43	1.11	2511	1456
IllS10	0.49	1.27	2823	2002
IllS21	0.54	1.39	4465	1168

A paper [152] reported a fractal surface in chars from SAXS data using Equation 2.58. In this work was found that is not possible to assume a

$q^{-(6-D)}$ decay of the scattering intensity I(q), therefore scattering curves by SAXS for the coal chars studied does not represent a fractal surface; which agree with similar conclusion in reference 141 (p. 188).

Log-log plots from SANS data are showed in Figure 6.9 and 6.10 for Pittsburgh and Illinois chars, respectively. SANS analysis to air and steam gasification on Pittsburgh char permits to infer similar information than SAXS. However, in this analysis air activation showed clearly an increase in the scattering intensity as burn-off increase; SAXS and SANS profiles to steam gasified chars seem like similar. The SANS curves to activate chars in carbon dioxide showed the same profile than unactivated char. SANS plots, corresponding to Illinois chars, nearly have similar analysis than SAXS. In both set of chars, the SANS considerations were supported by the Q values, or interfacial area formed (see Table 6.4).

This work bases the analysis by SAS techniques on the phenomenon of diffraction by microscopic inhomogeneities present within chars, therefore the I(q) depends upon the square of the contrast factor between that inhomogeneities and its surrounding carbonaceous matrix. The interpretations gave in this work to SAS data were considered that all the scattering intensity is from pores within the carbon matrix; however, mineral matter inclusions can be contribute to the total SAS intensity. For Pittsburgh chars the ash content was varied between 14 and 19%, and for Illinois chars the ash content ranged between 25 and 32%, (see Table 6.1). Also, Table 4.3 shows that in the original mineral matter of these coals there are high contribution of silicon, aluminium, iron and calcium.

Scattering electron and length density values for the mineral contained in Pittsburgh and Illinois are respectively; to quartz: 1.32 and 0.70 to Kaolinite: 1.31 and 0.054, to anhydrite: 1.48 and 0.064, to calcite 1.35 and 0.079, and to pyrite: 2.44 and 0.65 (expressed in $molcm^{-2}x10^{10}$). In previous work [231] was reported the contrast factors for SAS for a number of coals with combination of pore or minerals. In the case for low rank

coals; both SAXS and SANS, the $C_{i,j}$ factors for pores and minerals were close. Therefore, this effect must be kept in mine, and it is recommended by this work to run SAS experiments in demineralised coal chars.

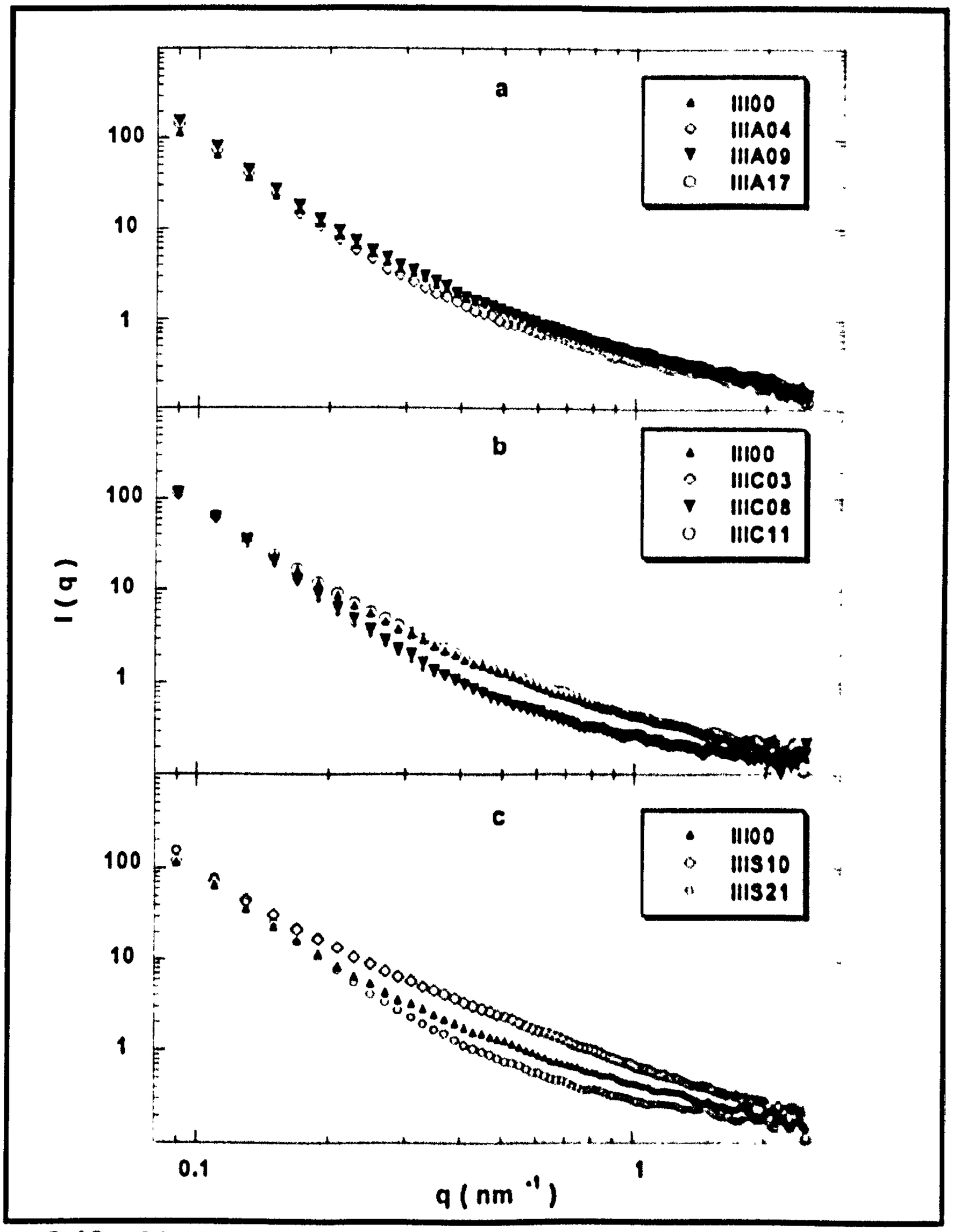

Figure 6.10: SANS log-log plot for activated Illinois coal chars with: a) air at 673K, b) carbon dioxide at 1173K, c) steam at 1173K.

6.4 Positron Annihilation Life-time Characterisation (PALS)

In the Section 2.4, it was settled that positron life-times in carbons can be attributed to annihilation of positrons in the bulk (~200 ps), on the surface (~400 ps), and by formation of a bound par (e^-e^+) called o-Ps which finally will be annihilated after 1000 ps [52,59,60]. In this research, positron annihilation life-time spectra obtained for coal chars were statistical best fitted as the sum of two components, however one and three components were tested using PATFIT program.

Table 6.4: Positron annihilation life-times and intensities for the activated coal chars.

CHAR	τ_1 (ps)	I_1 (%)	τ_2 (ps)	I_2 (%)	τ_M (ps)
Gasified Pittsburg coal chars					
Pit00	368	98.7	1120	1.3	378
PitA05	362	97.6	902	2.4	375
PitA16	367	97.6	963	2.4	381
PitA22	366	98.0	1088	2.0	380
PitC04	363	98.8	1405	1.2	376
PitC09	365	98.3	1073	1.7	377
PitC13	364	98.7	1196	1.3	375
PitS09	360	98.6	1126	1.4	371
PitS11	360	99.0	1382	1.0	371
Gasified Illinois coal chars					
III00	354	96.5	853	3.6	372
IIIA04	353	95.6	775	4.3	371
IIIA09	365	98.7	1171	1.3	376
IIIA17	354	95.8	841	4.2	375
IIIC03	366	98.9	853	1.1	377
IIIC08	357	97.5	1294	2.5	369
IIIC11	354	97.4	840	2.6	369
IIIS10	352	96.1	754	3.9	368
IIIS21	358	96.3	777	3.7	373

Table 6.4 shows the results of the life-times and intensities obtained. The mean time, τ_M, was proposed as a widespread form to analyse the positron annihilation spectrum and it was defined by Equation 2.74 for two

lifetime components. In this case τ_M shows a similar tendency than short-lived time, and then τ_M will be not considered beyond.

The annihilation experiments showed that the variation of the intensity is controlled mainly by the change by the short-lived component; which has been assigned to be the positron annihilation on graphitic surfaces and in the interfaces between crystals [193-196]. Consequently in chars, the intensity of this component can be assigned to changes in the basic carbon macrostructure, initially formed after the pyrolysis (i.e. lamellas type graphene cross-linked).

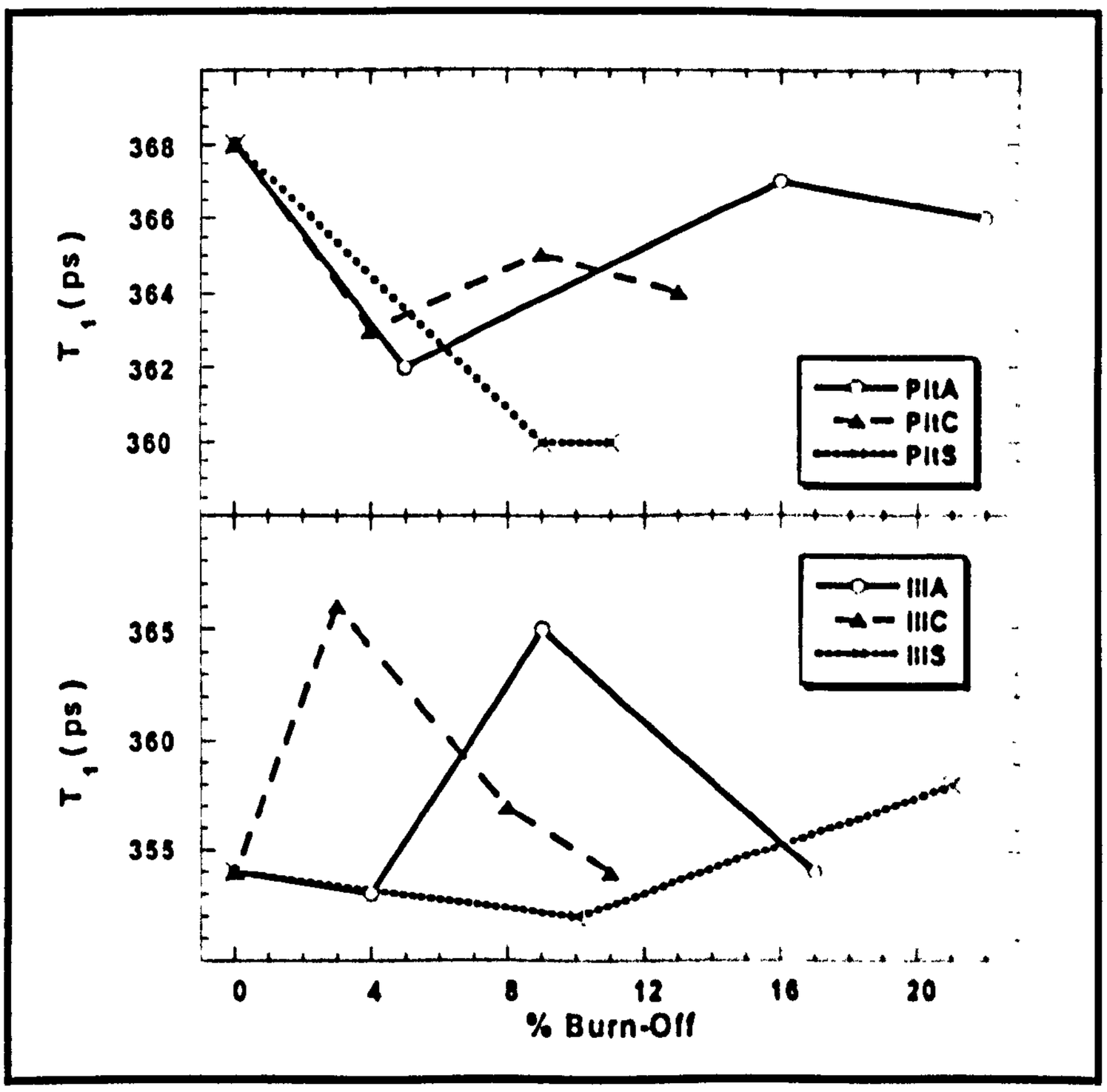

Figure 6.11: Shortest positron annihilation lifetime values for the air, carbon dioxide and steam gasification of Pittsburgh coal chars (up) and Illinois coal chars (down).

In general terms, despite that coal chars studied have not significantly change in the main positron life time annihilation, this value was low for Pittsburgh activated chars compared than unactivated char. In the case of Illinois activated chars, the annihilation time was high than unactivated

char (Figure 6.11). Therefore, and assuming that τ_1 senses the porosity developed with gasification, it seem that Illinois char was gasified by a pore widening mechanism. Opposite to that Pittsburgh char apparently generated new porosity. Also, it is showed that the pore size formed during Illinois gasification was narrow than Pittsburgh gasification. Hence, it is found a coincide information from PALS with adsorption analysis.

Other relevant fact, it is that during Illinois char gasification the decovolution of PAL spectra gave a second life time ranging between 754 and 1294 ps, which showed significantly intensity value, the majority of τ_2 value were below than 1000 ps, this means that the formation of o-positronium strictly can not inferred. But, development of narrow bimodal pore size could be proposed. Further modifications to the PATFIT program must be introduced to confirm this last appreciation.

6.5 Correlation of the Characterisation by Positron Annihilation Life-time Spectroscopy with Gas Adsorption and Small Angle Scattering

Figure 6.12 shows the correlation between the surface area (N_2-BET), microsurface area (CO_2-DR), and Porod scattering invariants (from SAS) for Pittsburgh coal chars. It can be seen that there is a similar tendency of the internal surface area obtained by gas adsorption and Q_{SAXS}.

All of them increase according to the burn-off, with exception of the carbon dioxide reaction, which showed few changes in surface area measured within nitrogen. On the other hand, Q_{SANS} values can see to be a constant and not significant changes are showed.

Rg values obtained from SAXS; which can be associated to the size of the scattering object showed an increase at low burn-off, and then remains

constant. The lifetime corresponding to the annihilation positron at the same low degree of burn-off decrease and then remains constant. It can be correlated, according to the positron trapping theory, so the increasing in the pore pore size delays the annihilation time. Therefore, Rg from SAXS and τ_1 from PALS can be assumed in agreement (see Figure 6.13).

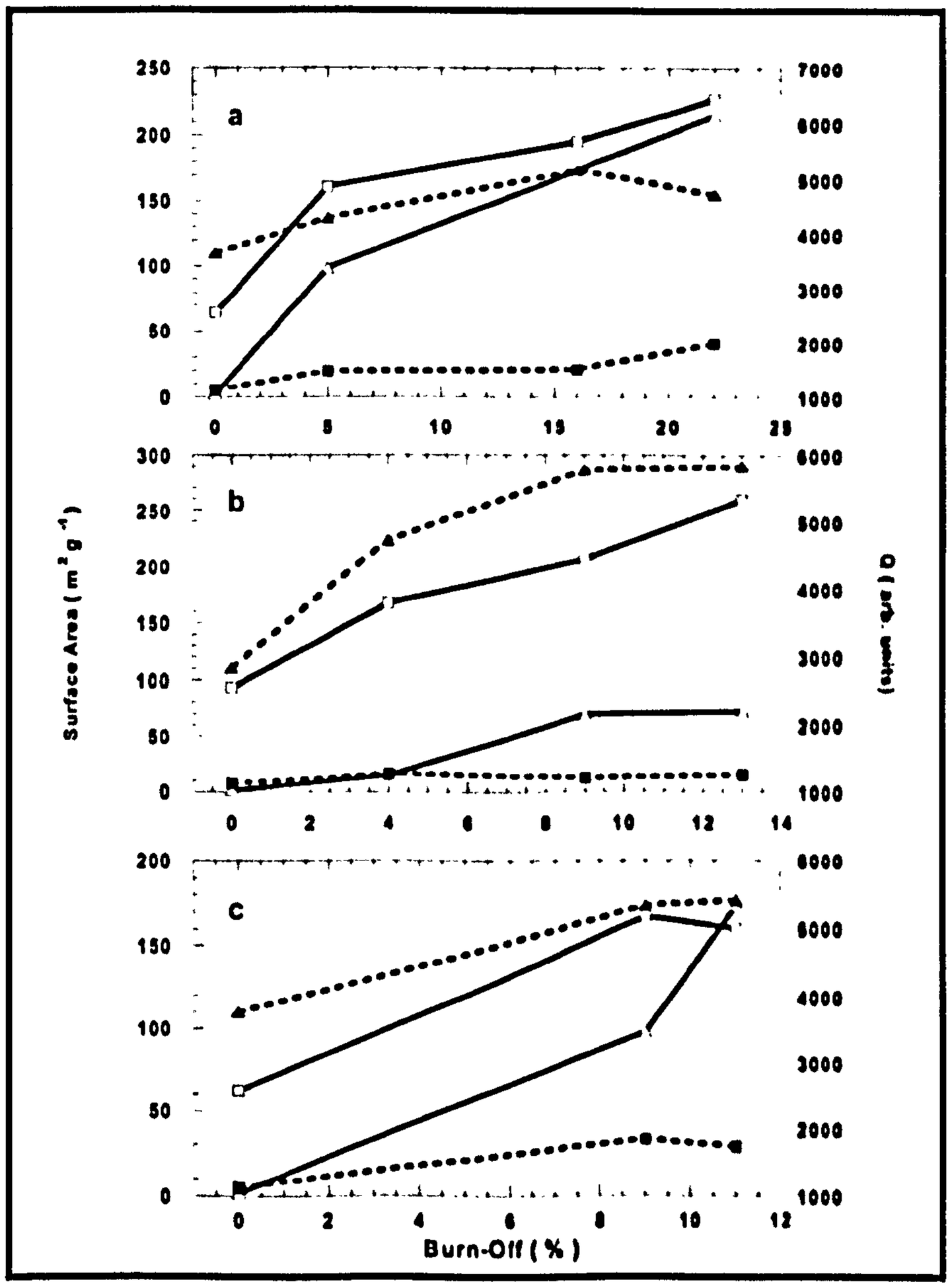

Figure 6.12: The correlation between the surface area by nitrogen adsorption (white triangles), micro surface area by CO_2 adsorption (black triangles), Porod scattering invariants by SAXS (white squares), Porod scattering invariants by SANS (black squares), for gasified Pittsburgh coal chars: a) Air, b) Carbon dioxide, c) Steam.

Figure 6.14 showed an agreement between the porod invariant from both SAXS and SANS, and surface area obtained by gas adsorption to Illinois gasified chars, with exception of IllA09. It can be deduced that the internal

surface area increase with burn-off, in particular to steam activation. However, CO_2 adsorption on Illinois gasified chars showed highest microsurface area values than Pittsburgh gasified chars. Thus, microporosity can be developed to Illinois char.

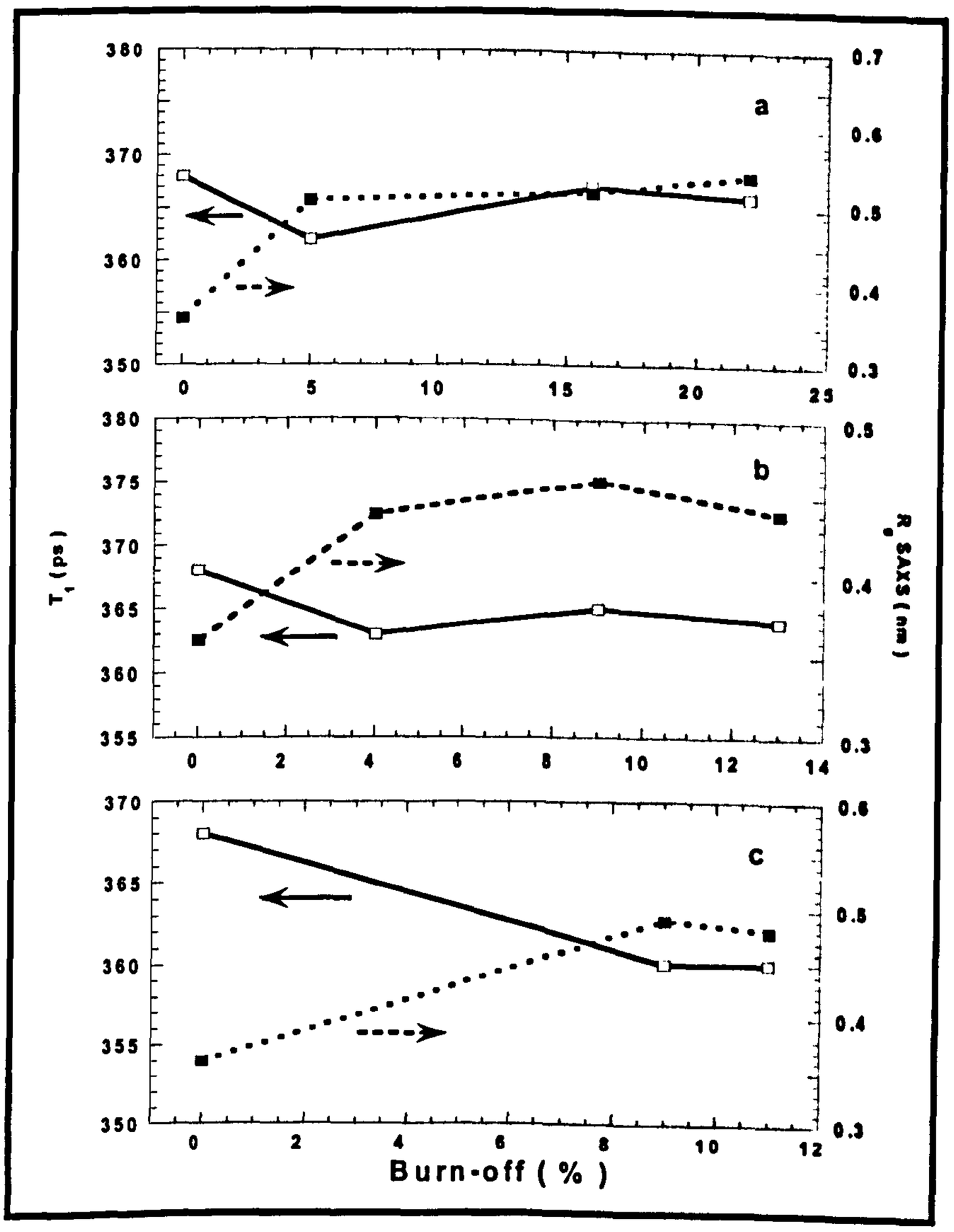

Figure 6.13: Comparison between the short positron annihilation lifetime (black squares) and the redii of gyration calculated from SAXS data (white squares), for gasified Pittsburgh coal chars: a) Air, b) Carbon dioxide, c) Steam.

Illinois activated chars have not a similar tendency in the annihilation positron lifetime therefore it is no possible to assume any correlation between positron life time and pore size; in Figure 6.15, τ_1 is compared to Rg from SAXS.

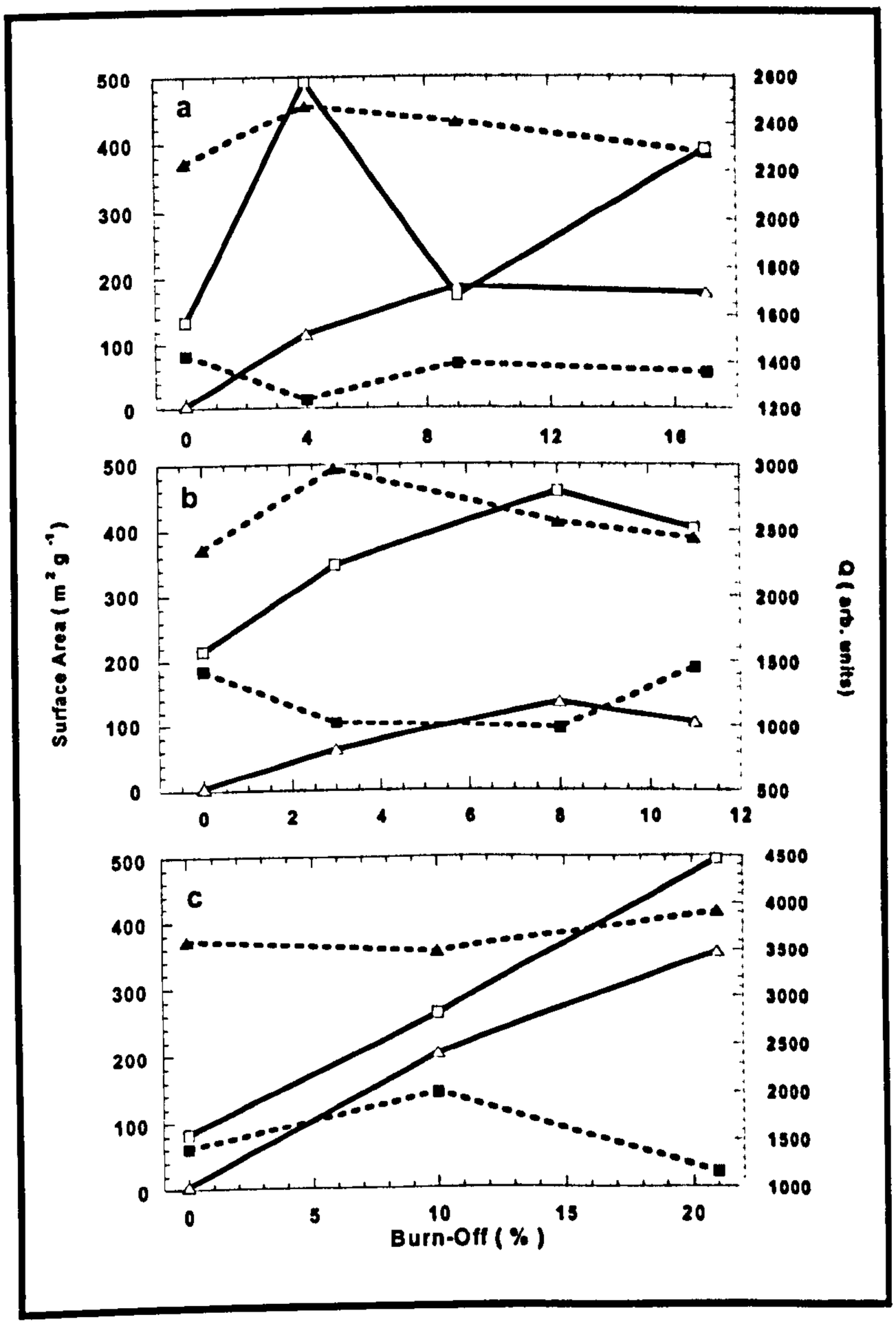

Figure 6.14: The correlation between the surface area by nitrogen adsorption (white triangles), micro surface area by CO_2 adsorption (black triangles), Porod scattering invariants by SAXS (white squares), Porod scattering invariants by SANS (black squares), for gasified Illinois coal chars: a) Air, b) Carbon dioxide, c) Steam.

The overall analyses of gasified chars showed develop of porosity for both series; Pittsburgh and Illinois coal gasification that can be deduced by the gas adsorption analysis and SAXS. SANS experiments showed low sensitive to follow the pore evolution in the gasification of the coal chars; which would attribute to the contribution of mineral matter to the neutron SAS intensity.

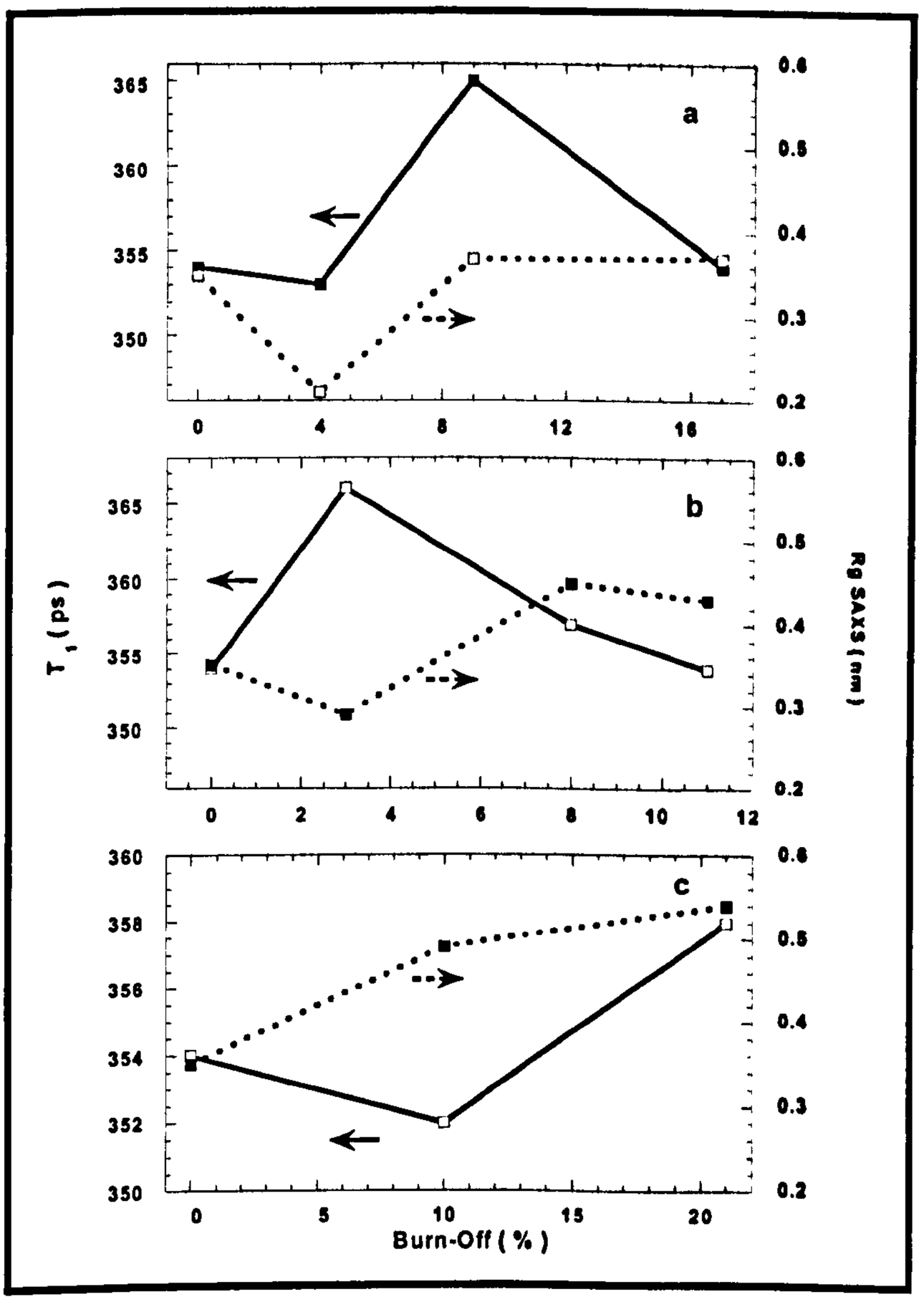

Figure 6.15: Comparison between the short positron annihilation lifetime (black squares) and the radii of gyration calculated from SAXS data (white squares), for gasified Illinois coal chars: a) Air, b) Carbon dioxide, c) Steam.

According to the adsorbed volume of CO_2 and N_2, the activated chars seem to be a mix of meso and micro porous adsorbents with molecular sieve properties. In the case of Illinois chars the tendency is to favour the formation of microporosity. Therefore for this kind of materials the information of gas adsorption can be influenced either by activate adsorption of molecules like CO_2 and N_2 into of ultramicroporosity also by the presence of close porosity, due to that the information can be unrealistic. The other side, SAS and PALS techniques showed patterns could be influenced by contribution of the mineral matter content. Thus, Pittsburgh and Illinois chars had more than 14 percent of ash content , and

the results from SAS and PALS to these chars have not a clearly correlation with porosity. The analysis in this work was noted that "pure" carbons (i.e. without mineral matter), such as Saran polymer based chars and carbon fibers, showed a good correlation between pore size and Rg (SAS) and τ_1 (PALS). Further PALS and SAS studies on demineralised coal chars will be made.

7 CONCLUSIONS AND FUTURE WORK

PALS gave information of the electronic density inside of the pore structure which is not feasible to obtain by the other accepted adsorption techniques used in this work. These data are complementary information to gas adsorption and small angle scattering techniques. The main positron lifetime component (below of 400 ps), found in the studied porous carbons has been assigned to annihilation of positrons by interaction with the electron density at the surface and near-surface regions.

The carbons prepared for this study were free of minerals and essentially microporous, due to this the analysis was directly related to the behavior of pore evolution. In general, PAS seems to be useful technique to probe both ultramicroporosity (below of 0.7nm) and supermicroporosity (between 0.7 and 2 nm) without restriction to access the porosity or interactions between the probe and the bulk material, as happened in common characterisation by N_2 /CO_2 adsorption.

A good correlation has been found between PALS and gas adsorption technique. The results in pure carbons, (AC and ACF), show a direct relationship between main positron lifetime and pore size. On the other hand in activated coal chars a decrease in the positron lifetime value was observed compared to pure carbons. Apparently the annihilation mechanism can be influenced by the mineral matter content.

It was found that SAS modelling produces quantitative knowledge of the pore dimensions from the scattering intensity data, dealing with the contrast factor, ($C_{s,p}$). It was found that this parameter according to the electron density sensed using PALS was variable. This is important

information in the initial stage of the gasification process of carbonaceous materials.

The correlation between lifetime from PALS, mean pore measured by gas adsorption and SAS all show that at low burn-off level (below 15%), there is essentiality development of microporosity, when carbonaceous materials have been gasified with air or carbon dioxide. At high burn-level or when steam is used as activator, evolution of mesoporosity was detected by widening of pore size. This means that new microporosity was not created in these reactions. This result can change with the origin of the raw material. In the case of coal chars, development of microporosity can be promoted at very low burn-off level using carbon dioxide, while with the other oxidizing agents a mixture of micro and mesoporosity was obtained. This information permits to direct the application of the activated carbons; for example, to promote microporosity will be right to obtain an adsorbent material, to control a mix of meso and microporossity will be adequate to produce a molecular sieve material. In sense of these results both of these materials can be produced from coal chars.

As a result of this work, it is recommended to study by PALS the demineralised coal chars to determine the effect of inorganic components on the positron annihilation mechanism. Also it is recommended to evaluate the use of an in-situ PALS detector during gasification of carbonaceous materials, in order to monitor the evolution of porosity during the reaction. Currently, this is a feasible analysis only 600 °C, due to the thin metal cover used to encapsulate the radioactive source.

REFERENCES

1. Edwards, I. A. S. in: Introduction to Carbon Science, (Ed. H. Marsh), Butterworth, London, 1989, pp. 2-18

2. International Committee for Characterization and Terminology of Carbon (ICCTC), *Carbon*, 1982, 20, 445

3. International Committee for Characterization and Terminology of Carbon (ICCTC), *Carbon*, 1982, 23, 601

4. International Committee for Characterization and Terminology of Carbon (ICCTC), *Carbon*, 1982, 21, 517

5. van Krevelen, D.W., Coal, Elsevier, Amsterdam, 1961

6. Francis, W., and Peters,M.C., Fuels and Fuel Technology, Pergamon Press, Oxford, 1980

7. Crelling, J.C., in: Introduction to Carbon Science, (Ed. H. Marsh), Butterworth, London, 1989, pp. 259-284

8. Osborne, D.G., Coal-Preparation Technology, *Volume one*, Graham & Trotman, London, 1988

9. Gibson, J., in: Coal and Modern Coal Processing, Pitt, G.W., and Millward, G.R., eds., Academic Press, London, 1979

10. Gray, R.J., in: Introduction to Carbon Science, (Ed. H. Marsh), Butterworth, London, 1989, pp. 285-321

11. International Committee for Characterization and Terminology of Carbon (ICCTC), *Carbon*, 1982, 25, 317

12. Heming, K.-D., Degel, J., in: Meeting of European Rotogravure Association Engineers Group, Mulhouse, France, 20/21 March 1990, www.activated-carbon.com

13. Bansal, R. Ch., Donnet, J.B., Stoeckli, F., Active Carbon, Marcel Dekker, New York, 1988, pp. 1-26, 335-460

14. Piccione, S., Urbanic, J.E., *U.S. Patent* 3,244,572, Dec. 27, 1966

15. Zall, D.M., *U.S. Patent* 3,876,451, Apr. 8, 1975

16. Ajayan, P.M., *Chem. Rev.*, 1999, 99, 1787

17. Bandow, S., Asaka, S., Saito, Y., Rao, A.M., Grigorian, L., Richter, E., Eklund, P.C., *Phys. Rev. Lett.*, 1998, **80**, 3779

18. Fan, Y.Y., liao, B., Liu, M., Wei., Y.L., Lu, M.Q., Cheng, H.M., **Carbon**, 1999, **37**, 1649

19. Dillon, A.C., Jones, K.M., Bekkedahl, T.A., Kiang, C.H., Bethune, D.S., *Nature*, 1997, **386**, 377

20. Smith, W.R., Polley, M.H., *J. Phys. Chem.*, 1956, **60**, 689

21. Board, J.A., In: Proc. 2nd Conf. on Ind. Carbon and Graphite, S.C.I, London, 1966, pp. 277-289

22. Marsh, H., Taylor, D.A., Lander, J.R., *Carbon*, 1981, **19**, 375

23. Marsh, H., Menendez, R., In: Introduction to Carbon Science, (Ed. H. Marsh), Butterworth, London, 1989, pp. 37-73

24. Evans, M., Marsh, H., in: Characterisation of Porous Solids, (Eds. S.J. Gregg, K.S.W. Sing, H.F. Stoekli), S.C.I., London, 1979, pp. 53-65

25. Muños-Guillena, M.J., Illan-Gomez, M.J., Martin-Martinez, J.M., Linaros-Solano, A., Salinas-Martinez de Lecea, C., *Energy & Fuels*, 1992, **6**, 9

26. Balek, V., Koranyi, A., *Fuel*, 1990, **69**, 1502

27. Siemieniewska, T., Tomkow, K., Kaczmarczyk, J., Albiniak, A., Broniek, E., Jankowska, A., Grillet, Y., Francois, M., In: Characterisation of Porous Solids III, (Eds. J. Rouquerol, F. Rodriguez-Reinoso, K.S.W. Sing, K.K. Unger), Elsevier, Amsterdam, 1994, pp. 695-704

28. Manster, K.J., McEnaney, B., In: Characterisation of Porous Solids, (Eds. S.J. Gregg, K.S.W. Sing, H.F. Stoekli), S.C.I., London, 1979, pp. 79-87

29. Nandi, S.P., Walker Jr., P.L., *Fuel*, 1975, **54**, 169

30. Chiche, P., Durif, S., Pregermain, S., *Fuel*, 1965, **44**, 5

31. Walker Jr., P.L., Foresti Jr., R.J., Wright, C.C., *Ind. Eng. Chem.*, 1953, **45**, 1703

32. van Heek, K.H., Muhlen, H.-J., *Fuel Process. Technol.*, 1987, **15**, 113

33. Lowenthal, C., Wanzl, W., van Heek, K.H., *Fuel*, 1986, **65**, 346

34. Muhlen, H.-J., van Heek, K.H, In: Porosity in Carbons: Characterization and Applications, (Ed. J.W. Patrick), Halsted Press, New York, 1994, pp. 131-149

35. Rodriguez-Reinoso, F., in: Fundamentals Issues in Control of Carbon Gasification Reactivity, (Eds. J. Lahaye, and P. Ehrburger), Kluwer Academic Publishers Amsterdam, 1991, pp. 533-571

36. Hurt, R.H., Sarofim, A.F., Longwell, J.P., *Energy & Fuels*, 1991, **5**, 290

37. Hurt, R.H., Sarofim, A.F., Longwell, J.P., *Fuel*, 1991, **70**, 1079

38. Berger, J., Siemieniewska, T., Tomkow, K., *Fuel*, 1976, **55**, 9

39. Adams, K.E., Glasson, D.R., Jayaweera, S.A.A., *Carbon*, 1989, **27**,95

40. Hoinkis, E., Robens, E., *Carbon*, 1989, **27**, 157

41. Tomkow, T., Siemieniewska, T., Czechowski, F., Jankowska, A., *Fuel*, 1977, **56**, 121

42. Rodriguez-Reinoso, F., Linares-Solano, A., Martin-Martinez, J.M., Lopez-Gonzales, J.D., *Carbon*, 1984, **22**, 123

43. Garrido, J., Linares-Solano, A., Martin-Martinez, J.M., Molina-Sabio, M., Rodriguez-Reinoso, F., Torregrosa, R., *J. Chem. Soc.: Faraday Transactions 1*, 1987, **3**, 1081

44. Parra, J.B., de Sousa, J.C., Pis, J.J., Pajares, J.A., Bansal, R.C., *Carbon*, 1995, **33**, 801

45. Kull, H., Kashani-Motlagh, M.M., Muhlen, H.-J., van Heek, K.H., *Fuel*, 1992, **71**, 879

46. Johnson, J.L., *Ame. Chem. Soc.: Div. Fuel Chem. Preprints*, 1975, **20 (4)**, 85

47. Bhatia, S.K., Perlmutter, D.D., *J. Ame. Inst. Chem. Eng.*, 1989, **26**, 379

48. Laine, N.R., Vastola, F.J., Walker Jr., P.L., *J. Phys. Chem.*, 1963, **63**, 2030

49. Radovic, L.R., Walker Jr., P.L., Jenkins, R.G., *Fuel*, 1983, **62**, 209

50. Radovic, L.R., *Carbon*, 1991, **29**, 809

51. McEnaney, B., in: Fundamentals Issues in Control of Carbon Gasification Reactivity, (Eds. J. Lahaye, P. Ehrburger), Kluwer Academic Publishers Amsterdam, 1991, pp. 175-203

52. Muhlen, H.-J., *Fuel Process. Technol.*, 1990, **24**, 285

53. Causton, P., McEnaney, B., *Fuel*, 1985, **65**, 292

54. Koranyi, de, A., *Carbon*, 1989, **27**, 55

55. van Heek, K.H., Muhlen, H.-J., *Fuel,* 1985, **64**, 1405

56. Walker, P.L., Rusinko, Jr. F. and Austin, L.G., In: Advances in Catalysis (Eds. D.D. Eley, P.W. Selwood, P.B. Weisz), Academic Press, New York,1959, Vol. XI, 133

57. Laurendeau, N.M., *Prog. Energy Combust. Sci.*, 1978, **4**, 221

58. Johnson, J.L., Kinetics of Coal Gasification, John Wiley & Sons, New York, 1979, pp. 1-178

59. Thomas, J.M., in: Chemistry and Physics of Carbon, (Eds. P. L. Walker, Jr and P.A. Thrower), Marcel Dekker, New York , 1965, Vol. 1, 121-196

60. Henning, in: Chemistry and Physics of Carbon, (Eds. P. L. Walker, Jr and P. A. Thrower), Marcel Dekker, New York, 1966, Vol. 2, pp. 1-49

61. Ergun, S., Mentser, M., in: Chemistry and Physics of Carbon, (Eds. P. L. Walker, Jr and P. A. Thrower), Marcel Dekker, New York, 1965, Vol. 1, pp. 203-263

62. Stein, S.E., Brown, R.L., *Carbon*, 1985, **23**, 105

63. Rodriguez-Reinoso, F., Thorwer, P.A., Walker Jr., P.L., *Carbon*, 1974, **12**, 63

64. Blackwood, J.D., McTaggart, F.K., *Aust. J. Chem.*, **12**, 533

65. Garten, V. A. and Weiss, D. E., *Aust. J. Chem*, **10**, 309

66. Walker Jr., P.L., in: Chemistry and Physics of Carbon, (Eds. P. L. Walker, Jr), Marcel Dekker, New York, 1968, Vol. 4, pp. 287-383

67. Hippo, E., Walker, Jr., P.L., *Fuel*, 1975, **54**, 245

68. Tomita, A., Mahajan, O.P., Walker, Jr., P.L., 1977, *Ame. Chem. Soc.: Div. Fuel Chem. Preprints*, **22(1)**, 4

69. Mondragon, F. and Molina, A., *Fuel*, 1999, **78**, 1831

70. Schilling, H-D., Bonn, B. and Krauss, U., Coal Gasification, Graham & Trotman, London, 1981, pp. 10-32

71. Smith, R. N., Lesnini, D. and Mooi, J., *J. Phys. Chem.*, 1957, **61**, 81

72. Bedjai, G., Orbach, N. N. and Riesenfeld, F.C., *Ind. Eng. Chem.*, **50**, 1165

73. Madley, D.G. and Strickland-Constable, R.F., *Trans. Faraday Soc.* , **49**, 1953, 1312

74. Watts, H., *Trans. Faraday Soc.*, **54**, 1958, 93

75. Marsh, H. and Kuo, K., in: Introduction to Carbon Science, (Ed. H. Marsh), Butterworth, London, 1989, pp. 107-151

76. von Fredersdorff, C.G., Elliott, M.A., in: Chemistry of Coal Utilization, supplementary volume, (Ed. H.H. Lowry), John Willey and Sons, New York-London, 1963, p.892

77. Phillips, S.R., Vastola, F.J., Walker Jr. P.L., *Carbon*, 1970, **8**, 197

78. Arthur, J., *Trans. Faraday Soc.*, 1956, **47**, 164

79. Ahmed, S., Back, M.H., *Carbon*,1985, **23**, 513

80. Phillips, S.R., Vastola, F.J., Walker Jr., P.L., *Carbon*, 1969, **7**, 479

81. Walker Jr., P.L., Taylor, R.L., Ranish, J.M., *Carbon*, 1991, **29**, 411

82. Thomas, J.M., *Carbon*, 1970, **8**, 413

83. Reif, A.E., *J. phys. Chem.*, 1952, **56**, 785

84. Salatino, P., Senneca, O., Masi, S., *Carbon*, 1998, **36**, 443

85. Barton, S.S., Harrison, B.H., *Carbon*, 1975, **13**, 283

86. Koing, P.C., Squires, R.G., Laurenfeau, N.M., *Carbon*, 1985, **23**,531

87. Meijer, R., Weeda, M., Kapteijn, F., Moulijn, J.A., *Carbon*, 1991, **29**, 929

88. Li, S., Cheng, Y., *Fuel*, 1995, **74**,456

89. Huttinger, K.J., Nattermann, C., *Fuel*, 1994, **73**, 1682

90. Juntgen, H., *Carbon*, 1981, **19**, 167

91. Ohtsuka, Y., Asami, K., *Energy & Fuels*, 1995, **9**, 1038

92. Liu, Z-l., Zhu, H-h., *Fuel*, 1986, **65**, 1334

93. Ginter, D.M., Somorjai, G.A., Heinemann, H., *Energy & Fuels*, 1993, **7**, 393

94. Takarada, T., Tamai, Y., Tomita, A., *Fuel*, 1985, **64**, 1438

95. Everett, D.H., in: Characterisation of Porous Solids, (Eds. K.K. Unger , J. Rouquerol, K.S.W. Sing, H.Kral), Elsevier, Amsterdam, 1988, pp. 1-22

96. Sing, K.S.W., in: Characterisation of Porous Solids II, (Eds. F. Rodriguez-Reinoso, J. Rouquerol, K.S.W. Sing, K.K. Unger), Elsevier, Amsterdam, 1991, pp. 1-9

97. Rouquerol, J., Avnir, D., Everett, D.H., Fairbridge,C., Haynes,M., Pernicone,N., Ramsay, J.D.F., Sing, K.S.W., Unger, K.K., *Pure and Appl. Chem.*, 1994, **66**, 1740

98. Byrne, J.F., Marsh, H., in: Porosity in Carbons: Characterization and Applications, (Ed. J.W. Patrick), Halsted Press, New York, 1994, pp. 2-48

99. Sing, K.S.W., Everett, D.H., Haul, L., Moscou, R.A., Pierotti, J., Rouquerol, J., Siemienewska, T., *Pure and Appl. Chem.*, 1985, **57**, 603

100. McEnaney, B., Mays, T.J., in: Introduction to Carbon Science, (Ed. H. Marsh), Butterworth, London, 1989, pp. 153-196

101. Smith, K.L., Smoot, L.D., Fletcher, T.H., in: Fundamentals of Coal Combustion: For clean and efficient use, (Ed. L.D. Smoot), Elsevier, Amsterdam, 1993, pp. 433-506

102. Wells, W., Smoot, L.D., *Fuel*, 1991, **70**, 454

103. Jeroniec, M., *Surface Sci. Reports*, 1986, **6**, 65

104. Bansal, R. Ch., Donnet, J.B., and Stoeckli, F., in : Active Carbon, Marcel Dekker, New York, 1988, pp. 119-162, 335-460

105. Sing, K.S.W., *Carbon*, 1989, **27**, 5

106. Rodriguez-Reinoso, F., Garrido, J., Martin-Martinez, J.M., Molina-Sabio, M., Torregrosa, R., *Carbon*, 1989, **27**, 23

107. Parkyns, N.D., Quinn, D.F., in: Porosity in Carbons: Characterization and Applications, (Ed. J.W. Patrick), Halsted Press, New York, 1994, pp. 291-325

108. Menon, V.C., Komarneni, S., *J. Porous Materials*, 1998, **5**, 43

109. Quinn, D.F., Macdonald, J.A., *Carbon*, 1992, **30**, 399

110. Macdonald, J.A., Quinn, D.F., *J. Porous Materials*, 1995, **1**, 43

111. Mondragon, F., Quintero, G., Jaramillo, A., Fernandez, J., Calo, J.M., and Hall, P.J., *J. Mater. Sci.*, 1997, **32**, 1455

112. Lowell, S., Shields, J.E., Powder Surface Area and Porosity, Chapman & Hall, London, 1984

113. Rouquerol F., Rouquerol J., Sing, K., Adsorption by Powders & Porous Solids, Academic Press, London, 1999

114. Dubinin, M.M., *J. Colloid Interface Sci.*, 1967, **23**, 487

115. Pierce, C., *J. Phys. Chem.*, 1959, **63**, 1076

116. Wood, G.O.., *Carbon,* 2001, **39**, 343

117. Bering, B.P., Dubinin, M.M., Serpinsky, V.V., *J. Colloid Interface Sci.*, 1966, **21**, 378

118. Dubinin, M.M., in: Progress in Surface and Membrane Science, (Eds. D.A. Cadenhead, J.F. Danielli, M.D. Rosenberg), Academic Press, New York, 1975, pp. 1-72

119. Marsh, H., Rand, B., *J. Colloid Interface Sci.*, 1970, **33**, 101

120. Marsh, H., *Carbon*, 1987, **25**, 49

121. McEnaney, B., *Carbon*, 1987, **25**, 69

122. Dubinin, M.M., Serpinsky, V.V., *Carbon*, 1981, **19**, 402

123. Dubinin, M.M., Astakhov, V.A., *Advances in Chemistry Series*, 1971, **102**, 69

124. Stoeckli, H.F., Kraehenbuehl, F., Ballerini, L., De Bernardini, S., *Carbon,* 1989, **27**, 125

125. Sing, K.S.W., in: Porosity in Carbons: Characterization and Applications, (Ed. J.W. Patrick), Halsted Press, New York, 1994, pp. 49-66

126. Stoeckli, H.F., *J. Colloid Interface Sci.*, 1977, **59**, 184

127. Hubert, U., Stoeckli, F., Houriet, J-P, *J. Colloid Interface Sci.*, 1978, **67**, 195

128. Carrasco-Marin, F., Alvarez-Merino, M.A., Moreno-Castilla, C., *Fuel*, 1996, **75**, 966

129. Rouquerol F., Rouquerol J., Sing, K., Adsorption by Powders & Porous Solids, Academic Press, London, 1999, pp. 199-202

130. Lozano-Castelló, D., Cazorla-Amorós, D., Linares-Solano, A., *Carbon,* 2004, **42**, 1233

131. Jaroniec, M., Lu, X., Madey, R., Choma, J., and Klinik, J., *Fuel*, 1990, **69**, 516

132. Gregg, S.J., Sing, K.S.W., Adsorption, Surface Area and Porosity, Academic Press, London, 1982, p. 228, 230

133. Sing, K.S.W., *Carbon*, 1989, **27**, 5

134. Stoeckli, H.F., Ballerini, L., *Fuel,* 1991, **70**, 557

135. Dubinin, M.M., Stoeckli, H.F., *J. Colloid Interface Sci.*, 1980, **75**, 34

136. Dubinin, M.M., *Carbon*, 1985, **23**, 373

137. Barton, S.S., Evans, M.Y.B., Harrison, B.H., *J. Colloid Interface Sci.*, 1974, **40**, 462

138. McEnaney, B., *Carbon*, 1988, **26**, 267

139. Kadlec, O., in: Characterisation of Porous Solids II, (Eds. F. Rodriguez-Reinoso, J. Rouquerol, K.S.W. Sing, K.K. Unger), Elsevier, Amsterdam, 1991, pp. 759

140. Jaroniec, M., Choma, J., *Colloids and Surfaces*, 1989, **37**, 183

141. Hoinkis, E., in: Chemistry and Physics of Carbon, (Ed. P. A. Thrower), Marcel Dekker, New York, 1997, pp. 71-241

142. Kratky, O., in : Small Angle X-ray Scattering, (Eds. O. Glatter, O. Kratky), Academic Press, London, 1982, pp. 3-13

143. Windsor, C.G., *J. Appl. Cryst.*, 1988, **21**, 582

144. Peter, F., in : Introduction to neutron scattering - 1st European Conference on Neutron Scattering (ECNS'96), (Ed. A. Furrer),Paul Scherrer Institut, Villigen, 1996, pp. 162-174

145. Scherm, R., in : Introduction to neutron scattering - 1st European Conference on Neutron Scattering (ECNS'96), Furrer, A., ed.,1996, Paul Scherrer Institut, Villigen, pp. 9-32

146. Porod, G., in : Small Angle X-ray, (Eds. O. Glatter, O. Kratky),Academic Press, London, 1982, pp. 17-51

147. Schmidt, P. W., *J. Appl. Cryst.*, 1991, **24**, 414

148. North, A.N., in: Neutron and X-ray Scattering: Complementary Techniques (Eds. M.C. Fairbanks, A.N. North, N.J. Newport), The Institute of Physics, New York, 1990, pp. 181-196

149. Ciccarello, S., *J. Appl. Cryst.*, 1988, **21**, 117

150. Martin, J.E., Hurd, A.J., *J. Appl. Cryst.*, 1987, **20**, 61

151. Hurd, A.J., Schaefer, D.W., Smith, D.M., Ross, S.B., LeMehate, A., Spooner, S., *Phys. Rev, B,* 1989, **39**, 9742

152. Reich, M.H., Russo, S.P., Snook, I.K., Wagenfeld, H.K., *J. Colloid Interface Sci.*, 1990, **135**, 353

153. Avnir, D., Pfifer, P., Farin, D., *Nature*, 1984, **308**, 261

154. Ramsay, J.D.F., *Chem. Soc. Rev.*, 1986, **15**, 335

155. Beelen, T.P.M., Dokter, W.H., Van Garderen, H.F., Van Santen, R.A., Pantos, E., *Journal De Physique IV*, 1993, **3**, 393

156. Bale, H.D., Smith, P.W., *Phys. Rev. Lett.*, 1984, **53**, 596

157. Foster, M. D., Jensen,K. F., *Carbon*, 1991, **29**, 271

158. Foster, M. D., Jensen, K. F., *J.Colloid Interface Sci.*,1990,**135**,132

159. Gethner, J. S., *J. Appl. Phys.*, 1986, **59**, 1068

160. Sheu, E.Y., *Physical Review A*, 1992, **45**, 2428

161. Calo, J.M., Hall, P.J., *Carbon.*, 2004, **42**, 1299

162. Bota, A., *J. Appl. Cryst.*, 1991, **24**, 635

163. Sousa, J. C., Torriani, I.L., Luengo, C.A., *J. Appl. Cryst.*, 1991, **24**,803

164. Dubinin, M.M., Plavnik, G.M., *Carbon* 1968, **6**, 183

165. Dubinin, M.M., Plavnik, G.M., Zaverina, E.D., *Carbon* 1964, **2**, 261

166. Janosi, A., Stoeckli, H.F., *Carbon* 1979, **17**, 465

167. Kaneko, K., Suzuki, T., Fujiwara, Y., Nishikawa, K., in: Characterisation of Porous Solids II, (Eds. F. Rodriguez-Reinoso, J. Rouquerol, K.S.W. Sing, K.K. Unger), Elsevier, Amsterdam, 1991, pp. 389-398

168. Kaneko, K., Sato, M., Suzuki, T., Fujiwara, Y., Nishikawa, K., Jaroniec, M., *J.C.S. Faraday Trans.*, 1991, **87**, 179

169. McEnaney, B., Mays, T.J., Causton, P.D., *Langmuir*, 1987, **3**, 695

170. Gupta, A., Harrison, I.A., *Carbon*, 1994, **32**, 953

171. Hall, P.J., Ruiz, W., Gascon, D., Barrientos, E.L., Sherrington, D.C., *J. Chem. Soc. , Faraday Trans.*, 1996, **92**, 2607

172. Hall, P.J., , Gascon, D., Ruiz, W., Mondragon, F., Barrientos, E.L., Sherrington,D.C., Calo, J., *J. Chem. Soc. , Faraday Trans.*, 1997, **93**, 463

173. Antxustegi, M.M., Hall, P.J., Calo, J.M., *Energy and Fuels*, 1998, **12**, 542

174. Hautojarvi, P., Vehanen A., in: Positrons in Solids, Springer-Verlag, Berlin,1979, pp.1- 23

175. Schrader, D.M., Jean, Y.C., in : Positron and Positronium Chemistry, (Ed. Y.C. Jean), Elsevier, Amsterdam,1988, pp. 1-26

176. Green, J., Lee, J., Positronium Chemistry, Academic Press, New York, 1964

177. West, R.N., Positron Studies of Condensed Matter, Taylor & Francis, London, 1974

178. Brand, W., *Appl. Phys.*, 1974, **5**, 1

179. Brand, W., Berko, S., Walker, K.K., *Phys. Rev.*, 1960, **120**, 1289

180. Eldrup, M., *Ann. Chim. Fr.*, 1985, **10**, 681

181. Wang, S.J., Jean, Y.C., in : Positron and Positronium Chemistry, (Ed. Y.C. Jean), Elsevier, Amsterdam, 1988, pp. 255

182. Nakanishi, H., Jean, Y.C., in : Positron and Positronium Chemistry, (Ed. Y.C. Jean), Elsevier, Amsterdam, 1988, pp. 159

183. Pethrick, R.A., *Prog. Polym. Sci.*, 1997, **22**, 1

184. Eldrup, M., in: Industrial Applications of Positron Annihilation, Invited talk at, Europhysics, Industrial Workshop EIW-12, Oisterwijk, 1994

185. Jean, Y.C., Sandreczki, T.C., Ames, D.P., *J. Poly. Sci. B*, 1986, **24**, 1247

186. Venkateswaran, K., Cheng, K.L., Jean, Y.C., *J. Phys. Chem.*, 1984, **88**, 2465

187. Deng, Q., Zandiehnadem, F., Jean, Y.C., *Macromolecules*, 1992, **25**, 1090

188. Stevens, J.R., Mao, A.C., *J. Appl. Phys.*, 1970, **41**, 4273

189. Uedono, A., Sadamoto, R., Kawano,T., Tanigawa, T., Uryo, T., *Journal 0f Polymer Science :Part B*, 1995, **33**, 891

190. Ohko, Y., Uedono, A., Ujihira, Y., *Poly. Sci. B*, 1995, **33**, 1183

191. Ueda, E., Uedono, A., Ujihira, Y., *Mater. Sci. Forum*, 1992, **105**, 1721

192. Jean, Y.C., Yuan, J.P., Liu, J., Deng, Q., Hisnjin, Y., *Journal 0f Polymer Science :Part B*, 1995, **33**, 2365

193. Iwata, T., Fukushima, H., Shimotoma, M., Doyama, M., *Jpn. J. Appl. Phys. Part i*, 1981, **20**, 1799

194. Jean, Y.C., Parsai, V.E., Cheng, K.L., *Appl. Phys. A.*, 1984, **35**, 169

195. Mokrusshin, A.D., Kondrashenkova, L.A., Shevyakov, V.P., *Solid Fuel Chemistry*, 1989, **23**(part I), 110

196. Azuma, T., Saito, H., Yamazaki, Y., Komaki, K., Nagashima, Y., Watanabe, H., Hyodo, T., Kataura, H., Kobayashi, N., *J. Phys. Soc. Jpn.*, 1991, **60**, 2812

197. Dryzek, J., Pamula, E., Blazewicz, S., *Phys. Stat. Sol.*, 1995, **155**, 39

198. Dale, J.M., Lester, Hulett, L.D., Rosseel, T.M., *J. Appl. Polym. Sci.*, 1987, **33**, 3055

199. Hall, P.J., Mackinnon, A., Pethrick, R., *Prep. Fuel Chem. Div., Am. Chem. Soc.*, 1992, **37**, 893

200. Aldrich, Catalogue Handbook of Fine Chemicals 1996-1997, Sigma-Aldrich Company Ltd, Gillingham, 1996, pp. 1275

201. Dacey, J.R., Clunie, J.C, Thomas, D.G., *Trans. Faraday Soc.*, 1958, **54**, 250

202. Culver, R.V., Heath, N.S., *Trans. Faraday Soc.*, 1955, **51**, 1569

203. Everett, D.H., Redman, E., Miles, A.J., Davies, D.H., *Fuel*, 1963,**42**, 219

204. Ismail, I.M.K., Walker, Jr., P.L., *Carbon*, 1989, **27**, 549

205. Ismail, I.M.K., Rodges, S.L., *Carbon*, 1992, **30**, 229

206. Ismail, I.M.K., *Carbon*, 1991, **29**, 11

207. Alcañiz-Monge, J., Cazorla-Amoros, D., Linares-Solano, A., Yoshida, S., Oya, A., *Carbon*, 1994, **32**, 1277

208. Cazorla-Amoros, D., Salinas-Martinez de Lecea, C., Alcañiz-Monge, J., Linares-Solano, A., Gardner, A., North, A., Dore, J., *Carbon*, 1998, **36**, 309

209. Vorres, K.S., in : Users Handbook for the Argonne Premium Coal Sample Program, Argonne National Laboratory, Argonne, 1993, pp.20

210. Demir, I., Lizzion, A.A.., Fuller, E.L., Harvey, R.D., *Prep. Fuel Chem. Div. Am. Chem. Soc.*, 1993, **38**, 1178

211. Micromeritics Instrument Corporation, Accelerator Surface Area and Porosimetry System, ASAP-2010 Operator's Manual, Norcross, 1996, p 1-3

212. Lebech, B., *Neutron News*, 1990, **2**, 7

213. Abis, S. Carciuffo R, Carsughi, F, Coppola, R, Magnani, M., Rustichelli, F., Stefanon M., *Phys. Rev. B*, 1990, **42**, 2275

214. Wignall, G.D., Bates, F.S., *J. Appl. Crystallogr.*, 1987, **20**, 28

215. Higgins, J.S, Benoit, H.C., Polymers and Neutron Scattering, Clarendon Press, Oxford, 1994, p. 52,153

216. Kirkegaard, P., Eldrup, M., Mogensen, O.E, Pedersen, N.J., *Computer Physics Communications*, 1981, **23**, 307

217. Kirkegaard, P., Pedersen, N.J., and Eldrup, M., PATFIT-88 : A data-processing system for positron annihilation spectra on mainfraime and personal computers., 1989, Riso National Laboratory, Roskilde, 1989

218. Dubinin, M.M., in: *Progress in Surface and Membrane Science*, (Eds. D.A. Cadenhead, J.F. Danielli, M.D. Rosenberg), Academic Press, New York, 1975, pp. 1-72

219. Kadlec, O., *Adsorption Science & Technology*, 2001, **19**, 1

220. Jean, Y.C., *Mater. Sci. Forum*, 1997, **175-178**, 59

221. Goworek, T., Ciesielski, Jasinska, B., Wawryszczuk, J. *Chem. Phys. Lett.*, 1997, **272**, 91

222. Ciesielski, Dawidowicz, A.L., Goworek, T., Jasinska, B., Wawryszczuk, J. *Chem. Phys. Lett.*, 1998, **289**, 41

223. Carrott, P.J.M., Sing, K.S.W., in: Characterisation of Porous Solids, (Eds. K.K. Unger , J. Rouquerol, K.S.W. Sing, H.Kral), Elsevier, Amsterdam, 1988, p. 77

224. Roberts, R.A., Sing, K.S.W., Tripathi, V., *Langmuir*, 1987, **3**, 331

225. Cazorla-Amoros, D., Alcañiz-Monge, J., Linares-Solano, A., *Langmuir*, 1996, **12**, 2820

226. Cazorla-Amoros, D., Alcañiz-Monge, J., de la Casa-Lillo, M.A., Linares-Solano, A., *Langmuir*, 1998, **14**, 4589

227. Solomon, P.R., and Hamblen D.G., in : Chemistry of Coal Conversion, (Ed. R.H. Schlosberg), Plenum Press, New York, 1985, pp. 121-248

228. McCarty G.J., *Carbon*, 1977, **15**, 95

229. Herman G., Huttinger K.J., *Carbon*, 1986, **24**, 705

230. Wigmans T., *Carbon*, 1989, **27**, 13

231. Tricker M.J., Grint A., Audley G.J., Church S.M., Rainey V.S., Wright C,J., *Fuel*, 1983, **62**, 1092

PUBLICATIONS AND CONFERENCES RELATED TO THIS WORK

"Characterization of gasified carbon materials by Positron annihilation Lifetime Spectroscopy, PALS". Jhon J. Fernandez, Fanor Mondragon, Peter J. Hall. In: **2° Iberoamerican Workshop on Characterisation of Catalysts and Adsorbents**. CYTED, Sao Carlos BRASIL, February 2001

"The Effects of the Electronic Structure of the Micropores on the Small Angle Scattering of X-Rays and Neutrons". Hall , P.J. , Brown, S.D., Fernandez , J.J., Calo, J.M., **Carbon**, 2000, 38, 8, 1257-1259

"Characterisation of activated carbon fibers by positron annihilation lifetimes spectroscopy". D. Lozano-Castelló, D. Cazorla-Amorós, A. Linares-Solano, Peter J. Hall, J.J. Fernández-Hincapié. In: **Characterisation of Porous Solids V**, serie: Studies in Surface Science and Catalysis,128 (Eds. K. K. Unger, G., Kreysa, J.P., Baselt), Elsevier, Amsterdam,2000, pp. 523-532

"Positron Annihilation in Coal Chars", P.J. Hall and J.J. Fernandez. In: **Prospects for Coal Science in the 21st Century:** Proceedings of the Tenth International Conference on Coal Science , Volume I, (Eds. B. Q. Li and Z. Y. Liu), Shanxi Science & Technology Press, Taiyuan, 1999, pp. 219-222

"Carbon porosity development via small angle scattering". Calo , J.; Hall , P.J.; Brown , S.; Fernández, J. J.; Antxustegi , M. M. In: **24th Biennial Conference on Carbon**, Extended Abstracts and Program. Charleston, American Carbon Society, 1999. v. II, pp. 440-441.

"The Effects of Drying and Heat Treatment on the Pore Structure of Low Rank Coals". Peter J. Hall, Stephen D. Brown, Jhon Fernandez. In: **BENSC Experimental Reports 1998**, Berlin Neutron Scattering Center: Hahn-Meitner-Institut, Berlin, May 1999, p. 224

"Contrast Matching to Study Closed Porosity in PVBC and PGMA Resins". Peter J. Hall, F. Mondragon, W. Ruiz, J. Fernandez, A. Mackinnon, D. Gascon. In: **BENSC Experimental Reports 1997**, Berlin Neutron Scattering Center: Hahn-Meitner-Institut, Berlin, June 1998, pp.259-260